GAUGE FIELDS AND GEOMETRIC PHASES IN PERIODIC SYSTEMS

NIE WEI

NATIONAL UNIVERSITY OF SINGAPORE

2017

GAUGE FIELDS AND GEOMETRIC PHASES IN PERIODIC SYSTEMS

NIE WEI

(M.Sc., SWJTU)

A THESIS SUBMITTED FOR THE DEGREE OF
DOCTOR OF PHILOSOPHY
CENTRE FOR QUANTUM TECHNOLOGIES
NATIONAL UNIVERSITY OF SINGAPORE

2017

Supervisor:
Associate Professor Kwek Leong Chuan

Examiners:
Assistant Professor Manas Mukherjee
Professor Bruce McKellar, University of Melbourne
Professor Long Guilu, Tsinghua University

Declaration

I hereby declare that the thesis is my original work and it has been written by me in its entirety. I have duly acknowledged all the sources of information which have been used in the thesis.

This thesis has also not been submitted for any degree in any university previously.

NIE WEI

19 May, 2017

Acknowledgements

First and foremost, I would like to thank my supervisor, Kwek Leong Chuan, for his amiableness, supervision, and advice. I am grateful to Kwek's support and guidance not only in academic but also in life. I am grateful to Huo Mingxia, for her invaluable helps and advices in the research at the beginning of my PhD candidacy. Thanks to David Hutchinson and Amico Luigi for the discussions in physics which broaden my research field quite a lot. I appreciate the helps from Mei Feng, Wang Fei, and Song Guozhu for their discussions in many sorts of physics. Thanks to Kyaw Thi Ha and Kwong Chang Jian for the encouragements in the path of my research. I have benefited tremendously from discussing physics with the friends in Kwek's group. Thanks to Sai Vinjanampathy, David Herrera-Marti, Davit Aghamalyan, Andy Chia, Ewan Munro, Hermanni Heimonen, Tobias Florian Haug, Wang Shuchao, Ye Xiangjun, Wei Zhaohui, Sun Chunfang, Zhang Kejia and Zhu Jing. It has been a pleasure working with all of you.

Outside of Kwek's group, but staying in the Centre for Quantum Technologies, thanks to You Jiabin, Xiu Xiaoming, Tian Guojing, Liao Kaiyu, Wang Yukun, Zhou Yuqian, Zhang Zhichao, Victor Manuel Bastidas Valencia, and many unnamed others for putting up with me and generally being awesome. I am grateful to Jia Wenzhi, Guillermo Romero and Ching Hua Lee for helpful discussions. I also want to thank two friends who enlighten me when I feel confused about life: Zhang Jiang who has shared countless wisdom with me; Mao Zhaohui for his friendly discussions and encouragements. I am also grateful to Tan Hui Min Evon, Lim Siew Hoon for their help with administration and Alexander Ling, Ramanathan Mahendiran for serving on my committee. The works in this thesis have been funded by the CQT Scholarship, and the National Research Foundation and Ministry of Education of Singapore.

At last, thanks to my mom and dad.

Contents

Abstract

This thesis focuses on gauge fields and geometric phases in periodic systems. The simulation of Aharonov-Bohm effect is discussed in real space with optical lattice. The artificial gauge fields provide convenience in simulating the dynamics of charged particles in magnetic field with neutral atoms. In condensed matter physics, the topological invariants can characterize topological properties of the systems, e.g., Chern number in quantum Hall effect. The geometric phase in one-dimensional optical lattices is employed to study topological phase transitions. In addition, the geometric phase in spin-1/2 chains is quite interesting not only in the gapped phase, but also in the regime close to phase transition. We use geometric phases to characterize the critical and noncritical properties in generalized spin-1/2 chain with multispin interactions. Moreover, the topological phases are explored via edge states.

Publications

1. M. Huo, **W. Nie**, D. Hutchinson, and L.C. Kwek., *Interference Signatures of Abelian and Non-Abelian Aharonov-Bohm effect on Neutral Atoms in Optical Lattices.* Scientific Reports **4**, 5992 (2014).
2. F. Mei, J. You, **W. Nie**, R. Fazio, Shi-Liang Zhu, and L.C. Kwek, *Simulation and Detection of Photonic Chern Insulators in One-Dimensional Circuit Quantum Electrodynamics Lattice.* Physical Review A **92**, 041805(R) (2015).
3. Fei Wang, **W. Nie**, Xunli Feng, and C. H. Oh, *Steady-state entanglement of harmonic oscillators via dissipation in a single superconducting artificial atom.* Physical Review A **94**, 012330 (2016).
4. Fei Wang, **W. Nie**, and C. H. Oh, *Higher-order squeezing and entanglement of harmonic oscillators in superconducting circuits.* Journal of the Optical Society of America B **34**, 130 (2017).
5. **Wei Nie**, Feng Mei, Luigi Amico, and Leong Chuan Kwek, *Scaling of geometric phase versus band structure in cluster-Ising models.* arXiv:1702.02501 (2017).

List of Figures

List of Tables

Chapter 1

Introduction

Quantum computation and quantum information processing are two strong drivers that have pushed for the explorations into quantum physics for the last 20 years. This is enhanced and supported by the concomitant rapid development in material processing and electronic circuits. We start with a simple two-level system, i.e., the qubit and explore the properties by coupling it different quantum devices. Luckily, theories in quantum optics have provided many practical solutions and means to bridge our understanding and foray into quantum computing. The fast developments in coherent control of quantum systems has also led to quantum simulating, or simulation of quantum systems. Quantum simulation has since received considerable attention from people working not only in physics, but also in chemistry and biology.

Ultracold atoms in optical lattice have provided a wonderful platform for testing the possibilities of quantum simulation. Many effects, such as lattice gauge theories [1], relativistic quantum field theories [2, 3], classical magnetism [4], and so on, can be simulated in cold atom experiments. In atomic physics, there exist well-established fabrication techniques for trapping atoms in optical lattice and these optical lattices offer a number of promising properties. The fast development in ultracold atoms benefits tremendously from this controllability. For example, the interaction strength in atom gases can be tuned through Feshbach resonances. The collision properties of atom gases can also be controlled from the preparation of Bose-Einstein condensate (BEC) and degenerate Fermi gases in experiments. Moreover, it is possible to engineer different geometries and dimensions in optical lattice. Such engineering feat can also help to facilitate the exploration of many-body phenomena in higher dimensions. The measurement of quantum effects in atom gases can also be probed optically.

A lot of studies has concentrated on the quantum phase transition between Mott-

insulator and superfluid regimes [5]. The introduction of artificial gauge fields in optical lattices has also provided a fruitful ground for studying novel quantum phases with broken time-reversal symmetry [6, 7] in condensed matter systems. Indeed, the studying of artificial gauge field has attracted much attention with novel and modern applications in quantum simulation, especially those effects related to topological models. In fact, using the interactions between lights and atoms, there have been many theoretical proposals and experiments to realize spin-orbit couplings as well as the observation of quantum anomalous spin Hall effects [8, 9, 10]. Very recently, some progresses have been made towards the implementation of Thouless pumping with both bosons and fermions in optical lattices [11, 12, 13, 14].

Laser-atom coupling are well-suited for generating artificial gauge fields in an optical lattice. For example, a two-level atom moves on a 1D state-dependent optical lattice with the energy minima for g and e in the odd and even sites [6]. The laser beams can drive the transitions between g and e via laser-atom coupling. Because of the state-dependent potential, atoms with different states move to different sites and induce laser-assisted hopping between the odd and even sub-sites. To select the hopping direction, one shifts the optical lattice by applying an electric field. In addition to the laser-assisted tunneling, the adiabatic evolution can also be utilized to generate artificial gauge fields. A first step is to introduce the position dependent parameters to the Hamiltonian. This can be achieved by considering the phase and the intensity of the laser beam. In the experiments, the phase and intensity can be easily tuned by the lasers. Thus, the interaction between laser and atom is spatially dependent. The eigenstates of the interaction which is a linear combinations of g and e are also position-dependent. Without any degeneracy in the system, and assuming adiabatical condition, the geometric phase of spatially varying Hamiltonian is created.

Quantum spin Hall(QSH) effect was proposed theoretically and realized experimentally in HgTe/CdTe quantum wells [15, 16, 17]. The discovery of the QSH effect as well as the development in topological insulators and topological superconductors changes our knowledge to condensed matter physics. Although great success in exploring topological states in electronic gases, there are still some challenges, e.g., observation of Hofstadter buttery. The simulation of magnetic fields provides another way to perform such experiments in other quantum systems. In fact, inspired by the discovery of quantum Hall physics and topological insulators, experimentalists have already succeeded in realizing topological phases in optical lattice and spin-orbit coupling. Some aspects of topological phases with cold atoms have been discussed in the recent reviews [18].

The topological models in 1D are quite interesting. Zak made a pioneering contribution in this field. He has shown that one can realize Berry's phase by varying the crystal momentum through the entire Brillouin zone [19]. This topological invariant in 1D has similar role of Chern number in 2D periodic lattices. Both of them are related to physical observables in the systems. In 1D lattice, Zak phase is connected to the charge center or polarization [20, 21, 22]. The direct measurement of the Zak phase in optical lattices is easy to achieve, combining coherent Bloch oscillations with Ramsey interferometry. The topological charge pumping in optical lattice [12, 14] and quasicrystals [23] has been performed. This opens the door to novel applications in quantum transport by analogy to electron systems. There are developments, both theoretical and experimental, towards realizing the Zak phase and topological charge pumping in optical lattice starting from simple superlattice to lattice with complex internal structure in the unit cell. Other periodic systems with inversion symmetry, including waveguide array [24], 1D photonic crystals [25, 26] and acoustic system [27], have been realized experimentally. It is also found that the Zak phase can be related to the mean displacement of a particle which initially localizes on one of the nondecaying sites in the lattice with inversion symmetry [28]. This reveals the relation between topological invariant and quantum walk [29, 30, 31, 32, 33].

A second route to physics beyond topological phase transition is to explore phases with temperature and dissipations. A mixed-state version of geometric phase, related to Uhlmann's phase, built with parallel transport principle, is also a very interesting field [34, 35]. Recent work by some groups has highlighted the interesting implications of temperature and dissipations [36, 37, 38, 39]. These investigations promote the topological quantum phase transition to a mixed states topological phase transition. Indeed, the realization of topological models in the systems with dissipation gives a chance to explore the dissipation induced topological phase transition [40]. However, there are several definitions on mixed-state geometric phase [41, 42, 43]. For example, the expression in Ref. [41] bases on interferometry with proper parallel transport condition. In simple quantum systems, the geometric phase of mixed state is observed in spin half nucleus through NMR interferometry [44]. And the geometric phase of the system coupled to an environments near a quantum phase transition is also measured [45]. Recently, the proposal to observe topological Uhlmann phase in superconducting circuits is suggested [46]. Another question is the physical meaning of mixed-state geometric phase. The Berry's phase in periodic systems is found to be related to palorization in crystalline solids [21].

In addition to topological models(such as Rice-Mele and SSH models) for free parti-

cles, one can find topological invariants in 1/2-spin chains [47]. Spin-1/2 Ising and XY models in a transverse field are usually used for investigating quantum phase transitions. Such spin chain can also be simulated, e.g., with optical lattice [48, 49], circuit QED [50]. The spin chain is exactly solvable by mapping the spin operators to free fermionic operators [51]. Due to this property, the spin chain is helpful to investigate nonequilibrium dynamics [52, 53, 54]. In the periodic systems, the crystal momentum space is usually the parameter space and the geometric phase is defined there. However, Carollo and Pachos introduced a rotation of spins around the z direction [55]. This spin rotation can construct a circle in the Bloch sphere for the ground state. In 1/2-spin chain, the ground states are degenerated. For systems with degenerate states, the geometric phase can not be defined (for Abelian case). Luckily, one of the degenerated ground states is trivial and no geometric phase acquired when the system varies. The geometric phase by means of spin rotations is related to average polarization along z direction.

This thesis mainly discusses the implications of geometric phase in producing artificial gauge fields and characterizing quantum phase transitions. Depending on the parameter spaces, geometric phase can be quantized or continuously varied between different phases. Some studies on the edge modes and nonequilibrium dynamics are also included.

1.1 Organization of the Thesis

Starting with a brief introduction of gauge fields in Chapter 2, we discuss how gauge fields can be generated in simple quantum systems [56, 57] and how it is feasible experimentally by means of atom-laser interaction [58]. Geometric phase is intrinsically related to Aharonov-Bohm effect [59]. Artificial gauge field in cold atom system is a concept that bridges between them. Depending the proposals, one can create phase factors via adiabatically or non-adiabatically manipulating the systems. In the first chapter, the adiabatic case is illustrated, based on a nice review in Ref. [60].

In addition to the adiabatic approach, there are many dynamical ways to generate artificial gauge fields. Jaksch and Zoller [6, 7] studied the possibility of realizing such artificial gauge fields in optical lattice in one dimensional lattice through laser-induced hopping. For discrete sites, the hopping is complex because of the laser-assisted hopping. To control the hopping directions of cold atoms in the lattice, they propose to use different potentials for ground and excited states. Moreover, shifting of the lattice in spatial positions is performed through the application of an acceleration of the optical or electric field. In Chapter 2, we consider the generation of artificial gauge fields in ring and square

optical lattices [61]. By using the angular momentum of Laguerre-Gauss laser modes, the artificial gauge field can be generated at cold atoms circulating the lattice. We also show that Abelian and non-Abelian gauge fields can be obtained and distinguished from the interference patterns.

It is also found that Berry's phase naturally appears in periodic lattice. The reciprocal space is the parameter space where Berry's phase can be calculated. It is noted by Zak that Berry's phase in one dimensional lattice with inversion symmetry is quantized [19]. Such quantized Berry's phase is also known for Zak phase. In Chapter 3, we discuss Zak phase in one-dimensional optical lattice with many subsites. We concentrate on the three-band and four-band models.

For a 1/2-spin chain, it is proposed that rotation operations of spins in a closed loop result in a geometric phase [55]. Zhu subsequently gives a finite-size scaling analysis of the critical regime in XY model and shows universal behaviors [62]. In Chapter 4, we investigate the generalized spin chain with multispin interactions. The finite-size scaling is used to study the quantum criticality. We also consider a topological way to characterize the system by using winding number [47, 63]. The competing effect between the interactions leads to complex phases which can be labelled with winding numbers.

In topological systems, there are edge modes when the system has open boundaries. These edge modes are localized at the ends of lattice. A famous example of edge modes is the Majorana fermions in the Kitaev model [64]. In the Chapter 5, we consider a quenched proposal to study the long-time steady state of the system. The steady state can be captured by diagonal ensemble [65, 54]. We study the probability distribution and the fidelity of the quenched Aubry-André-Harper model.

With the development of topological materials, many systems can be constructed to observe topological effects. In Chapter 6, we consider the circuit-QED system to simulate Chern insulators by manipulating the couplings between neighboring resonators. The topological invariant can be inferred from the scattering coefficient.

Chapter 2

Artificial Gauge Fields with Cold Atoms

2.1 Vector Potential

The nineteenth century is a critical era for the development of physics. Faraday's electromagnetic induction opens the door for physicists to explore fundamental properties of electronic and magnetic fields. Maxwell's mathematical formulation provides a theoretical foundation for the experimental phenomena. As Einstein noted, "The escape from this unsatisfactory situation by the electric field theory of Faraday and Maxwell represents probably the most profound transformation of the foundations of physics since Newton's time." Even with the great success of Maxwell's formulae, there are still debates on some of the subtle aspects of the electromagnetic field theory. The most intriguing one is the vector potential [66]. For the first half of twentieth century, most of the textbooks regard the vector potential as mathematical gimmick for the calculation of the magnetic field without any physical meaning whatsoever. The physics behind the magnetic vector potential was only given a firm foundation by Aharonov and Bohm in 1959.

After Einstein's formulation of special and general relativity, there was an attempt to extend the electromagnetic field to gravitational theory. The first development in this direction was proposed by Hermann Weyl, who was intrigued by the idea of parallel transport of a vector in Riemannian geometry. He posed the question that if the parallel transport of a vector after going around a closed loop in space-time does not return to its original direction, the same could happen for its length. His ultimate purpose was to incorporate electromagnetic field to gravitation field. However, this idea was not successful. If it was true, as Einstein said, "the length of a common ruler would depend

on its history". After the birth of quantum mechanics, Weyl reconsidered the problem by including square root of -1. As a result, the gauge transformation gives rise a phase. Therefore, the gauge invariance is actually "phase invariance" and the gauge field should be called "phase field" [67]. In other words, Weyl's theory is a theory of electromagnetism in quantum mechanics. The gauge theory gives a structure that captures both gravitation and electromagnetic field. If one reconsider Einstein's question, a further curiosity may arise: is the phase measurable? The answer is affirmative [68]. This is nowadays known as the Aharonov-Bohm (AB) effect.

Charged particles in a magnetic field can produce interesting physics. For example, in 2D electronic gases, quantum Hall effect is realized by applying magnetic field. The Lagrangian for a charged particle of mass m charge q moving in an eletromagnetic field is

$$\mathcal{L} = \frac{1}{2}m(\frac{d\boldsymbol{r}}{dt})^2 + q(\boldsymbol{A}\frac{d\boldsymbol{r}}{dt} - W), \tag{2.1}$$

where $d\boldsymbol{r}/dt$ is velocity. $\boldsymbol{A}$ and W are vector potential (gauge field) and scalar potential, respectively. Using the standard result of electromagnetic theory, one can always find a scalar potential W and gauge field $\boldsymbol{A}$, functions of $\boldsymbol{r}$ and t such that

$$\begin{aligned} \boldsymbol{B} &= \boldsymbol{\nabla} \times \boldsymbol{A}\,, \\ \boldsymbol{E} &= -W - \frac{\partial \boldsymbol{A}}{\partial t}\,. \end{aligned} \tag{2.2}$$

The equation of motion becomes

$$m\ddot{\boldsymbol{r}} = q(\boldsymbol{E} + \boldsymbol{v} \times \boldsymbol{B}). \tag{2.3}$$

The fields $\boldsymbol{E}$ and $\boldsymbol{B}$ are invariant under gauge tranformations

$$W \to W' = W - \frac{\partial \chi}{\partial t}\,, \tag{2.4}$$

$$\boldsymbol{A} \to \boldsymbol{A}' = \boldsymbol{A} + \boldsymbol{\nabla}\chi\,. \tag{2.5}$$

The equation of motion Eq. (2.3) is gauge invariant. The Hamiltonian is

$$H = \boldsymbol{p}\boldsymbol{v} - \mathcal{L}, \tag{2.6}$$

with canonical momentum

$$\boldsymbol{p} = \frac{\partial \mathcal{L}}{\partial \dot{\boldsymbol{r}}} = m\dot{\boldsymbol{r}} + q\boldsymbol{A}\,. \tag{2.7}$$

So

$$H = \frac{(\boldsymbol{p} - q\boldsymbol{A})^2}{2m} + qW. \tag{2.8}$$

In quantum mechanics, the Schrödinger equation describing charged particle in electromagnetic field is

$$i\hbar\frac{\partial\psi(\boldsymbol{r},t)}{\partial t} = \frac{1}{2m}(-i\hbar\boldsymbol{\nabla} - q\boldsymbol{A}(\boldsymbol{r}))^2\psi(\boldsymbol{r},t). \tag{2.9}$$

One can make a gauge transformation to the wavefunction, i.e., $\psi \to \psi'$

$$\psi' = U\psi = e^{iq\chi(\boldsymbol{r},t)/\hbar}\psi, \tag{2.10}$$

and the vector potential $\boldsymbol{A}(\boldsymbol{r}) \to \boldsymbol{A}'(\boldsymbol{r}) = \boldsymbol{A}(\boldsymbol{r}) + \boldsymbol{\nabla}\chi(\boldsymbol{r})$. These two wavefunctions are both eigenfunctions of the system under the gauge transformation.

To see the topological properties of the system, one can solve the Schrödinger equation, which is

$$\frac{(p - q\boldsymbol{A})^2}{2m}\psi = E\psi. \tag{2.11}$$

The solution of above equation is $\psi = e^{\frac{ig}{\hbar}\int \boldsymbol{A}\cdot d\boldsymbol{l}}\psi_0$. ψ_0 is the wavefunction for free particle. Now, ψ' and ψ is not related by gauge transformation, because the phase factor is path integral dependent. This phase factor is sometimes called the Dirac nonintegrable phase factor. It is however the reason for AB effect.

2.2 Aharonov-Bohm Effect

The study of many electromagnetic effects involves the interplay of electric and magnetic fields ($F_{\mu\nu}$). The vector potential $\boldsymbol{A}$ and the scalar potential $W = A_0$ were not given much attention prior to the discovery of AB effect. In quantum mechanics, $F_{\mu\nu}$ alone are not enough to describe the physics and $A_\mu = (\boldsymbol{A}, A_0)$ are often needed to invoke the main physics. One such example is the Aharonov-Bohm effect.

In 1959, Aharonov and Bohm proposed an experimental setup to verify the existence of gauge field [59]. For simplicity, we assume that the solenoid is infinitesimally small and the flux in the solenoid is Φ. We can choose

$$\boldsymbol{A}(\boldsymbol{r}) = (-\frac{y\Phi}{2\pi r^2}, \frac{x\Phi}{2\pi r^2}, 0), A_0 = 0, \tag{2.12}$$

such that $\boldsymbol{\nabla} \times \boldsymbol{A} = 0$ and $\int(\boldsymbol{\nabla} \times \boldsymbol{A}) \cdot d\boldsymbol{S} = \Phi$. Even though the flux is zero outside the

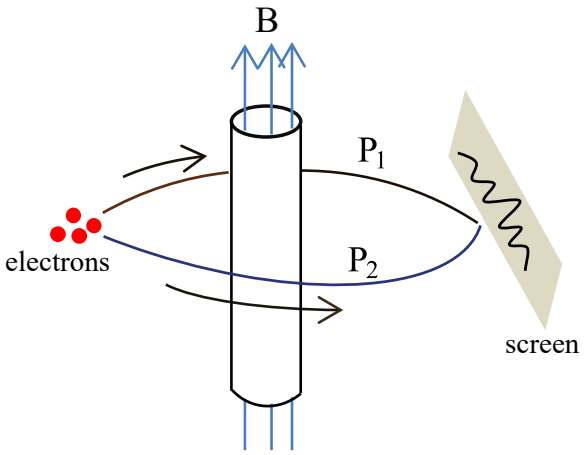

Figure 2.1: Aharonov-Bohm effect for electrons.

solenoid, the vector potential is not zero. In classical mechanics, the dynamics of charged particles does not make difference in the region of vanishing $\boldsymbol{B}$ field.

The electrons going through the region accumulate phases depending on their paths. As shown in Fig. 2.1 there are two paths P_1 and P_2 for electrons to reach the screen. Their wavefunctions are $\psi_1(\boldsymbol{r}_1)$ and $\psi_2(\boldsymbol{r}_2)$, respectively. Therefore, the wavefunction at the screen is

$$\begin{aligned} \psi \sim \psi_1(\boldsymbol{r}_1) + \psi_2(\boldsymbol{r}_2) &= e^{\frac{iq}{\hbar}\int_{P_1}\boldsymbol{A}\cdot d\boldsymbol{l}}\psi_1^0 + e^{\frac{iq}{\hbar}\int_{P_2}\boldsymbol{A}\cdot d\boldsymbol{l}}\psi_2^0 \\ &= e^{\frac{iq}{\hbar}\int_{P_1}\boldsymbol{A}\cdot d\boldsymbol{l}}(\psi_1^0 + e^{i2\pi\alpha}\psi_2^0), \end{aligned} \tag{2.13}$$

where ψ_1^0 and ψ_2^0 represent the wavefunctions of electrons free from the flux in the solenoid. $2\pi\alpha$ is the phase difference between the two paths which is related to the flux in the solenoid. We can calculate the probability for electrons arriving at the screen

$$|\psi|^2 = |\psi_1^0|^2 + |\psi_2^0|^2 + (\psi_1^0)^*\psi_2^0 e^{i2\pi\alpha} + \psi_1^0(\psi_2^0)^* e^{-i2\pi\alpha}. \tag{2.14}$$

The intensity of the electrons is affected by the relative phase between electrons from two paths. And the interference pattern can reveal the phase difference.

2.3 Artificial Gauge Fields

There are numerous effects and phenomena in other fields of physics which are related to magnetic field. In condensed matter physics, the famous examples are quantum Hall

effects, topological insulators, superconductors and semimetal [69, 70]. However, these effects can only be achieved with charged particles, like electrons. Recent developments in quantum computation and quantum optics have led to some advancement in the study of neutral particles such as neutral atoms, photons. As a toolbox for quantum simulation, cold atoms are required to possess effective magnetic fields to simulate dynamics of charged particles. In the seminal paper by Wilczek and Zee [57], they point out that "*gauge fields appear in a very natural way in ordinary quantum mechanical problems, whose initial formulation has no apparent relationship to gauge fields*". In their paper, even simple atomic systems can exhibit gauge structure.

One of the main purposes of generating artificial gauge fields is to investigate the quantum Hall effects in neutral particles. Due to the charge neutrality, an external magnetic field cannot be used to achieve breaking of time reversal symmetry. The effective magnetic field has to be synthesized. In 1996, inspired by Berry's phase which is produced from parameter-dependent adiabatic evolution, R. Dum and M. Olshanii suggested a method using atom-laser interaction to create the gauge field [58]. The internal states of atoms make it possible to realize artificial gauge field. The close analogy with the AB effect implies that appropriate controlled position-dependent Hamiltonian for neutral particle can simulate gauge field and magnetic field. Since then a lot of proposals have been suggested [6, 7, 71]. The simplest setup is a two-level atom. For two-electron atoms, such as ytterbium and alkaline-earth atoms, the long-lived two-level state exists and the spontaneous emission processes can be ignored. The position-dependent Hamiltonian can be created from the spatial variation of the Raman coupling and a position-dependent laser-atom detuning. In the following, we are going to show how the artificial gauge field can be yielded. For detailed illustration, several review articles are suggested [60, 72, 73].

2.3.1 Adiabatic Evolution Approach

In 1984, Michael Berry found that if a quantum state evolves adiabatically along a path, then a phase can develop [56]. This phase is robust and does not rely on local property but on the global structure of evolution path. Later, people realize that this geometric robustness could be applied to the quantum logic gates. Such quantum gates can be protected from quantum errors coming from unknown environment noises. Therefore, it is a promising scheme to realize quantum computation [74, 75, 76]. In addition to the overall phase factor of an evolution process, one can find the instantaneous "gauge field" in the dynamics of the adiabatically evolved quantum system. Indeed, in some

textbooks, Berry's phase is interpreted as the "flux" of "magnetic field" and is connected to the vector potential in the Schrödinger equation [77].

2.3.1.1 Abelian Artificial Gauge Fields

We first discuss the generic way to produce Abelian gauge fields. The laser-driven atom can be a setup to generate artificial gauge field [58]. We confine ourself to the single particle case in order to understand the basic idea without bothering about the interactions between atoms. There are two types of degree-of-freedom in the laser-driven atom. One is the motion of atom which can be characterized by position operator $\hat{\boldsymbol{r}}$ and momentum operator $\hat{\boldsymbol{p}} = -i\hbar\nabla_{\boldsymbol{r}}$. The second one is the internal state space. The internal quantum states can be coupled to electromagnetic fields via dipole interaction. For simplicity, we consider a two-level system as shown in Fig. 3.19(a). The atom is illuminated by a single frequency laser with detuning Δ between their frequencies. The corresponding Hamiltonian describing the laser-atom interaction can be expressed as

$$H_{2l} = \frac{\hbar}{2}\begin{pmatrix} \Delta & \Omega^* \\ \Omega & -\Delta \end{pmatrix}, \tag{2.15}$$

where Ω is the Rabi frequency and Δ is the detuning between atom and laser frequencies. After defining the parameters $\epsilon = \sqrt{\Delta^2 + |\Omega|^2}$, $\cos\vartheta = \Delta/\epsilon$, $\sin\vartheta = |\Omega|/\epsilon$, $\Omega = |\Omega|e^{-i\tau}$, we get the Hamiltonian

$$H_{2l} = \frac{\hbar\epsilon}{2}\begin{pmatrix} \cos\vartheta & e^{i\tau}\sin\vartheta \\ e^{-i\tau}\sin\vartheta & -\cos\vartheta \end{pmatrix}. \tag{2.16}$$

The total Hamiltonian is

$$H_{\text{tot}} = \left(\frac{\hat{\boldsymbol{p}}^2}{2m} + V\right)\hat{\boldsymbol{I}} + H_{2l}, \tag{2.17}$$

where V is the potential for atom. $\hat{\boldsymbol{I}}$ is the identity operator in the internal state space. We assume that the potential V acts on the particle in such a way that it is independent of its internal state. In Fig. 3.19(b) the state evolution is represented by the path on the Bloch sphere. The dynamics of the system can be mapped to points on the sphere. The eigenstates of internal Hamiltonian Eq. (2.16) is written as $|\chi_1\rangle$ and $|\chi_2\rangle$, which are

$$|\chi_1\rangle = \begin{pmatrix} -e^{i\tau}\sin\frac{\vartheta}{2} \\ \cos\frac{\vartheta}{2} \end{pmatrix}, \tag{2.18}$$

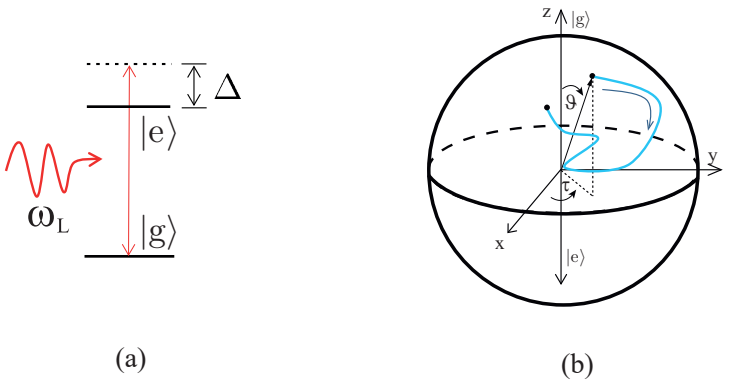

(a) (b)

Figure 2.2: Energy level with atom-laser interaction (a) and Bloch sphere (b) for the two level system.

$$|\chi_2\rangle = \begin{pmatrix} \cos\frac{\vartheta}{2} \\ e^{-i\tau}\sin\frac{\vartheta}{2} \end{pmatrix}, \tag{2.19}$$

corresponding to ground and excited states with eigenenergies $-\frac{\hbar\epsilon}{2}$ and $\frac{\hbar\epsilon}{2}$, respectively.

One can have the wavefunction of the system in terms of this adiabatic basis

$$|\Psi(\boldsymbol{r},t)\rangle = \sum_{j=1,2} \psi_j(\boldsymbol{r},t)|\chi_j(\boldsymbol{r})\rangle, \tag{2.20}$$

where $\psi_j(\boldsymbol{r},t)$ is the wave function for the center-of-mass motion of the atom in the internal state $|\chi_j(\boldsymbol{r})\rangle$. We assume that the internal states are robust to the velocity of the particle, which means that the system remains in the eigenstates. Acting the momentum operator on the state Eq. (2.20) leads to

$$\hat{\boldsymbol{p}}|\Psi\rangle = \sum_{j,l=1}^{2} \left[(\delta_{j,l}\hat{\boldsymbol{p}} - \boldsymbol{A}_{jl})\,\psi_l\right]|\chi_j\rangle, \tag{2.21}$$

with the artificial gauge field $\boldsymbol{A}_{jl}(\boldsymbol{r}) = i\hbar\langle\chi_j|\boldsymbol{\nabla}|\chi_l\rangle$. So $\boldsymbol{A}_{12}(\boldsymbol{r})$ is actually the connection between $|\chi_1\rangle$ and $|\chi_2\rangle$. To see how the artificial gauge field can be produced from the laser driving, we assume that the internal state is in the ground state, i.e., $\psi_2 = 0$.

$$\hat{\boldsymbol{p}}|\Psi\rangle = (\hat{\boldsymbol{p}} - \boldsymbol{A}_{11})\,\psi_1|\chi_1\rangle - \boldsymbol{A}_{21}\psi_1|\chi_2\rangle. \tag{2.22}$$

By projecting to the $|\chi_1\rangle$, we arrive at an effective Hamiltonian

$$H_{\text{eff}} = \frac{(\hat{\boldsymbol{p}} - \boldsymbol{A}_{11})^2}{2m} + W + V - \frac{\hbar\epsilon}{2}, \tag{2.23}$$

with $\boldsymbol{A}_{11} = i\hbar\langle\chi_1|\boldsymbol{\nabla}|\chi_1\rangle = \frac{\hbar}{2}(1-\cos\vartheta)\boldsymbol{\nabla}\tau$ and scalar potential $W = \frac{\hbar^2}{2m}|\langle\chi_2|\boldsymbol{\nabla}|\chi_1\rangle|^2$. The scalar potential can be regarded as the kinetic energy with atomic micro-motion created by quantum fluctuations of the radiative force [78]. The state-dependent scalar potential is not very interesting because one can use other ways, such as Stark shift, to create such potential. However, the artificial gauge field is quite nontrivial because it simulates the effective magnetic field for neutral atoms. The effective magnetic field for the ground state $|\chi_1\rangle$ is

$$\boldsymbol{B} = \boldsymbol{\nabla} \times \boldsymbol{A}_{11} = -\frac{\hbar}{2}\boldsymbol{\nabla}(\cos\vartheta) \times \boldsymbol{\nabla}\tau. \tag{2.24}$$

ϑ is related to both magnitude of Rabi frequency and detuning. τ is the phase of Rabi frequency. They are usually space-dependent quantities. By manipulating ϑ and τ, it is possible to obtain the effective magnetic field. This is the illustration for artificial gauge field with two-level atom. It requires the atom in the adiabatic eigenstate. For the Λ-type atom, as shown in Fig. 2.3(a), one can realize the effective two-level system with large detuning. Such three-level system can be described as

$$H_\Lambda = \hbar(\omega_1-\omega_2)|g_2\rangle\langle g_2| + \hbar\omega_1|e\rangle\langle e| + (\frac{\hbar}{2}\Omega_1 e^{-i\omega_{L1}t}|e\rangle\langle g_1| + \frac{\hbar}{2}\Omega_2 e^{-i\omega_{L2}t}|e\rangle\langle g_2| + h.c.). \tag{2.25}$$

After making a rotating frame transformation with

$$U = \begin{pmatrix} \frac{\delta_1-\delta_2}{2} & 0 & 0 \\ 0 & \omega_1-\omega_2-\frac{\delta_1-\delta_2}{2} & 0 \\ 0 & 0 & \omega_1-\frac{\delta_1+\delta_2}{2} \end{pmatrix}, \tag{2.26}$$

the Hamiltonian can be changed as

$$\begin{aligned} H_{rot} &= UH_{3l}U^\dagger - i\hbar U\frac{\partial}{\partial t}U^\dagger \\ &= \hbar\begin{pmatrix} -\frac{\delta_1-\delta_2}{2} & 0 & \frac{\Omega_1^*}{2} \\ 0 & \frac{\delta_1-\delta_2}{2} & \frac{\Omega_2^*}{2} \\ \frac{\Omega_1}{2} & \frac{\Omega_2}{2} & \frac{\delta_1+\delta_2}{2} \end{pmatrix}, \end{aligned} \tag{2.27}$$

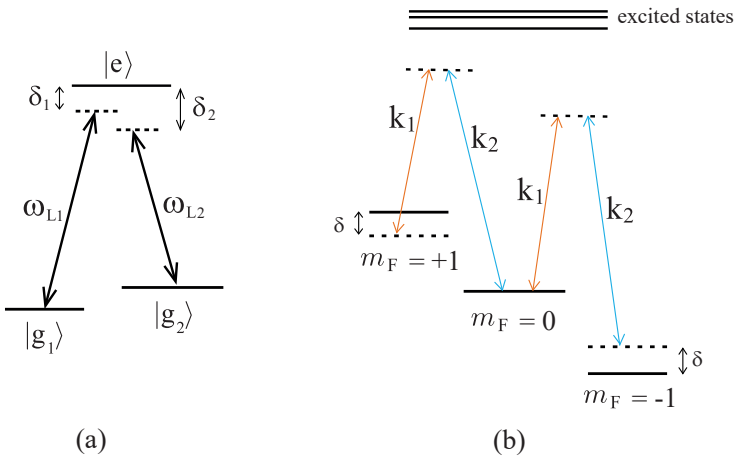

Figure 2.3: The atom-laser interaction with (a) Λ-type and (b) M-type schemes.

with $\delta_1 = \omega_1 - \omega_{L1}$ and $\delta_2 = \omega_2 - \omega_{L2}$. If the detuning of the excited state $|e\rangle$ is quite large such that $\frac{|\delta_1+\delta_2|}{2} \gg \frac{|\delta_1-\delta_2|}{2}, \frac{|\Omega_1|}{2}, \frac{|\Omega_2|}{2}$, the dynamics of the excited state $|e\rangle$ can be ignored. Therefore, one can get the effective Hamiltonian for the lowest two states

$$H_{\Lambda}^{(\mathrm{eff})} = -\hbar \begin{pmatrix} \frac{\delta_1-\delta_2}{2} + \frac{|\Omega_1|^2}{2(\delta_1+\delta_2)} & \frac{\Omega_1^*\Omega_2}{2(\delta_1+\delta_2)} \\ \frac{\Omega_1\Omega_2^*}{2(\delta_1+\delta_2)} & -\frac{\delta_1-\delta_2}{2} + \frac{|\Omega_2|^2}{2(\delta_1+\delta_2)} \end{pmatrix}. \tag{2.28}$$

The effective two-level system is similar to Eq. (2.15) with effective Rabi frequency in the off-diagonal part of Eq. (2.28). The effective Rabi frequency between the two ground states $|g_1\rangle$ and $|g_2\rangle$ is generated from the two-photon process. Recently, the experiments based on M-type scheme (see Fig. 2.3(b)) have been realized [79, 80]. A ^{87}Rb BEC is trapped in the $F = 1$ ground state with two Raman laser beams with momenta $\boldsymbol{k}_1$ and $\boldsymbol{k}_2$. The energy levels are shifted by applying a magnetic field. As a result, the levels $|m_F = \pm 1\rangle$ are displaced with respect to $|m_F = 0\rangle$ and the two laser beams couple three states with detunings $\pm\delta$. From above discussion for Λ-type levels, one can get the effective Hamiltonian for the M-type system

$$H_{\mathrm{M}} = \frac{\hbar}{2} \begin{pmatrix} -2\delta & \tilde{\Omega}^* & 0 \\ \tilde{\Omega} & 0 & \tilde{\Omega}^* \\ 0 & \tilde{\Omega} & 2\delta \end{pmatrix}, \tag{2.29}$$

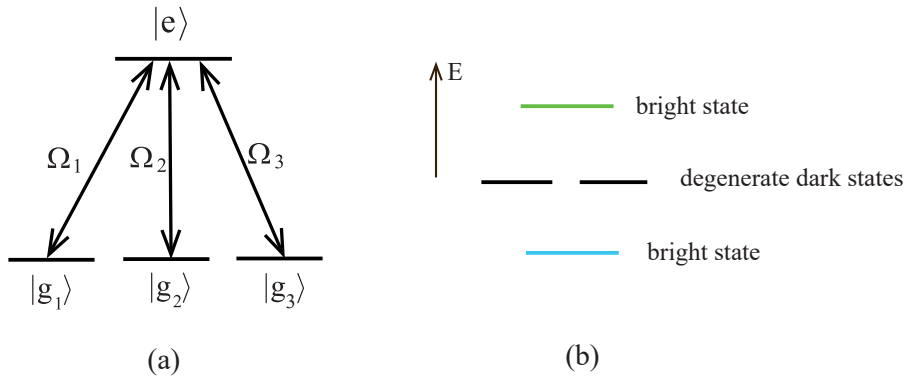

Figure 2.4: (a) Atom-laser interaction for tripod levels and (b) the corresponding eigenenergies.

with $\tilde{\Omega} = |\tilde{\Omega}|e^{-i\tilde{\tau}}$ and $\tilde{\tau} = (\boldsymbol{k}_1 - \boldsymbol{k}_2)\boldsymbol{r}$. The ground state is

$$|\chi_g\rangle = e^{i\tilde{\tau}} \cos^2 \frac{\vartheta}{2}|-1\rangle - \frac{\sin\vartheta}{\sqrt{2}}|0\rangle + e^{-i\tilde{\tau}} \sin^2 \frac{\vartheta}{2}|+1\rangle, \tag{2.30}$$

where $\vartheta = \arctan \frac{|\tilde{\Omega}|}{\sqrt{2}\delta}$. The artificial gauge field is $\boldsymbol{A} = i\hbar\langle\chi_g|\boldsymbol{\nabla}|\chi_g\rangle = -\hbar(\boldsymbol{k}_1 - \boldsymbol{k}_2)\cos\vartheta$. Therefore, the two-photon process with non-zero momentum exchange yields the artificial gauge field.

2.3.1.2 Non-Abelian Gauge Fields

We have analyzed the artificial gauge field for the ground eigenstate. This belongs to the Abelian case. If more eigenstates are considered, one can have different artificial gauge fields and effective magnetic fields. They can be used to simulate spin Hall effect [81] and pseudospin-dependent Stern-Gerlach effects [82].

Following the adiabatic approach, one can employ a degenerate multiple-level structure [57, 83] to create non-Abelian gauge fields. An example with degenerate eigenstates is shown in Fig. 2.4. (a) is the tripod level with three degenerate ground states. They are coupled to the excited state. With such atom-laser interaction, there exist degenerate eigenstates which are separated from other states, as shown in Fig. 2.4(b). It is realized by Wilczek and Zee that such degenerate eigenstates generalize Berry's phase from Abelian to non-Abelian [57]. And the non-Abelian gauge fields can be simulated in such degenerate systems. Here, we consider a general situation with multiple degenerate eigenstates.

And the full quantum state can be written as $|\tilde{\Psi}(\boldsymbol{r},t)\rangle = \sum_{j=1}^{N} \tilde{\psi}_j(\boldsymbol{r},t)|\tilde{\chi}_j(\boldsymbol{r})\rangle$. We assume that there are q degenerate eigenstates, i.e., $\{|\tilde{\chi}_1(\boldsymbol{r})\rangle, |\tilde{\chi}_2(\boldsymbol{r})\rangle, \ldots, |\tilde{\chi}_q(\boldsymbol{r})\rangle\}$. Similar to the effective Hamiltonian for one eigenstate (see Eq. (2.23)), the effective Hamiltonian for q degenerate eigenstates is

$$H_{\mathrm{NA}} = \frac{(\hat{\boldsymbol{p}} - \tilde{\boldsymbol{A}})^2}{2m} + \tilde{W} + V\hat{\boldsymbol{I}}_q + \varepsilon, \tag{2.31}$$

where $\hat{\boldsymbol{I}}_q$ is the identity operator in the space of q degenerate eigenstates. ε is a diagonal matrix of eigenenergies $\varepsilon_j (j = 1, ..., q)$. $\tilde{\boldsymbol{A}}$ and $\tilde{W}$ are $q \times q$ matrices with elements

$$\begin{aligned}
\tilde{\boldsymbol{A}}_{i,j} &= i\hbar\langle\tilde{\chi}_i|\boldsymbol{\nabla}\tilde{\chi}_j\rangle, \\
\tilde{W}_{i,j} &= \frac{1}{2m}\sum_{l=q+1}^{N} \tilde{\boldsymbol{A}}_{i,l}\cdot\tilde{\boldsymbol{A}}_{l,j} \\
&= \frac{\hbar^2}{2m}(\langle\boldsymbol{\nabla}\tilde{\chi}_i|\boldsymbol{\nabla}\tilde{\chi}_j\rangle + \sum_{k=1}^{q}\langle\tilde{\chi}_i|\boldsymbol{\nabla}\tilde{\chi}_k\rangle\langle\tilde{\chi}_k|\boldsymbol{\nabla}\tilde{\chi}_j\rangle),
\end{aligned} \tag{2.32}$$

with $i, j \in \{1, ..., q\}$. Here, we use $\nabla|\tilde{\chi}\rangle = |\nabla\tilde{\chi}\rangle$. The effective magnetic field $\boldsymbol{B}$ can be expressed as $B_i = \frac{1}{2}\epsilon_{ikl}F_{kl}$ with

$$F_{kl} = \partial_k\tilde{A}_l - \partial_l\tilde{A}_k - \frac{i}{\hbar}[\tilde{A}_k, \tilde{A}_l]. \tag{2.33}$$

The term $\frac{1}{2}\epsilon_{ikl}[\tilde{A}_k, \tilde{A}_l]$ is not necessary vanishing, for the vector components of $\tilde{\boldsymbol{A}}$ do not commute in general. Therefore, when degenerate eigenstates appear in the system, effective non-Abelian artificial gauge fields and magnetic fields can be created.

2.3.2 Laser-Assisted Tunneling in Optical Lattice

In the last twenty years or so, cold atoms in optical lattices have made tremendous progress. The periodicity of optical lattices makes it possible to study physical models originally developed in condensed matter physics. For example, in the pioneering work of D. Jaksch *et al.*, the Bose-Hubbard model which exhibits a quantum phase transition between superfluid and Mott insulator is suggested [5]. This work has motivated much progress in the techniques in optical lattice. Thanks to the flexibility in the control with some parameters such as lattice depth and spacing, the optical lattice can be tuned or switched off at will during the experiment. Further more, the optical potentials can be adjusted, modifying the geometry and dimensionality of the lattice, and forming patterns

such as triangular lattice [84] and Kagome lattice [85]. These advantages make it a promising experimental platform to mimick solid-state systems.

Another development in recent years is the quantum Hall effect in solid state physics. The intrinsic symmetries, like time reversal symmetry, particle-hole symmetry and chiral symmetry, have given rise to systems exhibiting topological properties. To simulate quantum Hall physics with neutral atoms in optical lattice, the first step is to generate artificial magnetic field. The artificial gauge field can be produced by laser-induced complex hopping parameters in optical lattice [86, 87, 88, 6, 3, 71].

In an optical lattice, the tunnelling of cold atoms between two neighbor sites is determined by the overlap between two wavefunctions. In a deep potential well, because of the negligible overlap between them, tunnleing is unlikely. As the potential decreases, the kinetic energy makes it possible to tunnel to neighbor sites. To effectively describe the system, a tight-binding approximation is usually assumed. The dynamics of ultracold dilute gas of bosonic atoms in 3D optical lattice can be described by a Bose-Hubbard model [5]

$$\begin{aligned} H = & \int d^3\boldsymbol{r}\psi^\dagger(\boldsymbol{r})\left(-\frac{\hat{\boldsymbol{p}}^2}{2m}+V_0(\boldsymbol{r})\right)\psi(\boldsymbol{r}) \\ & +\frac{1}{2}\frac{4\pi a_s\hbar^2}{m}\int d^3\boldsymbol{r}\psi^\dagger(\boldsymbol{r})\psi^\dagger(\boldsymbol{r})\psi(\boldsymbol{r})\psi(\boldsymbol{r}) \end{aligned} \tag{2.34}$$

where $\psi(\boldsymbol{r})$ is a boson field operator for atoms in a given internal atomic state. $V_0(\boldsymbol{r})$ is the optical lattice potential and a_s is the s-wave scattering length. To simplify the above Hamiltonian, one should employ the Wannier functions which constitute an orthogonal and normalized set of wave functions. They are maximally localized to individual lattice sites. In periodic lattices, Wannier functions are a unitary transformation of the Bloch functions and are formally an equivalent representation to describe the system. Expanding the field operators in the Wannier basis and keeping only the lowest vibrational states(i.e., s orbitals), $\psi(\boldsymbol{r}) = \sum_i b_i w(\boldsymbol{r}-\boldsymbol{r}_i)$, the Hamiltonian Eq. (2.34) can be rewritten as a Bose-Hubbard model

$$H = -J\sum_{\langle i,j\rangle}\hat{b}_i^\dagger\hat{b}_j - \sum_i \mu_i\hat{n}_i + \frac{U}{2}\sum_i \hat{n}_i(\hat{n}_i-1) \tag{2.35}$$

with $J = \int d^3\boldsymbol{r}\omega^*(\boldsymbol{r}-\boldsymbol{r}_i)(-\frac{\hbar^2}{2m}\boldsymbol{\nabla}^2+V_0(\boldsymbol{r}))\omega(\boldsymbol{r}-\boldsymbol{r}_j)$ being the tunneling matrix element between adjacent sites. $\langle i,j\rangle$ denotes summation over all neighbor lattice sites i and j. $\hat{b}_i$ and $\hat{b}_i^\dagger$ are bosonic annihilation and creation operators such that $\hat{n}_i = b_i^\dagger b_i$ is the number

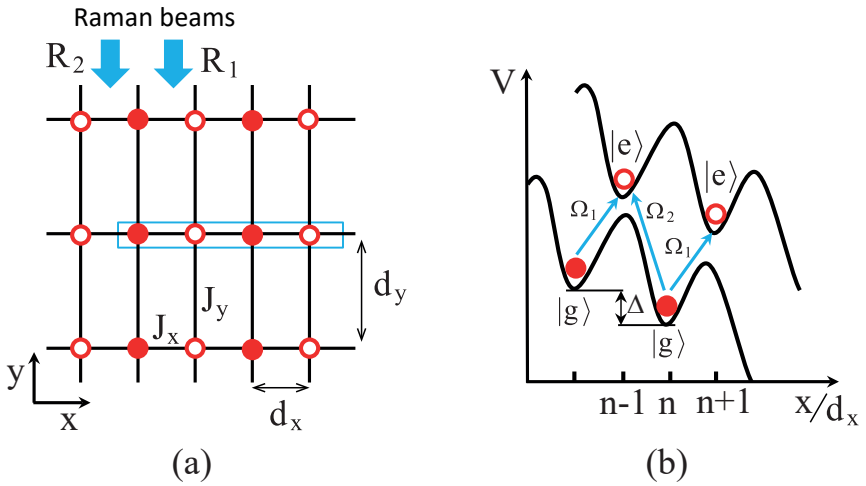

Figure 2.5: (a) Laser-assisted hopping in 2D square lattice. (b) is the direction-dependent hopping.

operator of atoms in the lattice site i. $\hat{b}_i$ and $\hat{b}_i^\dagger$ obey the canonical commutation relations $[\hat{b}_i, \hat{b}_j^\dagger] = \delta_{ij}$. The model is described by the tunneling amplitude J, the chemical potential μ and the on-site interaction U which can be attractive ($U < 0$) or repulsive $U > 0$. The phase diagram is known to possess the Mott-insulator phase ($U \gg J$) and the superfluid phase ($U \ll J$).

In the following discussion, we consider the non-interacting atom approximation, i.e., $U = 0$. To control the hopping, laser-induced tunnelling is introduced [5, 89]. As shown in Ref. [6], this method can be used to create artificial gauge fields in optical lattice. We assume that we have a 3D optical lattice where the tunneling in z direction is turned off and the lattice has the spacing $d_x = \lambda/4 (d_y = \lambda/2)$ in the x and y directions. In the x direction, the two states $|g\rangle$ and $|e\rangle$ have different potentials if their polarizabilities are opposite. By choosing this kind of polarizabilities, one can have state-dependent optical potential. In Fig. 2.5(a), we show state-dependent 2D optical lattice where the blue box is shown in (b), which illustrates the tilted optical potential in the x direction. Two running-wave beams R_1 and R_2 with Rabi frequencies Ω_1 and Ω_2 propagate along $-y$, which can resonantly drive transitions between $|g\rangle$ and $|e\rangle$ at tilted potentials. Thanks to the different optical potentials felt by $|g\rangle$ and $|e\rangle$, one can drive atoms along specific directions. For example, driving $|g\rangle$ at site n with Ω_1 laser will make the atom hopping to $|e\rangle$ at site $n + 1$. But if we use Ω_2, the atom will be driven to $|e\rangle$ at site $n - 1$. In experiment, this tilted potential can be experimentally realized by putting the lattice in static electric field or by accelerating the lattice.

The tunneling between two neighbor sites located at $\boldsymbol{r}_g = (n, m)$ and $\boldsymbol{r}_e = \boldsymbol{r}_g + \boldsymbol{b}_1 = (n+1, m)$ can be calculated as

$$J_{eg}^{(x)} e^{i\boldsymbol{k}\cdot\boldsymbol{r}_g} = e^{i\boldsymbol{k}\cdot\boldsymbol{r}_g} \frac{\hbar\Omega}{2} \int w_e^*(\boldsymbol{r} - \boldsymbol{b}_1) e^{i\boldsymbol{k}\cdot\boldsymbol{r}} w_g(\boldsymbol{r}) d^2\boldsymbol{r} \tag{2.36}$$

where $w_{g(e)}(\boldsymbol{r})$ are Wannier functions for corresponding states and $\boldsymbol{b}_1 = \lambda/4\hat{\boldsymbol{x}}$. We can see that the laser induced tunnelings between two neighbor sites $|e\rangle_n$ and $|g\rangle_{n\pm1}$ contain phase factors. Because of the factor $e^{i\boldsymbol{k}\cdot\boldsymbol{r}}$, the integral is nonzero when $2\pi/|\boldsymbol{k}|$ is of the order of the lattice spacing. This laser driving transition is much stronger than J, so the tunnelings along x direction are dominated by $J_{eg}^{(x)}$. Assume that $J_{eg}^{(x)} = J_x$ for Ω_1 and Ω_2. Therefore, the final Hamiltonian is

$$\begin{aligned} H = & -J_x \sum_{n,m} (e^{i2\pi\alpha m} \hat{c}_{2n+1,m}^\dagger \hat{c}_{2n,m} + e^{i2\pi\alpha m} \hat{c}_{2n+1,m}^\dagger \hat{c}_{2(n+1),m} + h.c.) \\ & -J_y \sum_{n,m} (\hat{c}_{n,m\pm1}^\dagger \hat{c}_{n,m} + h.c.), \end{aligned} \tag{2.37}$$

where $\alpha = \frac{k_y \lambda}{4\pi}$, which can be tuned by adjusting the angle between laser beam and the z-axis.

To realize such experiment, cold atoms with long lifetime for excited state should be considered. For example, atoms with two electrons in the outermost shell, i.e., ytterbium and alkaline-earth atoms, have a spin-singlet ground state and a long-lived spin triplet excited state. Further more, in order to avoid excitations to higher-lying motional Bloch band, the Rabi frequency Ω should be small compared to the energy gap between ground and first excited bands.

2.4 Artificial Gauge Fields by Laguerre-Gauss Laser Modes

In 1992, Allen *et al.* found that laser beams with angular momentum could be experimentally realized. These laser beams have helical phase fronts and so have an azimuthal component to the Poynting vector, which results in angular momentum along the beam travelling axis. The applications of orbit angular momentum of laser light include Hall effects [90, 91], cooling of rotational motion [92], measuring superfluid fraction [93]. It provides a useful tool for quantum information processing and quantum simulation. For

example, creation of artificial gauge fields using laser with angular momentum is studied in wide literature [61, 94, 95, 96, 91, 97].

Laguerre-Gauss (LG) modes are those modes with nonzero intrinsic orbital angular momenta. They form a complete and orthogonal basis from which an arbitrary field distribution can de described. LG modes can be produced by using computer generated holograms [98] or spatial light modulator [99]. LG laser has been shown to trap cold atoms in a ring structure potential [100]. And recently, many works have shown circulating currents with the similar ring structure [93, 101, 102]. Interestingly, one can also use LG laser to create ring-shaped optical lattice (RSOL) [61, 103]. In Ref. [61], RSOL is obtained by interfering a LG beam and a plane wave. Another method [103] to create RSOL is to use two LG modes with different azimuthal indices. The spatial structure of the intensity distribution can be manipulated by changing the detuning between laser frequency and atomic resonance frequency. RSOL make it ideal for studying persistent currents in a geometry with periodic boundary conditions. It stimulates many potential applications, such as quantum engine [104], superfluid qubits [105, 106], and atomtronics [107].

With the help of the laser-driven-hopping in lattice, we will show that one can naturally create artificial gauge fields in this RSOL. This LG laser-driven proposal is different from those for atoms cloud [94, 95, 96, 97] where Berry's approach is used. Here we employ LG-laser-assisted tunneling to produce artificial gauge field in ring lattice or square lattice. Using this LG-laser-assisted method, one can detect Abelian and non-Abelian artificial gauge fields by interference patterns. As shown in Fig. 2.6(a), the LG laser is applied perpendicular to the lattice. The amplitude of the LG laser resonant to the $|g\rangle$-$|e\rangle$ transition reads

$$E(\mathbf{r}) = E f_{pl}(r) e^{il\varphi} e^{i(\omega t - kz)}, \tag{2.38}$$

where $f_{pl}(r) = (-1)^p \sqrt{\frac{2p!}{\pi(p+|l|)!}} \xi^{|l|+2} L_p^{|l|} e^{-\xi^2}$, $\xi = \frac{\sqrt{2}r}{r_{\rm w}}$, $r_{\rm w}$ is the waist of the beam, and $L_p^{|l|}$ are the Laguerre functions [61]. For an $N_S \times N_S$ 2D lattice, we choose $r_{\rm w} = N_S a/2$. The cylindrical coordinate $(r,\ \varphi,\ z)$ is chosen that the longitudinal axis z is along the propagation direction of the LG laser, and the labels p and l represent the radial and azimuthal indices, respectively. In Fig. 2.6(a) and (b), we show LG-laser-assisted tunneling in square lattice in xy plane. This method is quite similar to the one used in the experiment of forming toroidal BEC [101] where atoms can be confined and guided by the LG laser. We would like to note that apart from the typical square lattice system which

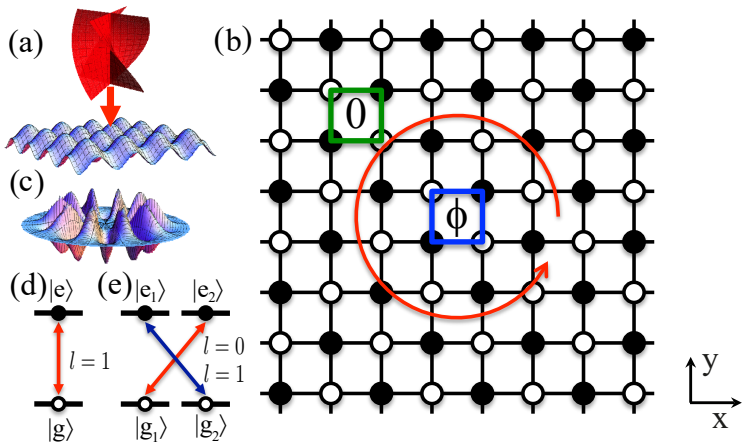

Figure 2.6: Schematic diagram for generating strongly localized effective Abelian and non-Abelian gauge fields with cold atoms trapped in square (a), (b) and ring (c) lattices. (d) and (e) are two schemes to generate Abelian and non-Abelian artificial gauge fields.

can be created by the interference of counter-propagating laser beams at the "anti-magic" wavelength, a ring lattice in (c) can be created by interfering an off-resonant LG laser and a plane wave with wavelength chosen to be at the "anti-magic" wavelength [61]. At this stage, the lattice depth is set to be very large such that the tunneling of atoms is strongly suppressed. As shown in Fig. 2.6(d), resonant LG lasers are applied to drive transitions between the $|g\rangle$ and $|e\rangle$ states, leading to atomic hoppings along a loop as shown in Fig. 2.6(b). Different values of l correspond to different accumulated phase when atoms move around the loop. We consider $l = 1$ and $l = 0$ lasers here. For the former with $l = 1$, it is found that the accumulated phase is π, which resembles a system where an Abelian magnetic field is applied to the atoms. For the latter with $l = 0$, the accumulated phase is 0, thus emulating a system with a zero magnetic field applied to the atoms. Moreover, when considering two sub-states in each $|g\rangle$ and $|e\rangle$ levels, which is shown in Fig. 2.6(e), SU(2) field can be generated by employing two LG lasers with $l = 0$ and $l = 1$ to drive transitions between different sub-states.

We first consider a Hamiltonian describing atoms with only one sub-state in each $|g\rangle$ and $|e\rangle$ levels as

$$H = \sum_{s=g,e} \int d\mathbf{r}\psi_s^\dagger(\mathbf{r})[\frac{\hat{\mathbf{p}}^2}{2m} + \eta_s V(\mathbf{r})]\psi_s(\mathbf{r}) - \int d\mathbf{r}[d_{eg}E(\mathbf{r})^* e^{i\omega t}\psi_e^\dagger(\mathbf{r})\psi_g(\mathbf{r}) + h.c.]. \quad (2.39)$$

The three terms in turn give the kinetic energy, the lattice potential, the laser-assisted

transition, respectively. The state-dependent sign of the lattice potential $V(r)$ is denoted by $\eta_g = +$ and $\eta_e = -$, due to the lattice lasers at the "anti-magic" wavelength. The dipole moment of the $|g\rangle$-$|e\rangle$ transition is denoted by d_{eg}.

We choose a lattice potential V that is minimized at sites $\mathcal{G} = \{\text{open-circle sites}\}$ and maximized at sites $\mathcal{E} = \{\text{solid-circle sites}\}$ (see Fig. 2.6). In the presence of a deep lattice potential, $\psi_s^\dagger(\mathbf{r})$ can be expressed by Wannier functions in the lowest band as $\psi_{g(e)}^\dagger(\mathbf{r}) \simeq \sum_{j\in\mathcal{G}(\mathcal{E})} a_j^\dagger \omega^*(\mathbf{r}-\mathbf{r_j})$. In the numerical simulation, we approximate the Wannier functions to be Gaussion functions. Here, we have assumed that the lattice potential is symmetric for the $|g\rangle$ and $|e\rangle$ states. The Hamiltonian then reduces to a tight-binding model as

$$H = -\sum_{\langle i,j\rangle}(J_{i,j}\hat{a}_i^\dagger \hat{a}_j + h.c.) + \sum_i \epsilon_i \hat{a}_i^\dagger \hat{a}_i. \tag{2.40}$$

Here, the chemical potential ϵ_i is not relevant in terms of the gauge fields, so we treat it as uniform by tuning the lattice potential. For the first hopping term, $\langle i,j\rangle$ denotes two nearest-neighbor (NN) sites that one is in the set $\mathcal{G}$ while the other is in the set $\mathcal{E}$, between which the tunnelling is induced by the LG laser and has a strength

$$J_{i,j} = d_{eg}E \int d\mathbf{r}\omega^*(\mathbf{r}-\mathbf{r}_i) f_{pl}(r) e^{-il\varphi} e^{ikz} \omega(\mathbf{r}-\mathbf{r}_j), \tag{2.41}$$

where $i \in \mathcal{G}$ and $j \in \mathcal{E}$.

A natural property of the laser with a non-zero orbital angular momentum is a position-dependent phase. Since the laser is applied perpendicular to the lattice, the phase of $J_{i,j}$ will only depend on the azimuthal angle φ, as shown in Eq. (2.41). The phase of $J_{i,j}$ can be estimated as $J_{i,j} \propto e^{-il\varphi}$ with φ the azimuthal angle of the midpoint between two adjacent sites $i \in \mathcal{G}$ and $j \in \mathcal{E}$. We would like to remark that the sign of the phase depends on the tunneling direction, where for $i \in \mathcal{E}$ and $j \in \mathcal{G}$, $J_{i,j} \propto e^{il\varphi}$. Due to the vortex of the LG laser, the accumulated phase for atoms moving around a loop enclosing or excluding the laser centre are different. As a simplified illustration, we consider a centre cell of the square lattice [blue square in the centre of Fig. 2.6(b)]. Here, we assume that the laser centre coincides with the centre of this cell. As a four-site circle, $\mathcal{G}$ and $\mathcal{E}$ sites appear alternatively. Without the loss of generality, we assume $\varphi = 0$ along the upward direction in Fig. 2.6(b). Then, for a particle moving in a counterclockwise direction, it undergoes tunneling with phases 0, $\frac{l\pi}{2}$, $-l\pi$, and $\frac{3l\pi}{2}$ in the four links, respectively. As a result, the accumulated phase around the centre cell is given by

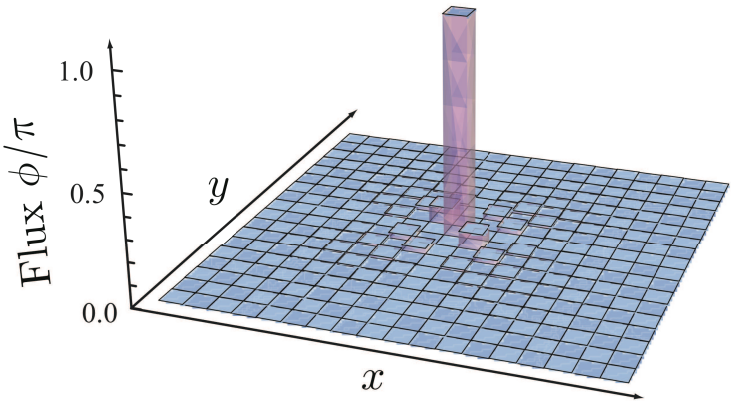

Figure 2.7: Numerically calculated net flux for each cell on a 2D square lattice.

$0 + \frac{l\pi}{2} - l\pi + \frac{3l\pi}{2} = l\pi$. By choosing an odd l, the accumulated phase is nontrivial, giving a non-zero gauge field within the centre cell. In the following, we focus on the case with $l = 1$ for the generation of an Abelian gauge field. As a comparison, a laser with $l = 0$ will give a zero accumulated phase and therefore correspond to a zero gauge field. On the other hand, for a cell far away from the laser centre [green square in Fig. 2.6(b)], the accumulated phase is always zero for any l, which means that a non-zero gauge field is strongly localized inside the centre cell for $l = 1$, resembling a very thin solenoid. As an illustration, we consider a cell centred around $\mathbf{r}_0$. The laser centre is set to be the origin of the system. The coordinates of each site belonging to the cell is $\mathbf{r} = \mathbf{r}_0 + \delta\mathbf{r}$, which gives the arimuthal angle

$$\varphi = \arctan(\frac{y}{x}) \simeq \varphi_0 + \frac{\cos\varphi_0\delta y - \sin\varphi_0\delta x}{r_0}, \tag{2.42}$$

provided $r_0 \gg a$. Here φ_0 is the azimuthal angle of r_0, and a is the lattice constant. With $\delta x, \delta y = \pm\frac{a}{2}$, the accumulated phase is zero for a cell away from the laser centre.

Numerical simulation for the accumulated flux ϕ_{ij} is shown in Fig. 2.7, where an $l = 1$ LG laser drives the tunnelling of atoms along a loop enclosing the lattice centre that coincides with the laser centre. The flux is defined as $\phi_{i,j} = \arg(J_{i,j}) - \arg(J_{i,j+1}) + \arg(J_{i+1,j+1}) - \arg(J_{i+1,j})$, where the tunneling strength $J_{i,j}$ is given in Eq. (2.41). As shown in Fig. 2.7, the gauge field is non-zero within only a few cells around the centre. We would like to remark that even if the centre of the laser is slightly shifted from that of the lattice, it will not affect the results significantly, although some small fluctuations may appear around the solenoid. In a similar way, an LG laser drives tunnelling of atoms which are trapped in a ring lattice. For an $l = 1$ laser, the accumulated phase along the

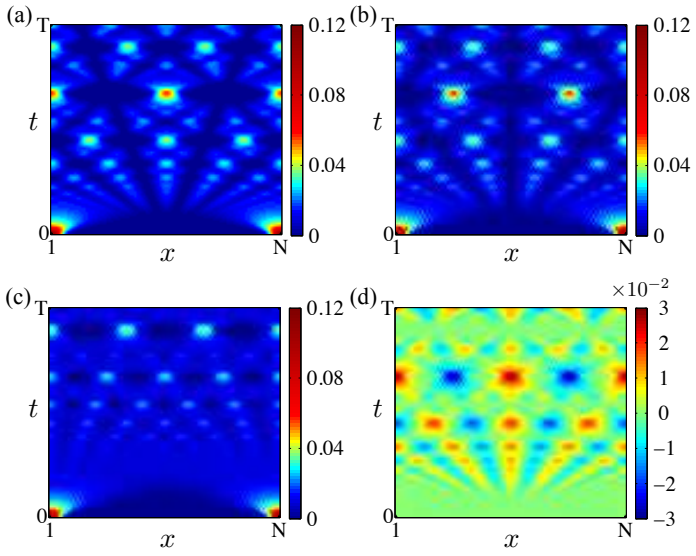

Figure 2.8: The time evolution of particle distributions for particles hopping around a loop formed by LG beams in a ring with $N_{\rm L} = 100$ sites under a zero gauge field (a), an Abelian U(1) field (b), or a non-Abelian SU(2) field ((c) and (d)).

ring is π. It is straightforward to extend to the SU(2) case, where ψ_s becomes a 2×1 column matrix to include the two sub-states $|g_1\rangle$ and $|g_2\rangle$ ($|e_1\rangle$ and $|e_2\rangle$) in $|g\rangle$ ($|e\rangle$) level [see Fig. 2.6(e)]. Two laser beams with $l = 0$ and $l = 1$ are employed to drive $|g_1\rangle$-$|e_2\rangle$ and $|g_2\rangle$-$|e_1\rangle$ transitions, respectively. To give a unitary hopping matrix for two spins, we should choose $l = 0$ and $l = 1$ lasers with the same amplitude to drive the spin-flipping transitions. It is satisfied when we apply an LG mode with $p = 0$, $l = 1$, and a superposition of two LG modes with $p = 0$, $l = 0$ and $p = 1$, $l = 0$. The non-Abelian tunneling matrix is then given by

$$\hat{J}_{ij} = \begin{pmatrix} 0 & |J_{ij}| \\ J_{ij} & 0 \end{pmatrix}, \tag{2.43}$$

where J_{ij} is given in Eq. (2.41).

For a 1D ring-shaped optical lattice as illustrated in Fig. 2.6(c), numerical simulations for spatial distributions of particle numbers are plotted in Fig. 2.8, where the particle numbers are shown as a percentage of the total number in the initially prepared BEC. We have chosen the lattice site number as $N_{\rm L} = 100$ and the time period T as 600 in unit of $E_R/\hbar$, where E_R is the recoil energy and the typical hopping is $J \simeq 0.05E_R$. With $E_R/\hbar = 2\pi \times 900$ Hz, the time scale is approximately in the range of 100 ms. Distinctly different interference pattens can be seen around $x = N_{\rm L}/2$ site for particles experiencing

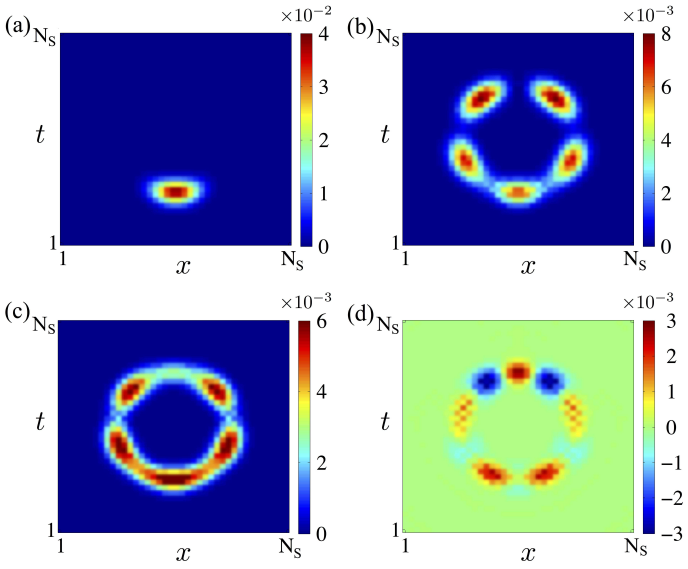

Figure 2.9: The time evolution of particle distributions for particles hopping around a loop formed by LG beams in a 2D square lattice with 40×40 sites.

a zero magnetic field as shown in (a), an Abelian U(1) gauge field as shown in (b), and a non-Abelian SU(2) gauge field as shown in (c)-(d). The interference fringes are closely related to the phase in our scheme. For an LG laser with $l = 1$, the accumulated phase along the circle is π. Since the atoms move along left or right path, the atoms from different paths will possess a different phase factor at the opposite site, giving a destructive interference. For an LG laser with $l = 0$, the phase is always zero, which resembles the system with particles moving in the absence of any gauge field. The atoms evolving along two different paths will possess the same phase factor at the opposite site, and the interference is destructive. The reason for the two subfigures in the SU(2) case is that two effective spins are involved in the SU(2) field. We plot an effective charge wave density (the sum of densities of the two effective spins) in (c) and an effective spin wave density (the difference of densities of the two effective spins) in (d), respectively. At the $N_{\mathrm{L}}/2$ site, a destructive (constructive) interference is always seen in (b) [(a)]. Two components appear with one colored red and the other blue, where the constructive interference occurs for one type (red).

For the 2D square lattice case as illustrated in Fig. 2.6(b), we can also prepare the initial state by loading a BEC around one plaquette. At one side, evolve the system, and detect the particle distributions at the opposite side. The initial state as shown in Fig. 2.9(a) is prepared with particles occupying a small area around $x = N_S/2$, $y = N_S/4$ with $N_S = 40$. Such an initial state can be achieved as a ground state of the system with

two lasers $l = 0$ and $l = 1$ switched on. After the initial state is prepared, we switch off the $l = 0$ and $l = 1$ lasers and turn on the following discussed corresponding LG beams at time $t = 0$ to drive the time evolution. For the U(1) Abelian field case as shown in Fig. 2.9(b), we turn on an $l = 1$ laser as illustrated in Fig. 2.6(d), and for the non-Abelian SU(2) field case as shown in Fig. 2.9 (c)-(d), we turn on two orthogonally polarized $l = 0$ and $l = 1$ lasers as illustrated in Fig. 2.6(e). Numerical simulations with time show that the angular momentum imparted by the LG beams results in a circular distributions of atoms. The particle number distribution at the opposite side of the circle from the initially prepared site again shows clear destructive interference in the case of the Abelian gauge field - the signature of the AB effect. As a concrete example, screenshots at time $t = 4000\hbar/E_R$ are given in Fig. 2.9 (b)-(d). The effect is similar to the ring geometry case.

Chapter 3

Topological Phases in One Dimensional Optical Lattice

Gauge fields are pivotal in our understanding of physics at all scales. At the highest energy scales known, the microscopic universe is governed by particles interacting with each other through the exchange of gauge bosons. At the largest length scales, our Universe is ruled by gravity, whose gauge structure suggests the existence of a particle called the graviton that mediates the gravitational force. At the mesoscopic scale, solid-state systems are subjected to gauge fields of different nature: materials can be immersed in external electromagnetic fields, but they can also feature emerging gauge fields in their low-energy description.

3.1 Su-Schrieffer-Heeger Model

In 1979, W.P. Su, J.R. Schrieffer, and A.J. Heeger gave the theoretical explanation for the soliton formation in long-chain polyenes [108]. Polyacetylene, $(CH)_x$, is a simple linear polymer formed as a chain of CH groups, as shown in Fig. 3.1. The separations between neighbor carbon atoms are around 1Å. In polyacetylene, the uniform array of carbon atoms is unstable. In fact, equilibrium is achieved only after the atoms shift from the equally spaced positions. This mechanism is known for Peierls distortion.

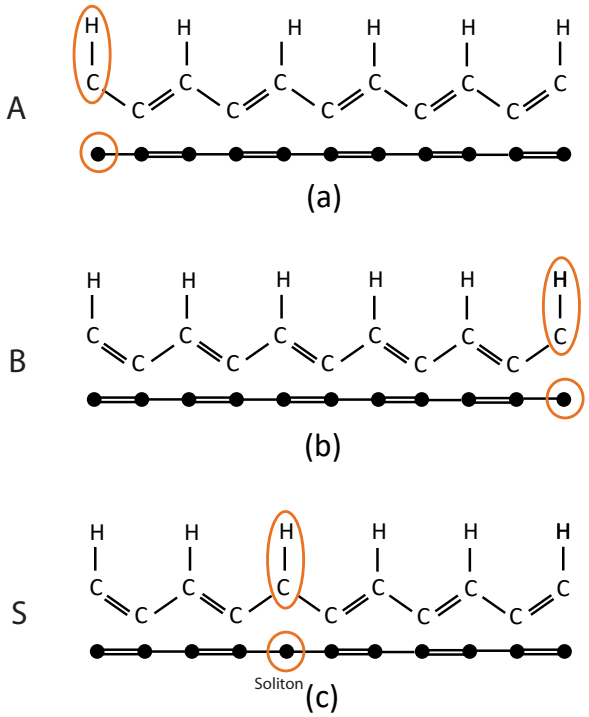

Figure 3.1: The dimerized trans-polyacetylene.

3.1.1 Peierls Distortion

The polyacetylene can be described as

$$H_{SSH} = H_\pi + H_{ph} + H_{\pi-ph}. \tag{3.1}$$

H_π represents the hopping of π electrons along the chain without spin flip. H_{ph} is the phonon Hamiltonian of the lattice. And $H_{\pi-ph}$ describes the interactions between electrons and phonons. The Hamiltonian for the free electron is

$$H_\pi = -t_0 \sum_{n,s} (\hat{c}^\dagger_{n+1,s}\hat{c}_{n,s} + \hat{c}^\dagger_{n,s}\hat{c}_{n+1,s}), \tag{3.2}$$

where $\hat{c}^\dagger_{n,s}$ and $\hat{c}_{n,s}$ describe the creation and annihilation of π electrons along the chain without spin flip. t_0 is the hopping amplitude for equally spaced crystal and s labels the spin orientation. The phonon Hamiltonian is

$$H_{ph} = \sum_n \frac{p_n^2}{2m} + \frac{K}{2}(u_{n+1} - u_n)^2, \tag{3.3}$$

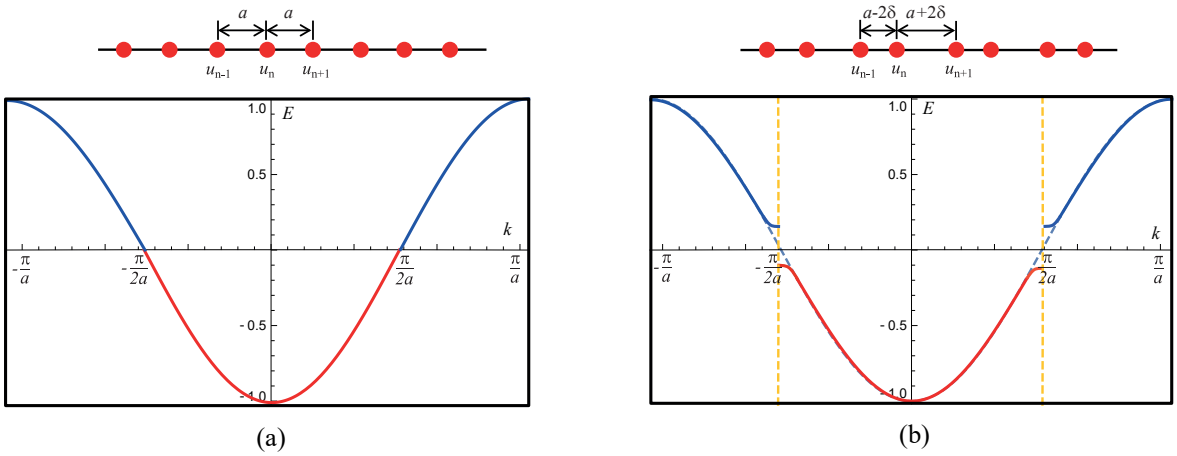

Figure 3.2: Energy band structures for electrons hopping in the crystal with (a) equal space and (b) unequal spaces.

where m is the mass of one unit of the chain, u_n is the displacement of the nth unit from its equilibrium position and p_n is the momentum conjugate to u_n. K represents an effective spring constant describing a harmonic approximation to the bond energy. The π-electron-phonon interaction is given by

$$H_{\pi-ph} = \alpha \sum_{n,s} (u_{n+1} - u_n)(\hat{c}^\dagger_{n+1,s}\hat{c}_{n,s} + \hat{c}^\dagger_{n,s}\hat{c}_{n+1,s}). \tag{3.4}$$

Here the linear terms in u_n is justified for the weak coupling.

Assuming that $m \to \infty$, one can treat the motion of the nuclei in a classical way. The dynamics of electrons is influenced by the coupling to phonons of the crystal. Because the electron-phonon coupling is invariant under spatial translations $2ma$, $m = \pm 1, \pm 2, \ldots$, the Brillouin zone is reduced to $-\frac{\pi}{2a} < k < \frac{\pi}{2a}$ and the energy band splits into two bands which are called valence and conduction bands as shown in Fig. 3.2(b). This band splitting effect is produced by the spontaneous symmetry-breaking of the translation symmetry. The ground state is spontaneously distorted to form a charge-density wave with $\langle u_n \rangle \neq 0$. To see how this spontaneous symmetry-breaking take places, we should find out the ground energy of the system. With the spatial translation invariance of $2ma$, the u_ns are constrained: $u_n \to \langle u_n \rangle = (-1)^n \delta$. δ can be regarded as the phonon field produced from crystal distortion. Therefore, the Hamiltonian Eq. (3.1) can be rewritten

as

$$H_{SSH}(\delta) = -\sum_{n,s}[t_0 + (-1)^n 2\alpha\delta](\hat{c}^\dagger_{n+1,s}\hat{c}_{n,s} + \hat{c}^\dagger_{n,s}\hat{c}_{n+1,s}) + 2NK\delta^2. \tag{3.5}$$

for a chain of N monomers in a crystal. Under the periodic boundary condition, one can make Fourier transformations in the reduced Brillouin zone

$$\hat{c}_{ks-} = \frac{1}{\sqrt{N}}\sum_{n,s} e^{-ikna}\hat{c}_{ns}, \qquad \hat{c}_{ks+} = -i\frac{1}{\sqrt{N}}\sum_{n,s} e^{-ikna}(-1)^n\hat{c}_{ns}. \tag{3.6}$$

for valence and conduction bands, respectively. After these transformations, the Hamiltonian reads

$$H_{SSH}(\delta) = \sum_{k,s}[\varepsilon_k(\hat{c}^\dagger_{ks+}\hat{c}_{ks+} - \hat{c}^\dagger_{ks-}\hat{c}_{ks-}) + \Delta_k(\hat{c}^\dagger_{ks+}\hat{c}_{ks-} + \hat{c}^\dagger_{ks-}\hat{c}_{ks+})] + 2NK\delta^2. \tag{3.7}$$

where $\Delta_k = 4a\delta\sin ka$, $\varepsilon_k = 2t_0\cos ka$. Finally, $H_{SSH}(\delta)$ can be diagonalized by making a Bogoliubov transformation:

$$\begin{aligned}\hat{a}_{ks-} &= \alpha_k\hat{c}_{ks-} - \beta_k\hat{c}_{ks+},\\ \hat{a}_{ks+} &= \beta_k\hat{c}_{ks-} + \alpha_k\hat{c}_{ks+},\end{aligned}$$

with $|\alpha_k|^2 + |\beta_k|^2 = 1$. Then we can get

$$H_{SSH}(\delta) = \sum_{k,s} E_k(\hat{n}_{ks+} - \hat{n}_{ks-}) + 2NK\delta^2, \tag{3.8}$$

where $E_k = (\varepsilon_k^2 + \Delta_k^2)^{1/2}$ and

$$\begin{aligned}\alpha_k &= \sqrt{\frac{1+\varepsilon_k/E_k}{2}},\\ \beta_k &= \sqrt{\frac{1-\varepsilon_k/E_k}{2}}\mathrm{sgn}(\Delta_k).\end{aligned}$$

In the half-filled case, the total energy of the system is

$$E_0(\delta) = -\frac{4Nt_0}{\pi}\int_0^{\pi/2}[1-(1-z^2)\sin^2 x]^{1/2}dx, \tag{3.9}$$

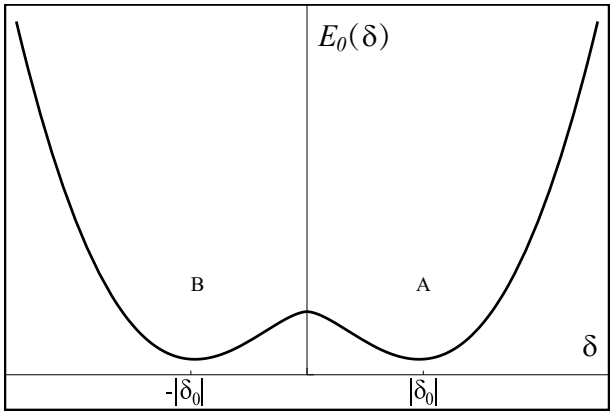

Figure 3.3: The total energy E_0 as a function of δ.

with $z = 2\alpha\delta/t_0$. For small δ

$$\frac{E_0(\delta)}{N} \approx -4\frac{t_0}{\pi} - \frac{2t_0}{\pi}[\ln(\frac{4}{z}) - \frac{1}{2}]z^2 + K\frac{t_0^2 z^2}{2\alpha^2}. \tag{3.10}$$

As $|z| \to 0$, the logarithmic term dominates and E_0 has a maximum at $\delta = 0$, which is consistent with Peierls theorem. For an assumed energy gap of $2\Delta = 1.4eV$ and parameters $\alpha = 4.1eV/\text{Å}$, $K = 21eV/\text{Å}^2$, and $t_0 = 2.5eV$, we can find the minimum energy mean-field distortion to be at $\delta_0 \approx 0.04$Å. As shown in Fig. 3.3, the two minima at $\delta = +|\delta_0|$ and $\delta = -|\delta_0|$ correspond to different phases A and B (Fig. 3.1(a) and (b)). The symmetric point at $\delta = 0$ is unstable. The symmetry breaking will lead to the system in either vacuum A or B, or both. For the first two cases, the phonon fields are constant, i.e., $\pm|\delta_0|$. If both A and B coexist in the crystal, then a boundary excitation can be yielded which is know as soliton [109]. The soliton continuously connects the phonon fields in both vacua. In Fig. 3.4, there are two constant phonon fields $\pm|\delta_0|$ corresponding to A and B phases. There are also two solitons $\pm\delta_s$ surviving at the boundary between A and B. In Fig. 3.1(c), one soliton is created at the interface. The phonon field of the soliton interpolates from B to A. In polyacetylene, the solitons are domain walls that separate regions with different vacua.

The dimerized chain shown above is natural in crystal. This effect is called Peierls instability or Peierls distortion. This is first pointed out by R. E. Peierl [110]. It states that a 1D equally spaced chain with one electron per ion is unstable. The distortion makes ions moves closer to one neighbor but further away from the other neighbor. In this way, the chain is formed alternately by long bonds and short bonds. The original

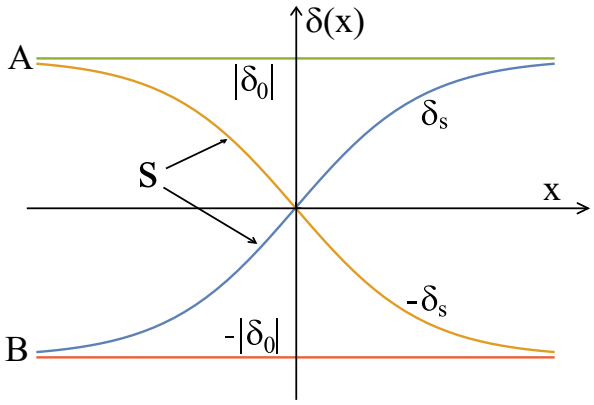

Figure 3.4: The two constant fields $\pm|\delta_0|$ correspond to two vacua A and B, respectively. The two kink fields $\pm\delta_s$ interpolate between A and B.

single band for equally spaced chain changes to separated two bands (see Fig. 3.2).

3.1.2 Topological Edge States

The soliton at the interface represents the topological difference between A and B. There also exist topological states at the lattices in Fig. 3.1(a) and (b). To visualize the topological states, we consider the SSH model in the real space. The SSH Hamiltonian can simply written as

$$H_{ssh} = \sum_n J_1 \hat{a}_n^\dagger \hat{b}_n + J_2 \hat{b}_n^\dagger \hat{a}_{n+1} + h.c., \tag{3.11}$$

where $\hat{a}_n^\dagger(\hat{b}_n^\dagger)$ and $\hat{a}_n(\hat{b}_n)$ are the creation and annihilation operators of particles on A(B) sublattice at the unit cell j. In this model, each unit cell is composed of two subsites, A and B. In general, the hopping terms in the unit cell J_1 and between neighbor cells J_2 are different. This enables the two band structure. Here, we assume $J_1 = 1 - \cos\varphi_\lambda$, $J_2 =$

$1+\cos\varphi_\lambda$. The above Hamiltonian can be written as

$$\begin{aligned} H_{ssh} &= \sum_{n=1}^{N} \begin{pmatrix} \hat{a}_n^\dagger & \hat{b}_n^\dagger \end{pmatrix} \begin{pmatrix} 0 & J_1 \\ J_1 & 0 \end{pmatrix} \begin{pmatrix} \hat{a}_n \\ \hat{b}_n \end{pmatrix} + \begin{pmatrix} \hat{a}_{n+1}^\dagger & \hat{b}_{n+1}^\dagger \end{pmatrix} \begin{pmatrix} 0 & J_2 \\ 0 & 0 \end{pmatrix} \begin{pmatrix} \hat{a}_n \\ \hat{b}_n \end{pmatrix} \\ &\quad + \begin{pmatrix} \hat{a}_n^\dagger & \hat{b}_n^\dagger \end{pmatrix} \begin{pmatrix} 0 & 0 \\ J_2 & 0 \end{pmatrix} \begin{pmatrix} \hat{a}_{n+1} \\ \hat{b}_{n+1} \end{pmatrix} \\ &= \sum_{n=1}^{N} \mathcal{M}\Psi_n^\dagger\Psi_n + \mathcal{T}^\dagger\Psi_{n+1}^\dagger\Psi_n + \mathcal{T}\Psi_n^\dagger\Psi_{n+1}, \end{aligned} \tag{3.12}$$

with

$$\mathcal{M} = \begin{pmatrix} 0 & J_1 \\ J_1 & 0 \end{pmatrix}, \mathcal{T} = \begin{pmatrix} 0 & 0 \\ J_2 & 0 \end{pmatrix}.$$

We make an ansatz for the edge state $\psi = \sum_n \lambda^n \xi$, where ξ is a 2 component spinor.

$$H_{ssh}\psi = E\psi. \tag{3.13}$$

From the above equation, we can have

$$(\mathcal{M} + \lambda\mathcal{T}^\dagger + \lambda^{-1}\mathcal{T})\xi = E\xi, \tag{3.14}$$

with $E = 0$ for edge state.

$$\mathcal{M} + \lambda\mathcal{T}^\dagger + \lambda^{-1}\mathcal{T} = \begin{pmatrix} 0 & J_1 + J_2\lambda \\ J_1 + J_2\lambda^{-1} & 0 \end{pmatrix}. \tag{3.15}$$

To solve Eq. (3.14), we should find appropriate λ for $\mathrm{Det}(\mathcal{M} + \lambda\mathcal{T}^\dagger + \lambda^{-1}\mathcal{T}) = 0$. Then we have

$$J_1J_2\lambda^2 + (J_1^2 + J_2^2)\lambda + J_1J_2 = 0, \tag{3.16}$$

with two solutions for λ: $\lambda_1 = -\frac{J_1}{J_2}$, $\lambda_2 = -\frac{J_2}{J_1}$. The wavefunction of edge state should decay along the lattice, so $|\lambda| < 1$. From this result we can know, when $|J_1| < |J_2|$, $|\lambda_1| < 1$; otherwise, $|\lambda_2| < 1$. This means that no matter $|J_1| < |J_2|$ or $|J_1| > |J_2|$, there are edge states at $E = 0$. This corresponds to the lattice in Fig. 3.5(a). There are no topological phase transitions in the lattice. However, the situation is different for (b). As $|J_1| < |J_2|$, there are degenerate edge states which localize at left and right ends of the lattice. But, if $|J_1| > |J_2|$, no edge states appear in the spectrum gap. Therefore, the lattice is in a non-topological phase.

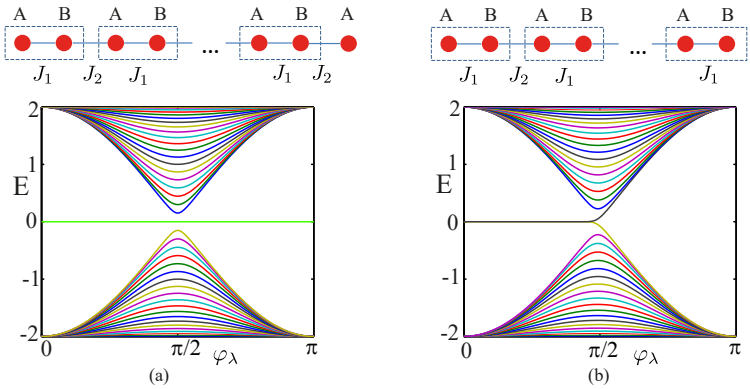

Figure 3.5: Lattice structure and the corresponding spectrum of SSH model.

3.2 Topological Quantum Number in Periodic Lattice

It is well known that a geometric phase is acquired by a slowly moving particle traversing adiabatically through a closed evolution path with a Hamiltonian governed by path-dependent parameters. If the system starts with one of the eigenstates of the system, the adiabatical evolution ensures that the system remains in the particular eigenstate of the system. The Berry's phase depends only on the geometry of the state space of the evolution path, and it is different from the phase arising from dynamical process.

In periodic lattice, the parameter space is naturally defined by the Brillouin zone where Berry's phase can be defined. In 1982, D.J. Thouless *et al.* showed that Hall conductivity of 2D electronic gas in periodic lattice is quantized [111]. Later, it was found that the Hall conductivity is actually related to the Berry's phase defined in the Brillouin zone of 2D periodic lattice [112, 113]. In 1989, J. Zak found that Berry's phase of electron moving in an inversion symmetric crystal is quantized [19]. This quantized Berry's phase is thereafter called Zak phase. In this section, we discuss Zak phase in the SSH model.

3.2.1 Berry's Phase in Periodic Lattice

It is well known from Bloch's theorem that periodic systems exhibit energy band structures. Within the independent particle approximation, the Hamiltonian for a particle in a crystal is

$$H = \frac{\hat{\boldsymbol{p}}^2}{2m} + V(\boldsymbol{r}), \tag{3.17}$$

where $V(\boldsymbol{r}+\boldsymbol{a}) = V(\boldsymbol{r})$ is the periodic potential with $\boldsymbol{a}$ the Bravais lattice vector. According to the Bloch's theorem, the eigenstates of the above Hamiltonian satisfy the boundary condition

$$\psi_{n\boldsymbol{k}}(\boldsymbol{r}+\boldsymbol{a}) = e^{i\boldsymbol{k}\cdot\boldsymbol{a}}\psi_{n\boldsymbol{k}}(\boldsymbol{r}). \tag{3.18}$$

where n is the band index, $\hbar\boldsymbol{k}$ is the crystal momentum. Eq. (3.18) means that the Bloch functions $\psi_{n\boldsymbol{k}}(\boldsymbol{r})$ obey $\boldsymbol{k}$-dependent boundary conditions. In order to define Berry's phase, one should require parameter-independent boundary conditions which means that all the eigenstates reside in the same Hilbert space. In order to do this, we should make a transformation to the Hamiltonian and eigenstates. The eigenstates can be written as $\psi_{n\boldsymbol{k}}(\boldsymbol{r}) = e^{i\boldsymbol{k}\cdot\boldsymbol{r}}u_{n\boldsymbol{k}}(\boldsymbol{r})$. Now the transformed eigentates $u_{n\boldsymbol{k}}(\boldsymbol{r})$ satisfy the periodic boundary conditions

$$u_{n\boldsymbol{k}}(\boldsymbol{r}+\boldsymbol{a}) = u_{n\boldsymbol{k}}(\boldsymbol{r}). \tag{3.19}$$

And the transformed Hamiltonian becomes

$$H(\boldsymbol{k}) = e^{-i\boldsymbol{k}\cdot\boldsymbol{r}}He^{i\boldsymbol{k}\cdot\boldsymbol{r}} = \frac{(\hat{\boldsymbol{p}}+\hbar\boldsymbol{k})^2}{2m} + V(\boldsymbol{r}). \tag{3.20}$$

In this way, we have the Hamiltonian $H(\boldsymbol{k})$ and corresponding eigenstates $|u_n(\boldsymbol{k})\rangle$. This Hamiltonian identifies the Brillouin zone as a parameter space where $\boldsymbol{k}$ and $\boldsymbol{k}+\boldsymbol{G}$ denote the same point ($\boldsymbol{G}$ is the reciprocal lattice vector). By making the phase choice such that $|\psi_n(\boldsymbol{k})\rangle = |\psi_n(\boldsymbol{k}+\boldsymbol{G})\rangle$ and considering Eq. (3.18) and Eq. (3.19), $|u_n(\boldsymbol{k})\rangle$ and $|u_n(\boldsymbol{k}+\boldsymbol{G})\rangle$ follow the phase relation

$$u_{n\boldsymbol{k}}(\boldsymbol{r}) = e^{i\boldsymbol{G}\cdot\boldsymbol{r}}u_{n\boldsymbol{k}+\boldsymbol{G}}(\boldsymbol{r}). \tag{3.21}$$

This gauge choice is called the periodic gauge [114]. Berry's phase is found to be

$$\gamma_n = \oint_{\mathcal{C}} d\boldsymbol{k}\cdot\langle u_n(\boldsymbol{k})|i\boldsymbol{\nabla}_{\boldsymbol{k}}|u_n(\boldsymbol{k})\rangle. \tag{3.22}$$

3.2.2 Zak Phase of SSH Model

In artificial materials, dimerized lattice is easy to be created. There are many systems have realized such dimerized structure, like optical and waveguide lattices [115, 116, 24]. In optical lattice, lasers with different frequencies can be employed to yield superlattice for cold atoms [117]. In Fig. 3.6, we show the optical superlattice realized in experiment which simulates the SSH model. The system is described by Eq. (3.11). In the last section, we have discussed the topological edge state of SSH model in real space. In this section, we study Zak phase of SSH model in the crystal momentum space. By performing

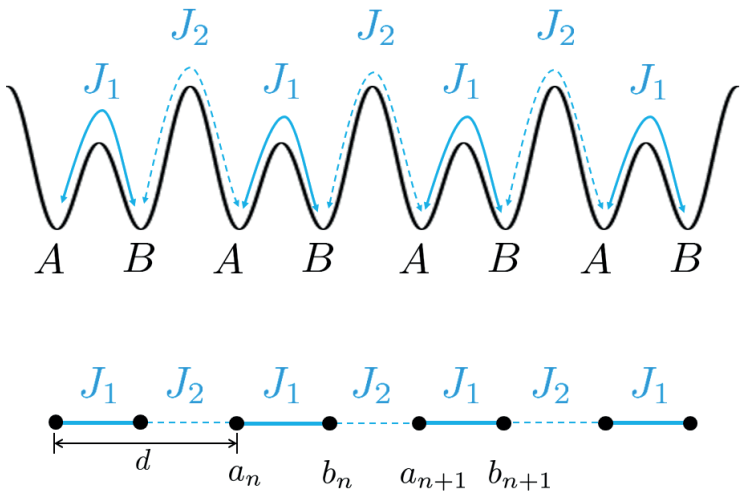

Figure 3.6: The sketch for superlattice. $J_{1,2}$ are the hopping amplitudes of cold atoms between neighbor potential wells.

the Fourier transformations,

$$\begin{aligned} \hat{a}_n &= \frac{1}{\sqrt{N}} \sum_k e^{ik\cdot nd} \hat{a}_k, \\ \hat{b}_n &= \frac{1}{\sqrt{N}} \sum_k e^{ik\cdot(n+\frac{1}{2})d} \hat{b}_k, \end{aligned} \tag{3.23}$$

where N is the number of the unit cells in the lattice, we can get

$$H_{ssh} = -\sum_k (\hat{a}_k^\dagger, \hat{b}_k^\dagger) H_{ssh}(k) \begin{pmatrix} \hat{a}_k \\ \hat{b}_k \end{pmatrix}, \tag{3.24}$$

with $H_{ssh}(k) = \boldsymbol{h}_k \cdot \boldsymbol{\sigma}$, $\boldsymbol{\sigma} = (\sigma_x, \sigma_y, \sigma_z)$. $\boldsymbol{h}_k = \big((J_1 + J_2)\cos\frac{kd}{2}, (J_2 - J_1)\sin\frac{kd}{2}, 0\big)$. One can solve the Schrödinger equation to get the two-component spinor eigenstates as

$$\mathbf{u}_{\pm,k} = \begin{pmatrix} \alpha_{\pm,k} \\ \beta_{\pm,k} \end{pmatrix} = \frac{1}{\sqrt{2}} \begin{pmatrix} \mp 1 \\ e^{-i\theta_k} \end{pmatrix}, \tag{3.25}$$

where $\theta_k = \arctan\frac{h_k^y}{h_k^x} = \arctan\frac{(J_1-J_2)\sin(\frac{kd}{2})}{(J_1+J_2)\cos(\frac{kd}{2})}$. The difference between J_1 and J_2 then induces a gap for the Bloch waves that leads to nontrivial topology. This nontrivial topology has a correspondence in real space, i.e., edge modes. With this two eigenvectors,

we can define Zak phase in the Brillouin zone as

$$\varphi_{Zak} = i \int_{-G/2}^{G/2} (\alpha_k^* \partial_k \alpha_k + \beta_k^* \partial_k \beta_k) dk. \tag{3.26}$$

Therefore, we can find that $\varphi_{Zak,-} = \varphi_{Zak,+} = \pi/2$ for $J_1 > J_2$ and $\varphi_{Zak,-} = \varphi_{Zak,+} = -\pi/2$ for $J_1 < J_2$. This two Zak phases for different lattice configurations represent the topological difference between them. It is protected by the intrinsic chiral symmetry of the system. We can change the parameters J_1 and J_2 such that the configuration of the lattice can be manipulated. When $J_1 = J_2$, the bandgap between up and low bands closes. In this situation, it returns to single band of homogeneous lattice. The difference between the Zak phases of ground bands for lattices $J_1 > J_2$ and $J_1 < J_2$ is π. This indicates the topological transition between different phases of SSH lattice. By choosing a different Fourier transformations comparing to Eq. (3.24), Zak phases can be 0 and π [118].

Berry's phase in solids [119] can be revealed by magneto-oscillatory effects which have been realized in graphene systems [120, 121]. However, the direct observation of Berry's phase is quite challenging in electronic systems. Adiabatic evolution in the crystal momentum space typically acquires dynamical phase. In general, to distinguish Berry's phase from the dynamical phase is a difficult task. However, Zak phase can be simulated in many interesting systems, such as optical superlattice [117, 13], photonic crystal [25, 27]. Direct measurement of Berry's phase has been reported in optical superlattice using a combination of Bloch oscillation and Ramsey interferometry [117]. One can also measure the reflection phase to indicate Zak phase in 1D photonic crystal [25].

3.2.3 Physical Observable Corresponding to Zak Phase

In topological systems, the topological invariants usually correspond to some physical observables. For example, in 2D electron gases, the Hall conductivity is related to the Chern number [111]. In 1993, King-Smith and Vanderbilt pointed out that Zak phase is related to macroscopic polarization in crystalline dielectrics [21].

Without loss of generality, we suppose that the time-varying potential depends on a set of parameters $\mathbf{R}(t)$. The Schödinger equation for the time-dependent wave function $|\psi(t)\rangle$ is

$$i\hbar\partial_t|\psi(t)\rangle = H(t)|\psi(t)\rangle. \tag{3.27}$$

Suppose that $|n(t)\rangle$ are instantaneous eigenvectors of $H(t)$, so

$$|\psi(t)\rangle = \sum_n e^{-i\int_0^t dt' E_n(t')/\hbar} a_n(t)|n(t)\rangle. \tag{3.28}$$

Substitute the above equation to the Eq. (3.27) and we have

$$\dot{a}_n(t) = -\sum_m a_m(t)\langle n(t)|\partial_t|m(t)\rangle e^{-i\int_0^t dt'(E_m(t')-E_n(t'))/\hbar}. \tag{3.29}$$

Under the parallel transport condition, i.e.,

$$\langle n(t)|\partial_t|n(t)\rangle = \dot{\mathbf{R}}(t)\langle n(t)|\frac{\partial}{\partial \mathbf{R}}|n(t)\rangle = 0. \tag{3.30}$$

We denote the wave functions satisfying above condition as $|\tilde{n}\rangle$. If the time evolution is adiabatic, i.e., $\dot{\mathbf{R}}(t) = 0$, we have $\dot{a}_n(t) =$ to zeroth order. To first-order correction, for $m \neq n$,

$$\partial_t a_m(t) = -\langle \tilde{m}|\partial_t|\tilde{n}\rangle e^{-i\int_0^t dt'(E_n(t')-E_m(t'))/\hbar}. \tag{3.31}$$

After integrating above equation by parts, one has

$$a_m = -i\hbar\frac{\langle \tilde{m}|\partial_t|\tilde{n}\rangle}{E_n - E_m} e^{-i\int_0^t dt'(E_n(t')-E_m(t'))/\hbar}. \tag{3.32}$$

Finally, to first order, the wavefunction is

$$|\psi(t)\rangle = e^{-i\int_0^t dt' E_n(t')/\hbar}(|\tilde{n}\rangle - i\hbar\sum_{m\neq n}\frac{\langle \tilde{m}|\partial_t|\tilde{n}\rangle}{E_n - E_m}|\tilde{m}\rangle). \tag{3.33}$$

We now consider a slowly varying time-periodic potential which satisfies $H(t+T) = H(t)$. We discuss the problem by considering the eigenstates $\{|u_n(k,t)\rangle\}$ of $H(k,t)$ (see Eq. (3.20)). Therefore, from Eq. (3.33) the wave function is given as

$$|u_n\rangle - i\hbar\sum_{m\neq n}\frac{|u_m\rangle\langle u_m|\partial/\partial t|u_n\rangle}{E_n - E_m}. \tag{3.34}$$

Now we also want to know the velocity of particle. From Heisenberg equation we can get that $\boldsymbol{v} = \dot{\boldsymbol{r}} = (i/\hbar)[H, \boldsymbol{r}]$. Here in the k representation as defined in Eq. (3.20), we can

have

$$\begin{aligned} \boldsymbol{v}(\boldsymbol{k}) &= \frac{i}{\hbar} e^{-i\boldsymbol{k}\boldsymbol{r}}[H, \boldsymbol{r}]e^{i\boldsymbol{k}\boldsymbol{r}} \\ &= \frac{1}{\hbar}\frac{\partial H}{\partial k}, \end{aligned} \tag{3.35}$$

where we use $\boldsymbol{r} = i\partial/\partial\boldsymbol{k}$. The average velocity for a given k is

$$v_n(k) = \frac{1}{\hbar}\frac{\partial E_n(k)}{\partial k} - i\sum_{m\neq n}\left(\frac{\langle u_n|\partial H/\partial k|u_m\rangle\langle u_m|\partial/\partial t|u_n\rangle}{E_n - E_m} - \text{c.c.}\right), \tag{3.36}$$

where c.c. represents the complex conjugate. To simplify above equation, we have

$$\begin{aligned} \langle u_n|\frac{\partial H(k)}{\partial k}|u_m\rangle &= \langle u_n|\frac{\partial \sum_l E_l|u_l\rangle\langle u_l|}{\partial k}|u_m\rangle \\ &= \sum_l\left(\frac{\partial E_l}{\partial k}\langle u_n|u_l\rangle\langle u_l|u_m\rangle + E_l\langle u_n|\frac{\partial|u_l\rangle}{\partial k}\langle u_l|u_m\rangle + E_l\langle u_n|u_l\rangle\frac{\partial\langle u_l|}{\partial k}|u_m\rangle\right) \\ &= (E_m - E_n)\langle u_n|\frac{\partial}{\partial k}|u_m\rangle. \end{aligned} \tag{3.37}$$

Thus, the average velocity is

$$v_n(k) = \frac{1}{\hbar}\frac{\partial E_n(k)}{\partial k} - i(\langle\frac{\partial u_n}{\partial k}|\frac{\partial u_n}{\partial t}\rangle - c.c.). \tag{3.38}$$

The second term is just the Berry curvature Ω^n_{kt} defined in the time-momentum space. So $v_n(k) = \frac{1}{\hbar}\frac{\partial E_n(k)}{\partial k} - \Omega^n_{kt}$. The current of the system can be derived by taking integration over the Brilouin zone. In such situation, only the second term in Eq. (3.38) is nonzero. The induced adiabatic current is given by

$$j_c = -\frac{1}{2\pi}\sum_n\int_{B.Z.} dk\Omega^n_{kt}. \tag{3.39}$$

The sum is taken over the filled bands. With the above result, the polarization difference in crystalline solids [21] is

$$\begin{aligned} \Delta P &= -e\int_0^T dt j_c \\ &= \frac{e}{2\pi}\sum_n\int_0^T dt\int_{B.Z.} dk\Omega^n_{kt}. \end{aligned} \tag{3.40}$$

With this, King-Smith and Vanderbilt defined the electric polarization of crystalline solid as $P = -eq_n$. So Zak phase, adiabatic pump and polarization have close relation. Recently, the particle pumping is realized in many groups with cold atoms in optical lattices [12, 14].

3.3 Extended SSH Model

We have studied the SSH model in the dimerized lattice and the Zak phase. SSH lattice has only two energy bands. And the topological phase transition takes place when the bandgap closes. To investigate more general situations, we would like to consider the system with higher energy bands. A simple extension to SSH model is to allow for more subsites in every unit cell. We here discuss the extended SSH model with four sublattices.

3.3.1 Three-Band Model: Aharonov-Bohm Cage

Generalizing the dimerized lattice to more complex superlattice is nontrivial. As shown in Fig. 3.7(a), we consider a 1D optical lattice with three subsites A, B, C in a cell. This lattice is topologically nontrivial. It can produce fractional charges which are related to the symmetry and topology of the system [122, 123]. Here we show that the next-nearest-neighbor (NNN) hopping can lead to interesting effect. In Fig. 3.7(a), J_1 and J_2 are the NN tunnelings for c_{n-1} and a_n, a_n and b_n, respectively. They are tuned by the potential height between the wells. The tunneling between b_n and c_n is vanishing because of large height between them. However, the long-range hopping can be engineered via laser-assisted tunneling which is used to generate artificial gauge field [88, 71]. J_3 is the NNN hopping from b_{n-1} to a_n, and J_4 is the one from a_n and c_n. Because of the laser driving, J_3 and J_4 contain phase factors. Fig. 3.7(b) shows the equivalent structure of the long-range hopping driven lattice. This rhombic lattice has been studied in photonic lattice [124, 125]. It can be reduced to SSH model. For example, when $J_1 = J_4 = 0$, it is SSH lattice for the upper branch. If $J_2 = J_3 = 0$, SSH lattice is formed for the lower branch. For general situation, there are loops in the lattice.

The Hamiltonian of this system can be written as

$$\begin{aligned} H = \quad & \sum_n J_1 \hat{a}_n^\dagger \hat{c}_{n-1} + J_2 \hat{b}_n^\dagger \hat{a}_n + J_3 \hat{a}_n^\dagger \hat{b}_{n-1} + J_4 \hat{c}_n^\dagger \hat{a}_n + h.c. \\ & + \Delta_a \hat{a}_n^\dagger \hat{a}_n + \Delta_b \hat{b}_n^\dagger \hat{b}_n + \Delta_c \hat{c}_n^\dagger \hat{c}_n. \end{aligned} \tag{3.41}$$

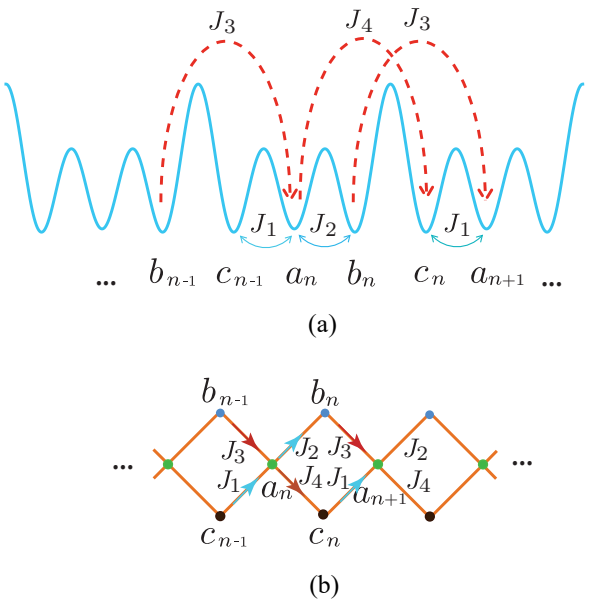

Figure 3.7: The equivalence between (a) long-range hopping of three-band extended SSH model and (b) rhombic lattice.

where $\hat{\alpha}_n^\dagger$ and $\hat{\alpha}_n$ are operators for creating and annihilating atoms at the nth cell of subsites α with $\alpha = a, b, c$. Δ_α are the chemical potential of these subsites. We can employ the artificial gauge field from Raman transition process to study flat band in 1D optical lattice.

The dynamical equations can be written as

$$\begin{aligned} i\dot{a}_n &= \Delta_a a_n + J_1 c_{n-1} + J_3 b_{n-1} + J_2^* b_n + J_4^* c_n, \\ i\dot{b}_n &= \Delta_b b_n + J_2 a_n + J_3^* a_{n+1}, \\ i\dot{c}_n &= \Delta_c c_n + J_1^* a_{n+1} + J_4 a_n. \end{aligned} \tag{3.42}$$

The solutions for above equations have plane wave form, i.e., $a_n = a(t)e^{ikn}$, $b_n = b(t)e^{ikn}$, $c_n = c(t)e^{ikn}$. Therefore, we can rewrite the equations as

$$\begin{aligned} i\dot{a}(t) &= \Delta_a a(t) + (J_1 e^{-ik} + J_4^*)c(t) + (J_3 e^{-ik} + J_2^*)b(t), \\ i\dot{b}(t) &= \Delta_b b(t) + (J_2 + J_3^* e^{ik})a(t), \\ i\dot{c}(t) &= \Delta_c c(t) + (J_4 + J_1^* e^{ik})a(t). \end{aligned} \tag{3.43}$$

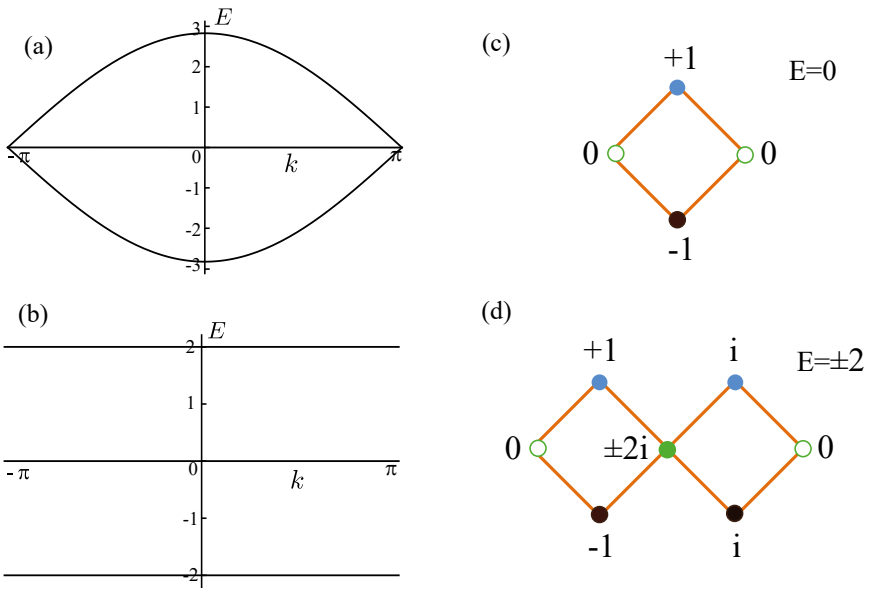

Figure 3.8: Energy bands with (a) $\theta = 0$ and (b) $\theta = \pi$ in rhombic lattice. (c) denotes the localized eigenstate for the flat band in (a). (d) represents the localized eigenstates for flat bands with $E = \pm 2$ in (b). Other parameters are $J_1 = J_2 = J_3 = J_4 = 1, \phi = 0$.

Assume $a(t), b(t), c(t) \sim e^{iEt}$, we can get the equation

$$\begin{aligned}(E+\Delta_a)(E+\Delta_b)(E+\Delta_c) &= (E+\Delta_b)[|J_1|^2+|J_4|^2+2|J_1||J_4|\cos(\theta-k)] \\ &\quad +(E+\Delta_c)[|J_2|^2+|J_3|^2+2|J_2||J_3|\cos(\phi-k)].\end{aligned} \tag{3.44}$$

where we assume $J_1 J_4 = |J_1||J_4|e^{i\theta}$, $J_2 J_3 = |J_2||J_3|e^{i\phi}$. θ and ϕ is related to the artificial gauge fields in the optical lattice. To simplify the discussion, we consider the case with $\Delta_a = \Delta_b = \Delta_c = 0$.

The band energies are: $0, \pm\sqrt{J_1^2+J_2^2+J_3^2+J_4^2+2J_1J_4\cos(\theta-k)+2J_2J_3\cos(\phi-k)}$. The dispersionless mode is localized state. The origin of such localized state is the effect of destructive interference. The other two modes are delocalized. The bandgap between up and low bands is

$$\Delta_k = 2\sqrt{P_0+2P_1\cos(\eta-k)}. \tag{3.45}$$

where $P_0 = J_1^2+J_2^2+J_3^2+J_4^2$, $P_1 = \sqrt{J_1^2J_4^2+J_2^2J_3^2+2J_1J_2J_3J_4\cos(\theta-\phi)}$ and $\eta = \arccos\frac{A}{\sqrt{A^2+B^2}}$ with $A = |J_1J_4|\cos\theta+|J_2J_3|\cos\phi$, $B = |J_1J_4|\sin\theta+|J_2J_3|\sin\phi$. The bandgap closes when $\theta-\phi=0$ and $|J_1|=|J_4|, |J_2|=|J_3|$. And the critical momentum

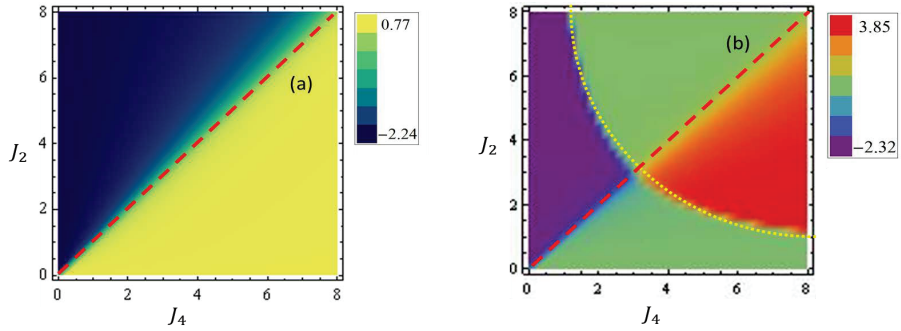

Figure 3.9: Zak phase for (a) the lowest band and (b) the first excited band changing with J_2 and J_4. $J_1 = J_3 = 3$ is assumed.

is $k_c = \theta + \pi$. The interesting result is the flat band $\lambda = 0$ [126]. In Fig. 3.8(a) and (b), we present the energy bands for $\theta = 0$ and $\theta = \pi$, respectively, with $J_1 = J_2 = J_3 = J_4 = 1, \phi = 0$. Interestingly, when $\theta = 0$, only the middle band is the flat band. However, when $\theta = \pi$, the three energy bands become flat. The eigenstates corresponding to the flat bands in (a) and (b) are localized. The localized eigenstates are shown in Fig. 3.8(c) and (d). This destructive interference effect is also known for Aharonov-Bohm cage and can be simulated with the artificial gauge field [127].

3.3.2 Four-Band Model

We consider the case of four sublattices in a unit cell

$$\begin{aligned} H_{4b} = \quad & -\sum_n (J_1 \hat{a}_n^\dagger \hat{b}_n + J_2 \hat{b}_n^\dagger \hat{c}_n + J_3 \hat{c}_n^\dagger \hat{d}_n + J_4 \hat{d}_n^\dagger \hat{a}_{n+1} + h.c.) \\ & -\sum_n (\Delta_1 \hat{a}_n^\dagger \hat{a}_n + \Delta_2 \hat{b}_n^\dagger \hat{b}_n + \Delta_2 \hat{c}_n^\dagger \hat{c}_n + \Delta_1 \hat{d}_n^\dagger \hat{d}_n). \end{aligned} \tag{3.46}$$

J_i are the hoppings between different subsites. Δ_1 and Δ_2 are the energy offsets or chemical potentials. The energy offset is chosen such that the unit cell is inversion

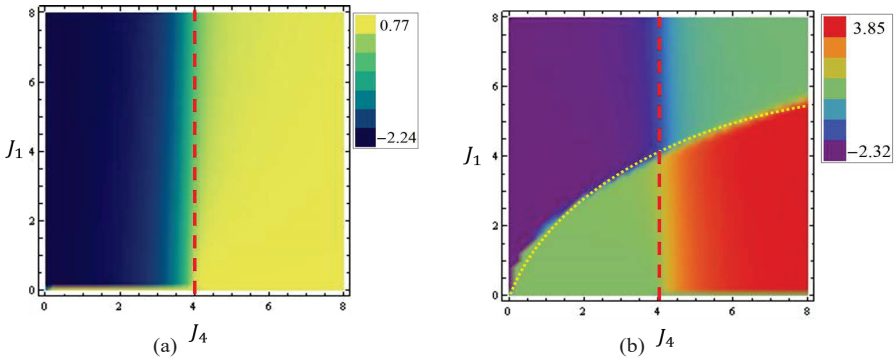

Figure 3.10: Zak phase for the lowest band (a) and the first excited band (b) changes with J_1 and J_4. Here $J_2 = 4$.

symmetric. With the periodic boundary conditions, we can make Fourier transformations

$$\begin{aligned}
\hat{a}_n &= \frac{1}{\sqrt{N}} \sum_k e^{iknd\tilde{}} \hat{a}_k, \\
\hat{b}_n &= \frac{1}{\sqrt{N}} \sum_k e^{ik(nd\tilde{}+d\tilde{}/4)} \hat{b}_k, \\
\hat{c}_n &= \frac{1}{\sqrt{N}} \sum_k e^{ik(nd\tilde{}+d\tilde{}/2)} \hat{c}_k, \\
\hat{d}_n &= \frac{1}{\sqrt{N}} \sum_k e^{ik(nd\tilde{}+3d\tilde{}/4)} \hat{d}_k,
\end{aligned} \tag{3.47}$$

where $\tilde{d}$ is the length of unit cell in the four-band lattice. Therefore, $H_{4b} = \sum_k \Psi_k^\dagger H_{4b}(k) \Psi_k$, with $\Psi_k = (\hat{a}_k, \hat{b}_k, \hat{c}_k, \hat{d}_k)^T$

$$H_{4b}(k) = - \begin{pmatrix} \Delta_1 & J_1 e^{i\phi} & 0 & J_4 e^{-i\phi} \\ J_1 e^{-i\phi} & \Delta_2 & J_2 e^{i\phi} & 0 \\ 0 & J_2 e^{-i\phi} & \Delta_2 & J_3 e^{i\phi} \\ J_4 e^{i\phi} & 0 & J_3 e^{-i\phi} & \Delta_1 \end{pmatrix}, \tag{3.48}$$

with $\phi = k\tilde{d}/4$.

We assume $\Delta_1 = \Delta_2 = 0$ and study the influence of parameters $J_{1,2,3,4}$ to Zak phase. At first, we consider $J_1 = J_3 = C$ (C is a constant), J_2 and J_4 can be changed (as shown in Fig. 3.9). When $J_2 = J_4$, the lowest band and the first excited band touch (red-dashed line in (a)). We see that Zak phase for the lowest band changes abruptly from $J_2 > J_4$ to

$J_2 < J_4$. The bandgap between the first excited band and the band above closes along the yellow-dotted line in (b). Therefore, Zak phase for the first excited band changes when it touches with upper or lower band. Then, we let J_1, J_3, J_4 be variables and J_2 is fixed. We assume $J_1 = J_3$. From Fig. 3.10(a), Zak phase for the lowest band is independent of J_1. But for the second lowest band, Zak phase varies with J_1.

In Fig. 3.11, we consider the role of energy offset Δ_1, Δ_2. When J_1 and J_3 are very small, there is a critical value for J_2. Below that value, the lowest band has only one Zak phase in the whole range of J_4. As J_1 and J_3 increase, this critical value decreases. When J_1 and J_3 are large enough, there are two Zak phases in the whole range of J_2 (Fig. 3.11(b)). As J_1 and J_3 increase continuously, there is linear relationship at the boundary of two Zak phases between J_2 and J_4 (Fig. 3.11(c) and (d)).

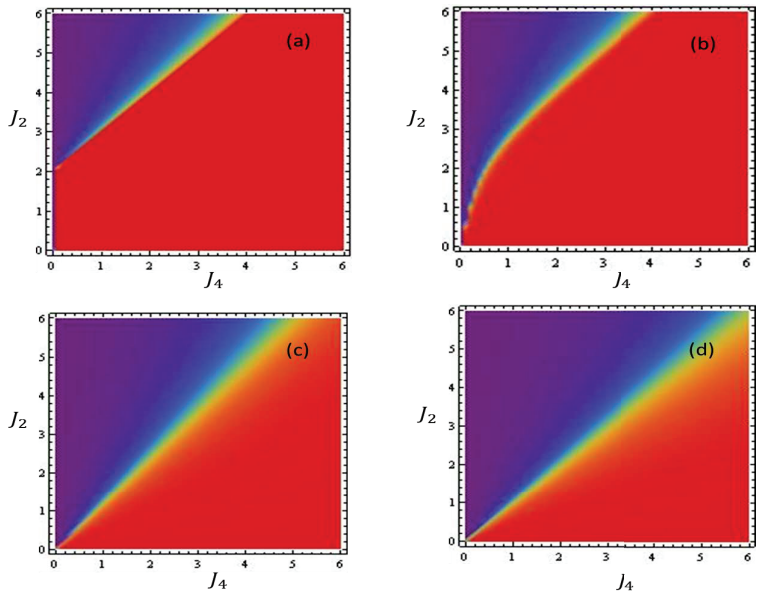

Figure 3.11: Zak phase of the ground band with $\Delta_1 = 0$, $\Delta_2 = 2$ under different J_1, J_3. (a) $J_1 = J_3 = 0.02$. (b) $J_1 = J_3 = 1$. (a) $J_1 = J_3 = 10$. (d) $J_1 = J_3 = 100$.

3.3.3 Edge States and Topological Phase Transitions

The four-band extended SSH model Eq. (3.46) can be rewritten as

$$H_{4b} = \sum_{n=1}^{N} \tilde{\mathcal{M}} \Psi_n^\dagger \Psi_n + \tilde{\mathcal{T}}^\dagger \Psi_{n+1}^\dagger \Psi_n + \tilde{\mathcal{T}} \Psi_n^\dagger \Psi_{n+1}, \tag{3.49}$$

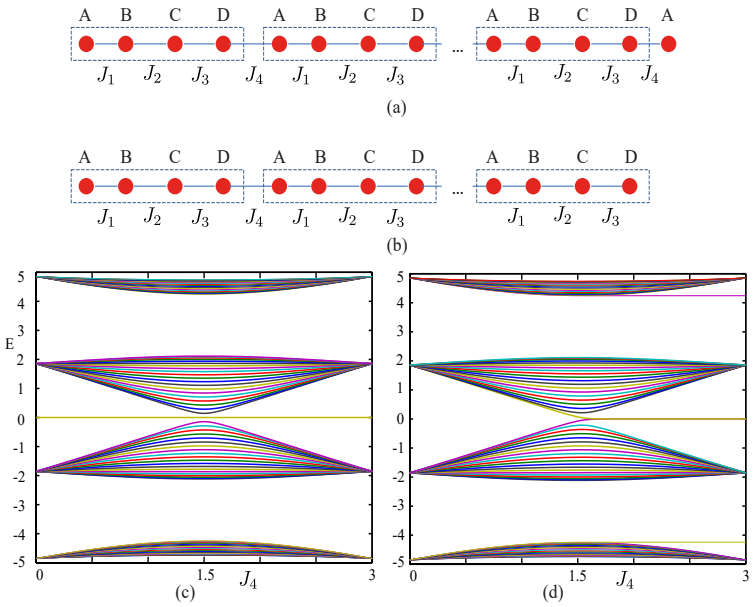

Figure 3.12: Four-band extended SSH model with (a) and (b) two lattice structures. The corresponding band structures are shown in (c) and (d). $J_1 = 3 - J_4, J_2 = J_3 = 3$.

with $\Psi_n^\dagger = (\hat{a}_n^\dagger, \hat{b}_n^\dagger, \hat{c}_n^\dagger, \hat{d}_n^\dagger)$ and

$$\tilde{\mathcal{M}} = \begin{pmatrix} 0 & J_1 & 0 & 0 \\ J_1 & 0 & J_2 & 0 \\ 0 & J_2 & 0 & J_3 \\ 0 & 0 & J_3 & 0 \end{pmatrix}, \tilde{\mathcal{T}} = \begin{pmatrix} 0 & 0 & 0 & 0 \\ 0 & 0 & 0 & 0 \\ 0 & 0 & 0 & 0 \\ J_4 & 0 & 0 & 0 \end{pmatrix}.$$

Following the procudure Eq. (3.13) and Eq. (3.14), in the open boundary conditions we have

$$J_1 J_2 J_3 J_4 \lambda^2 - (J_1^2 J_3^2 + J_2^2 J_4^2)\lambda + J_1 J_2 J_3 J_4 = 0, \tag{3.50}$$

with two solutions for λ: $\lambda_1 = \frac{J_1 J_3}{J_2 J_4}$, $\lambda_2 = \frac{J_2 J_4}{J_1 J_3}$. This corresponds to the lattice structure shown in Fig. 3.12(a). We can see that both $|J_1 J_3| < |J_2 J_4|$ and $|J_1 J_3| > |J_2 J_4|$ ensure edge states at $E = 0$ (see the spectrum in (c)). For the lattice Fig. 3.12(b), only $|J_1 J_3| < |J_2 J_4|$ makes the zero modes appear (as shown in (d)). For a general lattice, we can get the zero modes condition: $\prod_{i=\text{odd}} J_i = \prod_{j=\text{even}} J_j$.

In the four-band model, we consider four lattice structures: (I) $J_1 \ll J_2 = J_3 = J_4$, (II) $J_2 \ll J_1 = J_3 = J_4$, (III) $J_3 \ll J_1 = J_2 = J_4$, and (IV) $J_4 \ll J_1 = J_2 = J_3$, as shown in Fig. 3.13(a). The unit cells are chosen depending on the hopping parameters.

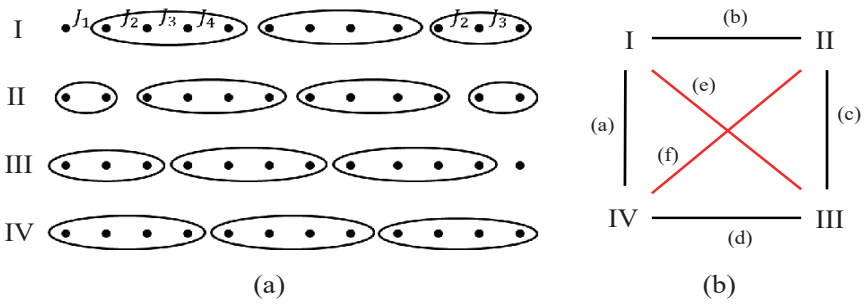

Figure 3.13: (a) Four different lattices depending on different choices of the unit cell. (b) Transitions between different lattice structures by changing NN hopping parameters (black lines) and NNN hopping parameters (red lines).

Fig. 3.13(b) represents the possible transitions between different lattice structures. The corresponding energy spectrums are plotted on Fig. 3.14. We can find that (II) has two degenerate edge states between the two lowest bands. For (I) and (III), there is one edge state between lowest two bands. The lattice of (IV) does not have edge state. Therefore, it is a topologically trivial lattice.

Now we discuss the transitions between different lattice structures. For the cases ((a)-(d) in Fig. 3.14), changing in band structure makes the number of zero modes different. This is same to the claim of S. Ganeshan *et al.* that zero mode is a topological invariant in Aubry-André-Harper (AAH) model [128]. The hopping parameters in AAH model have definite forms. The variation in lattice structure only involves topological changing of two middle bands. Therefore, in the AAH model, zero modes can indicate topological phases. However, in the extended four-band SSH model, there are energy degeneracies between the lowest bands (see Fig. 3.14(e) and (f)). In (e), we set $J_3 = 3 - J_1, J_2 = J_4 = 3$ and let J_1 varies from 0 to 3. The cases for $J_1 = 0$ and $J_1 = 3$ mirror symmetric. This can be seen from (I) and (III) in Fig. 3.13(a). The edge states at the ends of lattice are swapped when J_1 changes. For (f), the topological structures of the bands are different. The topological change does not involve zero modes, which signifies a different topological transition. Therefore, there are two kinds of topological transitions in this four-band lattice. This can be seen from the sum of Zak phases of the lowest two bands $\varphi_{\text{zak}}^{\text{sum}}$, as shown in Fig. 3.15. For the cases from (a) to (d) involving zero modes, the differences of $\varphi_{\text{zak}}^{\text{sum}}$ are π around the phase transition point. However, for (e) and (f), they are 2π.

In this chapter, we discussed the Zak phases for bulk states (Bloch states) and topological edge states in closed boundary conditions and open boundary conditions, respectively.

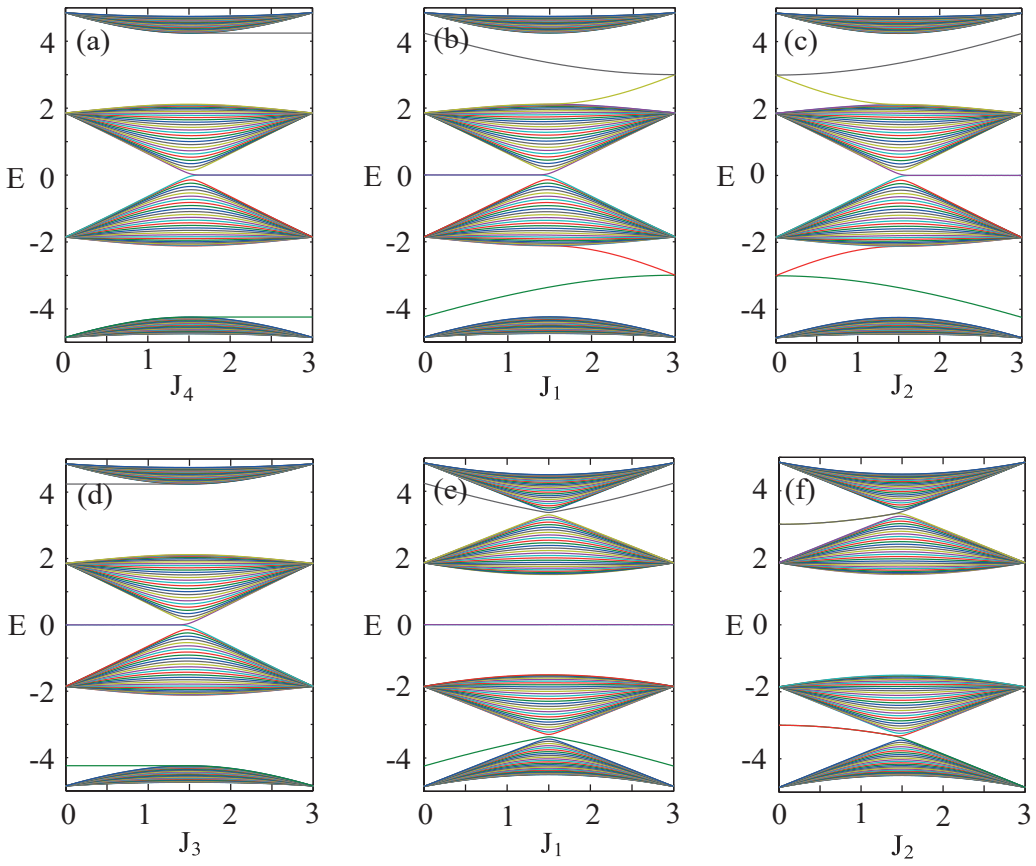

Figure 3.14: Energy spectrum of the four-band extended SSH lattice with open boundary conditions. The hopping parameters are chosen as: (a) $J_1 = 3 - J_4, J_2 = J_3 = 3$, (b) $J_2 = 3 - J_1, J_3 = J_4 = 3$, (c) $J_3 = 3 - J_2, J_1 = J_4 = 3$, (d) $J_4 = 3 - J_3, J_1 = J_2 = 3$, (e) $J_3 = 3 - J_1, J_2 = J_4 = 3$, (f) $J_4 = 3 - J_2, J_1 = J_3 = 3$.

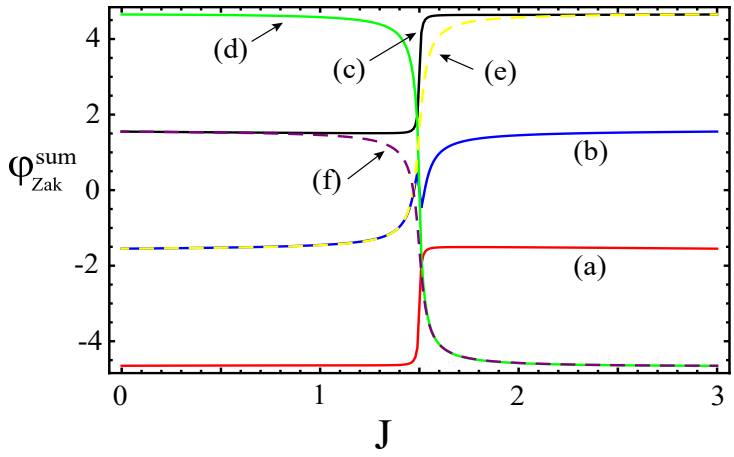

Figure 3.15: The sum of Zak phases for the lowest two bands corresponding to plots in Fig. 3.14. J is the hopping for specific cases. (a)-(d) show that the change of $\varphi_{\text{zak}}^{\text{sum}}$ because of energy degeneracies between middle bands. (e) and (f) show the change of $\varphi_{\text{zak}}^{\text{sum}}$ coming from energy degeneracies between lowest two band.

The Zak phase can be directly observed via guiding atoms adiabatically through Brillouin zone [117]. For the photonic crystal with the dimerized lattice structure, surface impedance of incident photons can be related to Zak phase [129]. Another way to reveal the relation between Zak phase and the transport of particle is studied by considering the decay in SSH lattice [28]. The first moment of the distribution of the dissipated particles, i.e., the average displacement, is found to be proportional to Zak phase. Recently, this effect has been realized in experiment [24]. For the extended SSH model, e.g., four-band model has also been discussed [130]. The topological phases in extended four-band SSH model are symmetry-protected [131]. The topological origin can be understood from the Majorana basis [128]. Because of the various topological phase transitions, it might be interesting to consider the topological pumping with the extended SSH model.

Chapter 4

Winding Number and Geometric Phase in Spin Chain

We have discussed quantized Berry's phase in inversion symmetric 1D periodic lattice in previous chapter. In this chapter, we study Berry's phase in spin-1/2 chain. The universal properties of phase transitions can be explored by geometric phase which was first proposed by S.L. Zhu in XY model [62]. He found that the derivative of geometric phase (DGP) with respect to external magnetic field diverges at critical points. And the finite-size scaling of DGP reveals the universality of phase transition. Such geometric phase is acquired by spin rotations. However, in the spin chain with periodic lattice, one can also find a Brillouin zone and geometric phase can be defined there. This geometric phase defined in Brillouin zone is proportional to winding number. Therefore, we use the winding number to characterize the topological invariant in the crystal momentum space. In this chapter, we focus on the spin chain with multispin interactions. Because of the multispin interactions, the ground states can have topological orders [132, 133]. It is also found that these systems can be topologically characterized [63, 47].

4.1 Winding Number in Generalized Ising Model

Highly entangled cluster states are useful resource for measurement-based quantum computation. Cluster states are defined as the unique state satisfying $C_j|\Psi_C\rangle = +1|\Psi_C\rangle$, where the stabilizer operators $C_j = \sigma_j^x \sigma_{j+1}^z \sigma_{j+2}^x$. The cluster state $|\Psi\rangle$ is a $\mathbb{Z}_2 \times \mathbb{Z}_2$ symmetry protected topological state. However, this symmetry can be broken under perturbation. When other interaction is introduced, the system exhibits phase transitions [134, 135, 132, 133]. We consider the generalized Ising model where cluster-like

interaction [136, 137] is included in the Hamiltonian,

$$H_{GI} = \sum_{j=-M}^{M} a(\frac{1+\gamma}{2}\sigma_j^x\sigma_{j+1}^x + \frac{1-\gamma}{2}\sigma_j^y\sigma_{j+1}^y) + g\sigma_j^z + b\sigma_j^z(\frac{1+\delta}{2}\sigma_{j-1}^x\sigma_{j+1}^x + \frac{1-\delta}{2}\sigma_{j-1}^y\sigma_{j+1}^y), \tag{4.1}$$

with periodic boundary condition, i.e., $\sigma_{N+1}^{\alpha} = \sigma_1^{\alpha}$. $\sigma_j^{\alpha}(\alpha = x, y, z)$ are Pauli matrixes at site i. M is $N/2$ ($(N-1)/2$) for N even (odd). The NN and inter-spin mediated NNN interactions in XY plane are controlled by anisotropy parameters γ and δ, respectively. g is the external magnetic field along z axis. a and b denote the strength of interactions.

For the case of $b = 0$, it is the XY model. This model has been studied in equilibrium and nonequilibrium dynamics [55, 53, 62, 54]. When $a = -1, \gamma = 1$, it is Ising model. For $|g| < 1$, the system has two degenerate ferromagnetic ground states with spin polarized along $|\rightarrow\rangle$ or $|\leftarrow\rangle$. $|\rightarrow\rangle$ and $|\leftarrow\rangle$ are two eigenstates of σ_x. For $|g| > 1$, the system is in the paramagnetic phase where the spins are polarized by g. $|g| = 1$ is transition points between this two phases.

To investigate this model, one should simplify the Hamiltonian. As a standard procedure, one can use Jordan-Wigner transformation to map the spins to 1D spinless fermions with creation and annihilation operators $\hat{c}_j^{\dagger}, \hat{c}_j$,

$$\sigma_j^x = \prod_{l<j}(1 - 2\hat{c}_l^{\dagger}\hat{c}_l)(\hat{c}_j + \hat{c}_j^{\dagger}), \tag{4.2}$$

$$\sigma_j^y = -i\prod_{l<j}(1 - 2\hat{c}_l^{\dagger}\hat{c}_l)(\hat{c}_j - \hat{c}_j^{\dagger}), \tag{4.3}$$

$$\sigma_j^z = 1 - 2\hat{c}_j^{\dagger}\hat{c}_j, \tag{4.4}$$

with $\sigma_l^{\pm} = (\sigma_l^x \pm i\sigma_l^y)/2$. The operators $\hat{c}_j, \hat{c}_j^{\dagger}$ obey the canonical fermionic algebra,

$$\{\hat{c}_j, \hat{c}_{j'}^{\dagger}\} = \delta_{jj'}, \{\hat{c}_j, \hat{c}_{j'}\} = 0, \{\hat{c}_j^{\dagger}, \hat{c}_{j'}^{\dagger}\} = 0. \tag{4.5}$$

The coupled spins transform as

$$\begin{aligned} \sigma_j^x\sigma_{j+1}^x &= (\hat{c}_j^{\dagger} - \hat{c}_j)(\hat{c}_{j+1}^{\dagger} + \hat{c}_{j+1}), \\ \sigma_j^y\sigma_{j+1}^y &= (\hat{c}_j^{\dagger} + \hat{c}_j)(-\hat{c}_{j+1}^{\dagger} + \hat{c}_{j+1}). \end{aligned} \tag{4.6}$$

In the fermionic representation,

$$\begin{aligned} H_{GI} &= \sum_{j=-M}^{M} [a(\gamma \hat{c}_j^\dagger \hat{c}_{j+1}^\dagger + \hat{c}_j^\dagger \hat{c}_{j+1} + h.c.) + g(1 - 2\hat{c}_j^\dagger \hat{c}_j) \\ &+ b(\delta \hat{c}_{j-1}^\dagger \hat{c}_{j+1}^\dagger + \hat{c}_{j-1}^\dagger \hat{c}_{j+1} + h.c.)]. \end{aligned} \tag{4.7}$$

By Fourier transformation, $\hat{c}_k = \frac{1}{\sqrt{N}} \sum_j \hat{c}_j \exp(-ijk)$ with $k = -\pi, ..., \pi$, the Hamiltonian can be transformed to momentum space,

$$\begin{aligned} H_{GI} &= \sum_k i(a\gamma \sin k + b\delta \sin 2k)(\hat{c}_k^\dagger \hat{c}_{-k}^\dagger + \hat{c}_k \hat{c}_{-k}) \\ &+ (a \cos k + b \cos 2k - g)(\hat{c}_k^\dagger \hat{c}_k - \hat{c}_{-k} \hat{c}_{-k}^\dagger). \end{aligned} \tag{4.8}$$

We write the Hamiltonian in Nambu space $\Psi_k^\dagger = (\hat{c}_k^\dagger, \hat{c}_{-k})$ as $H_{GI} = \sum_k \Psi_k^\dagger H_{GI}(k) \Psi_k$. Using the Anderson pseudospin $\mathbf{d}(k)$, the Hamiltonian can be expressed as $H_{GI}(k) = \mathbf{d}(k) \cdot \boldsymbol{\sigma}$. $\mathbf{d}(k) = h_y \hat{\mathbf{e}}_y + h_z \hat{\mathbf{e}}_z$ where $\hat{\mathbf{e}}_y, \hat{\mathbf{e}}_z$ are the unit vectors in y, z directions. $h_y = -(a\gamma \sin k + b\delta \sin 2k)$, $h_z = a \cos k + b \cos 2k - g$.

After diagonalizing the Hamiltonian, we obtain

$$H_{GI} = \sum_k 2\Lambda_k (\hat{\eta}_k^\dagger \hat{\eta}_k - \frac{1}{2}), \tag{4.9}$$

with

$$\Lambda_k = [(a \cos k + b \cos 2k - g)^2 + (a\gamma \sin k + b\delta \sin 2k)^2]^{1/2}, \tag{4.10}$$

and $\hat{\eta}_k = \hat{c}_k \cos \frac{\theta_k}{2} + ie^{-i2\phi} \hat{c}_{-k}^\dagger \sin \frac{\theta_k}{2}$. θ_k is defined as

$$\theta_k = \arctan \frac{(a\gamma \sin k + b\delta \sin 2k)}{(a \cos k + b \cos 2k - g))}. \tag{4.11}$$

The topological structures in the parameter space $(h_y(k), h_z(k))$ are shown in Fig.4.1. The topology can be changed as parameters of the Hamiltonian vary and phase transitions occur. To characterize the phase transition, one can define the winding number of θ_k as

$$W = \frac{1}{2\pi} \int_{\text{B.Z.}} d\theta_k. \tag{4.12}$$

Then the phase transition can be [47].

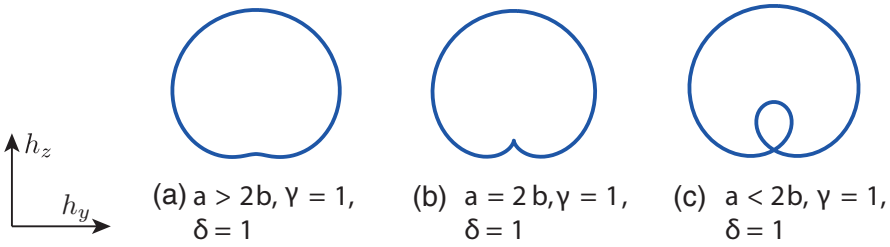

Figure 4.1: The variation of topology of the parameter space when the system changes.

4.2 Geometric Phase Generated by Spin Rotations

When $\gamma = 0$, the Hamiltonian Eq. (4.1) has an additional $U(1)$ symmetry involving spin rotation in the xy plane, which is broken with finite γ. Those systems with the broken symmetry constitute a continuous space with the identical spectrum. They are related by a unitary rotation of all the spins around the z-axis by angle [55]. By applying such rotation, nontrivial complex instantaneous eigenstates can be created and geometric property of the system can be studied in these states [55, 53, 62]. The rotating spin chain is described by

$$\begin{aligned} H_\phi^{GI} &= \mathcal{R}^\dagger H_{GI} \mathcal{R} \\ &= \sum_{j=-M}^{M} a \left(\frac{1+\gamma}{2} \mathcal{R}^\dagger \sigma_j^x \sigma_{j+1}^x \mathcal{R} + \frac{1-\gamma}{2} \mathcal{R}^\dagger \sigma_j^y \sigma_{j+1}^y \mathcal{R} \right) + g \mathcal{R}^\dagger \sigma_j^z \mathcal{R} \\ &\quad + b \left(\frac{1+\delta}{2} \mathcal{R}^\dagger \sigma_{j-1}^x \sigma_j^z \sigma_{j+1}^x \mathcal{R} + \frac{1-\delta}{2} \mathcal{R}^\dagger \sigma_{j-1}^y \sigma_j^z \sigma_{j+1}^y \mathcal{R} \right), \end{aligned} \tag{4.13}$$

with $\mathcal{R} = \prod_{j=-M}^{M} e^{-i\phi_j \sigma_j^z/2}$. The rotations of the coupled spins are

$$\begin{aligned} \mathcal{R}^\dagger \sigma_j^x \sigma_{j+1}^x \mathcal{R} &= \cos\phi_j \cos\phi_{j+1} \sigma_j^x \sigma_{j+1}^x - \cos\phi_j \sin\phi_{j+1} \sigma_j^x \sigma_{j+1}^y \\ &\quad - \sin\phi_j \cos\phi_{j+1} \sigma_j^y \sigma_{j+1}^x + \sin\phi_j \sin\phi_{j+1} \sigma_j^y \sigma_{j+1}^y, \end{aligned} \tag{4.14}$$

$$\begin{aligned} \mathcal{R}^\dagger \sigma_j^y \sigma_{j+1}^y \mathcal{R} &= \cos\phi_j \cos\phi_{j+1} \sigma_j^y \sigma_{j+1}^y + \cos\phi_j \sin\phi_{j+1} \sigma_j^y \sigma_{j+1}^x \\ &\quad + \sin\phi_j \cos\phi_{j+1} \sigma_j^x \sigma_{j+1}^y + \sin\phi_j \sin\phi_{j+1} \sigma_j^x \sigma_{j+1}^x, \end{aligned} \tag{4.15}$$

$$\mathcal{R}^\dagger\sigma^x_{j-1}\sigma^z_j\sigma^x_{j+1}\mathcal{R} = \cos\phi_{j-1}\cos\phi_{j+1}\sigma^x_{j-1}\sigma^z_j\sigma^x_{j+1} - \cos\phi_{j-1}\sin\phi_{j+1}\sigma^x_{j-1}\sigma^z_j\sigma^y_{j+1} - \sin\phi_{j-1}\cos\phi_{j+1}\sigma^y_{j-1}\sigma^z_j\sigma^x_{j+1} + \sin\phi_{j-1}\sin\phi_{j+1}\sigma^y_{j-1}\sigma^z_j\sigma^y_{j+1}, \quad (4.16)$$

$$\mathcal{R}^\dagger\sigma^y_{j-1}\sigma^z_j\sigma^y_{j+1}\mathcal{R} = \cos\phi_{j-1}\cos\phi_{j+1}\sigma^y_{j-1}\sigma^z_j\sigma^y_{j+1} + \cos\phi_{j-1}\sin\phi_{j+1}\sigma^y_{j-1}\sigma^z_j\sigma^x_{j+1} + \sin\phi_{j-1}\cos\phi_{j+1}\sigma^x_{j-1}\sigma^z_j\sigma^y_{j+1} + \sin\phi_{j-1}\sin\phi_{j+1}\sigma^x_{j-1}\sigma^z_j\sigma^x_{j+1}, \quad (4.17)$$

and $\mathcal{R}^\dagger\sigma^z_j\mathcal{R} = \sigma^z_j$. Then the rotated Hamiltonian is

$$\begin{aligned} H^{GI}_\phi = & -\frac{a}{2}\sum_j[(\cos(\phi_j-\phi_{j+1}) + \gamma\cos(\phi_j+\phi_{j+1}))\,\sigma^x_j\sigma^x_{j+1} \\ & + (\cos(\phi_j-\phi_{j+1}) - \gamma\cos(\phi_j+\phi_{j+1}))\,\sigma^y_j\sigma^y_{j+1} \\ & + (\sin(\phi_j-\phi_{j+1}) - \gamma\sin(\phi_j+\phi_{j+1}))\,\sigma^x_j\sigma^y_{j+1} \\ & - (\sin(\phi_j-\phi_{j+1}) + \gamma\sin(\phi_j+\phi_{j+1}))\,\sigma^y_j\sigma^x_{j+1}] \\ & -\frac{b}{2}\sum_j[(\cos(\phi_{j-1}-\phi_{j+1}) + \gamma\cos(\phi_{j-1}+\phi_{j+1}))\,\sigma^x_{j-1}\sigma^z_j\sigma^x_{j+1} \\ & + (\cos(\phi_{j-1}-\phi_{j+1}) - \gamma\cos(\phi_{j-1}+\phi_{j+1}))\,\sigma^y_{j-1}\sigma^z_j\sigma^y_{j+1} \\ & + (\sin(\phi_{j-1}-\phi_{j+1}) - \gamma\sin(\phi_{j-1}+\phi_{j+1}))\,\sigma^x_{j-1}\sigma^z_j\sigma^y_{j+1} \\ & - (\sin(\phi_{j-1}-\phi_{j+1}) + \gamma\sin(\phi_{j-1}+\phi_{j+1}))\,\sigma^y_{j-1}\sigma^z_j\sigma^x_{j+1}] \\ & + g\sum_j\sigma^z_j. \end{aligned} \quad (4.18)$$

We assume that the spin rotating angle $\phi_j = \phi$ for every spin. Based on the transformations Eq. (4.6) and

$$\begin{aligned} \sigma^x_j\sigma^y_{j+1} &= -i(\hat{c}^\dagger_j - \hat{c}_j)(-\hat{c}^\dagger_{j+1} + \hat{c}_{j+1}), \\ \sigma^y_j\sigma^x_{j+1} &= i(\hat{c}^\dagger_j + \hat{c}_j)(\hat{c}^\dagger_{j+1} + \hat{c}_{j+1}), \\ \sigma^x_{j-1}\sigma^z_j\sigma^x_{j+1} &= (\hat{c}^\dagger_{j-1} - \hat{c}_{j-1})(\hat{c}^\dagger_{j+1} + \hat{c}_{j+1}), \\ \sigma^x_{j-1}\sigma^z_j\sigma^y_{j+1} &= -i(\hat{c}^\dagger_{j-1} - \hat{c}_{j-1})(\hat{c}^\dagger_{j+1} - \hat{c}_{j+1}), \\ \sigma^y_{j-1}\sigma^z_j\sigma^x_{j+1} &= -i(\hat{c}^\dagger_{j-1} + \hat{c}_{j-1})(\hat{c}^\dagger_{j+1} + \hat{c}_{j+1}), \\ \sigma^y_{j-1}\sigma^z_j\sigma^y_{j+1} &= -(\hat{c}^\dagger_{j-1} + \hat{c}_{j-1})(\hat{c}^\dagger_{j+1} - \hat{c}_{j+1}), \end{aligned} \quad (4.19)$$

we have

$$H_\phi^{GI} = \sum_{j=-M}^{M} [a(\gamma e^{-i2\phi}\hat{c}_j^\dagger \hat{c}_{j+1}^\dagger + \hat{c}_j^\dagger \hat{c}_{j+1} + h.c.) + g(1 - 2\hat{c}_j^\dagger \hat{c}_j) + b(\delta e^{-i2\phi}\hat{c}_{j-1}^\dagger \hat{c}_{j+1}^\dagger + \hat{c}_{j-1}^\dagger \hat{c}_{j+1} + h.c.)]. \quad (4.20)$$

Using the Fourier transformation, H_ϕ^{GI} is transformed to momentum space as

$$H_\phi^{GI} = \sum_k i(a\gamma \sin k + b\delta \sin 2k(e^{-i2\phi}\hat{c}_k^\dagger \hat{c}_{-k}^\dagger + e^{i2\phi}\hat{c}_k \hat{c}_{-k}) + (a\cos k + b\cos 2k - g)(\hat{c}_k^\dagger \hat{c}_k - \hat{c}_{-k}\hat{c}_{-k}^\dagger), \quad (4.21)$$

The eigenspectrum is as the same as Eq. (4.9). The ground state of H_ϕ^{GI} is

$$|\chi(\phi)\rangle = \prod_k (\cos\frac{\theta_k}{2}|0\rangle_k|0\rangle_{-k} - ie^{-i2\phi}\sin\frac{\theta_k}{2}|1\rangle_k|1\rangle_{-k}). \quad (4.22)$$

The ground state $|\chi\rangle$ is a tensor product of states, each lying in the two-dimensional Hilbert space spanned by $|0\rangle_k|0\rangle_{-k}$ and $|1\rangle_k|1\rangle_{-k}$. The geometric phase

$$\varphi = \frac{i}{M}\int_0^\pi \langle\chi(\phi)|\partial_\phi|\chi(\phi)\rangle d\phi = \frac{\pi}{M}\sum_{k=0}^{\pi}(1 - \cos\theta_k). \quad (4.23)$$

We assume that g is the control parameter. Thus, the phase of the system can be tuned by g. We can find three critical points for g: $-a+b, a+b, \frac{a^2\gamma^2 - a^2\gamma\delta - 2b^2\delta^2}{2b\delta^2}$ for this generalized Ising model. This phase diagram has been analysed in [134]. There, only one cluster term, i.e., $\sum_j \sigma_{j-1}^x \sigma_j^z \sigma_{j+1}^x$ is considered. The full phase diagram should be interesting when the other cluster-like terms, e.g., $\sum_j \sigma_{j-1}^y \sigma_j^z \sigma_{j+1}^y$, are considered.

In this section, we give some examples that illustrate the geometric phases and winding numbers. At first, we look at the simplest case, i.e., Ising model with $b = 0, \delta = 0, a = 1, \gamma = 1$ in Eq. (4.1). In Fig. 4.2 (a) and (b) we show the geometric phase and DGP. We can see that there are critical points at $|g| = 1$. This critical behavior of geometric phase has been discussed for Ising model [62]. In (b), topology in parameter space $(h_y(\boldsymbol{k}), h_z(\boldsymbol{k}))$ are demonstrated for various phases. When g goes across -1, the topology goes from above horizontal axis to the one containing the original point. As g changes continuously, there is a transition at $g = 1$ where the original point leaves the topology. The winding

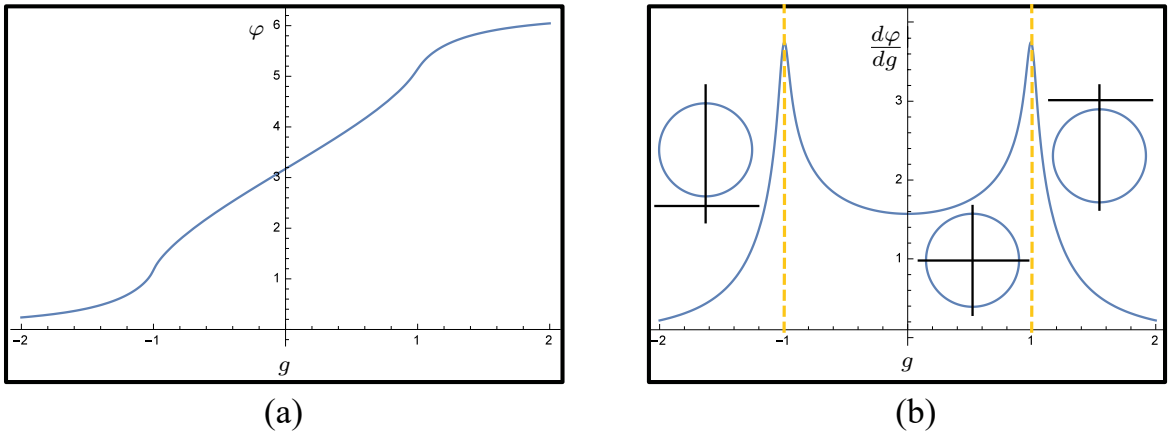

Figure 4.2: Geometric phase (a) and DGP (b) with the parameters $b = 0, \delta = 0, a = 1, \gamma = 1$.

number changes as $0, 1, 0$ when g varies from -2 to 2.

With the cluster-like interactions, the phase structure becomes complex and interesting. For the generalized Ising model, one can have different topologies in the momentum space. In Fig. 4.3, we show the case with $b = 1, \delta = 1, a = 1, \gamma = 1$. We can see that there are four phases. When $g < -1$, the topology is above horizontal axis. As $-1 < g < 0$, the original point is in the center of two circles. When $0 < g < 1$, only the out circle contains the original point. Finally, if $g > 1$, the original point goes out of the topology. We can find the derivative of geometric phase shows the critical points. Actually, these different phases correspond to different winding numbers which are $0, 2, 1, 0$, respectively.

By manipulating the parameter δ, one can have more topological features. In Fig. 4.4, we show the plots for $b = 1, \delta = -0.7, a = 1, \gamma = 1$. This choice of these parameters gives an interesting structure as shown in Fig. 4.4(b). As g changes from negative to positive values, the system goes through phases with the corresponding winding numbers $0, 1, -1, 0$. When we change δ to -1.5, we get a different topology as shown in Fig. 4.5(b), where the winding number changes successively as $0, -2, -1, 0$.

In these examples, the DGP shows the phase boundaries whenever the winding number changes. There are two kinds of ways that winding number varies across the critical regime. One is that the winding number difference is unity near the critical points. This kind of critical regime has been investigated [62]. Another one case is where the winding number difference is larger than 1. The latter case is quite interesting. To characterize such phase transitions with large winding number difference, we use the finite-size scaling

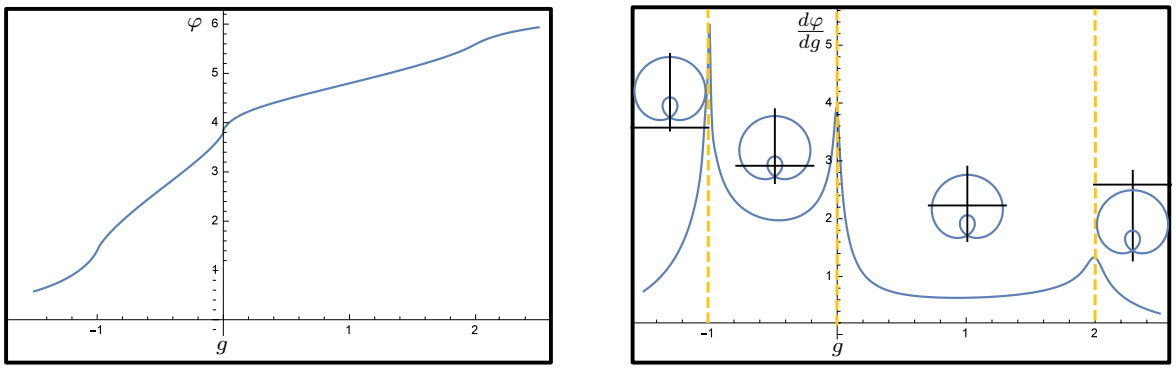

(a) (b)

Figure 4.3: Geometric phase (a) and DGP (b) with the parameters $b = 1, \delta = 1, a = 1, \gamma = 1$.

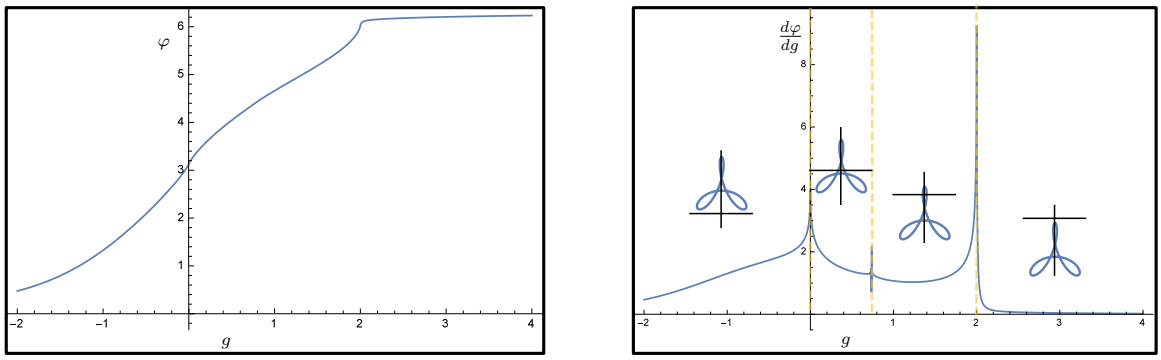

(a) (b)

Figure 4.4: Geometric phase (a) and DGP (b) with the parameters $b = 1, \delta = -0.7, a = 1, \gamma = 1$.

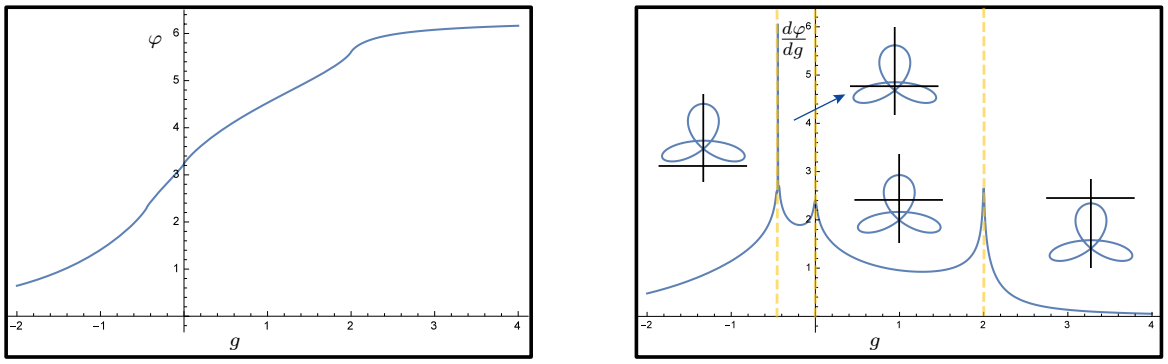

(a) (b)

Figure 4.5: Geometric phase (a) and DGP (b) with the parameters $b = 1, \delta = -1.5, a = 1, \gamma = 1$.

of geometric phase to study the critical phenomena.

4.3 Floquet Driving Induced Multispin Interaction

The generalized Ising model Eq. (4.1) can be rewritten as

$$\begin{aligned} H_{\text{GIF}} = & \sum_{i=-M}^{M} \frac{a}{2}(\sigma_j^x \sigma_{j+1}^x + \sigma_j^y \sigma_{j+1}^y) + \frac{b}{2}\sigma_i^z(\sigma_{i-1}^x \sigma_{i+1}^x + \sigma_{i-1}^y \sigma_{i+1}^y) \\ & + \frac{c}{2}(\sigma_j^x \sigma_{j+1}^x - \sigma_j^y \sigma_{j+1}^y) + \frac{d}{2}\sigma_i^z(\sigma_{i-1}^x \sigma_{i+1}^x - \sigma_{i-1}^y \sigma_{i+1}^y) + g\sigma_j^z. \end{aligned} \tag{4.24}$$

In the fermionic representation,

$$\begin{aligned} H_{\text{GIF}} = & \sum_{j=1}^{N}[(c\hat{c}_j^\dagger \hat{c}_{j+1}^\dagger + a\hat{c}_j^\dagger c_{j+1} + h.c.) + (d\hat{c}_{j-1}^\dagger \hat{c}_{j+1}^\dagger + b\hat{c}_{j-1}^\dagger \hat{c}_{j+1} + h.c.)] \\ & + g(1 - 2\hat{c}_j^\dagger \hat{c}_j). \end{aligned} \tag{4.25}$$

For a system with periodic driving, $H(t+T) = H(t)$ where $T = 2\pi/\omega$ is the period of the driving, the Floquet theory can be applied. After using the Floquet state $|\psi_\nu(t)\rangle = e^{-i\epsilon_\nu t}|\phi_\nu(t)\rangle$, one can have the Floquet equation,

$$H_F(t)|\phi_\nu(t)\rangle = \epsilon_\nu|\phi_\nu(t)\rangle. \tag{4.26}$$

where $H_F(t) = H(t) - i\partial_t$ is the Floquet Hamiltonian. The Floquet modes are time-periodic $|\phi_\nu(t+T)\rangle = |\phi_\nu(t)\rangle$. ν labels the band index. The quasienergies ϵ_ν and Floquet states $|\psi_\nu(t)\rangle$ are only uniquely defined up to the gauge freedom $\epsilon' = \epsilon_\nu + n\omega$, $|\phi'\rangle = |\phi_{\nu+n}\rangle$. We fix the gauge by choosing within the first Floquet-Brillouin zone $-\omega/2 \leq \epsilon_\nu \leq \omega/2$.

And the Hamiltonian can be written as

$$H(t) = H_0 + \delta H(t). \tag{4.27}$$

To find the effective Hamiltonian of the system, we make a rotating frame transformation. The unitary operator can be defined as $U^\dagger(t) = e^{i\int_0^t dt' \delta H(t')}$. And the Hamiltonian in the new frame is

$$\tilde{H}(t) = U^\dagger(t)H(t)U(t) - iU^\dagger(t)\dot{U}(t). \tag{4.28}$$

and $|\tilde{\phi}_\nu(t)\rangle = U^\dagger(t)|\phi_\nu(t)\rangle$.

At first we consider to drive the term $(\sigma_j^x\sigma_{j+1}^x + \sigma_j^y\sigma_{j+1}^y)$ with $a = a_0 + \frac{a_1}{2}\cos\omega t$, following the procedure [138], the effective Hamiltonian is

$$\begin{aligned}
\tilde{H}^{\text{eff}}_{\text{GIF1}} = \quad & \sum_{j=1}^{N} \frac{a_0}{2}(\sigma_j^x\sigma_{j+1}^x + \sigma_j^y\sigma_{j+1}^y) \\
& + \frac{b}{2}(\sigma_j^x\sigma_{j+1}^z\sigma_{j+2}^x + \sigma_j^y\sigma_{j+1}^z\sigma_{j+2}^y) + g\sigma_j^z \\
& + p_0(\sigma_j^x\sigma_j^x - \sigma_j^y\sigma_j^y) \\
& + \sum_{l=1,3,\ldots} p_l^o(a_1)(\sigma_j^x M_{j,l}^z\sigma_{j+l}^x - \sigma_j^y M_{j,l}^z\sigma_{j+l}^y) \\
& + \sum_{l=2,4,\ldots} p_l^e(a_1)(\sigma_j^x M_{j,l}^z\sigma_{j+l}^x - \sigma_j^y M_{j,l}^z\sigma_{j+l}^y),
\end{aligned} \tag{4.29}$$

with $M_{j,l}^z = \sigma_{j+1}^z \ldots \sigma_{j+l-1}^z$. Other parameters are

$$\begin{aligned}
p_0 &= \frac{d}{2}\sum_{m=0}^{\infty} D_{m,m+1}, \\
p_l^o &= \frac{c}{2}\sum_{m=0}^{\infty}(D_{m,m+\frac{l+1}{2}} - D_{m,m-\frac{l-1}{2}}), \\
p_l^e &= \frac{d}{2}\sum_{m=0}^{\infty}(D_{m,m+\frac{l+2}{2}} - D_{m,m-\frac{l-2}{2}}),
\end{aligned} \tag{4.30}$$

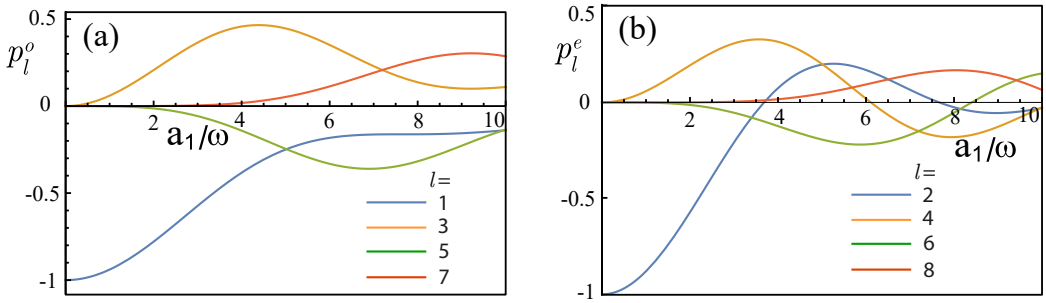

Figure 4.6: Multispin interactions for (a) odd and (b) even l as a function of a_1/ω.

where $D_{m,r} = \frac{(-1)^m}{(m!)^2}(\frac{a_1}{4\omega})^{2m}\begin{pmatrix}2m\\r\end{pmatrix}$. In Eq. (4.29), the multispin interactions characterized by $p_l^o(a_1)$ and $p_l^e(a_1)$ are created. In Fig. 4.6 we show the p_l^o and p_l^e as a function of a_1/ω. As the Floquet driving is weak, i.e., $a_1/\omega \ll 1$, only the terms $(\sigma_j^x\sigma_{j+1}^x - \sigma_j^y\sigma_{j+1}^y)$ and $\sigma_i^z(\sigma_{i-1}^x\sigma_{i+1}^x - \sigma_{i-1}^y\sigma_{i+1}^y)$ are kept. As it becomes large, multispin interactions take place.

If we drive $c = c_0 + \frac{c_1}{2}\cos\omega t$, we can get the effective Hamiltonian as

$$\begin{aligned}\tilde{H}^{\text{eff}}_{\text{GIF2}} = \quad & \sum_{j=1}^{N}\frac{c_0}{2}(\sigma_j^x\sigma_{j+1}^x - \sigma_j^y\sigma_{j+1}^y) + \frac{d}{2}(\sigma_j^x\sigma_{j+1}^z\sigma_{j+2}^x - \sigma_j^y\sigma_{j+1}^z\sigma_{j+2}^y) - h_0\sigma_j^z \\ & + \sum_{l=1,3,\ldots} h_l^o(c_1)(\sigma_j^x M_{j,l}^z\sigma_{j+l}^x + \sigma_j^y M_{j,l}^z\sigma_{j+l}^y) \\ & + \sum_{l=2,4,\ldots} h_l^e(c_1)(\sigma_j^x M_{j,l}^z\sigma_{j+l}^x + \sigma_j^y M_{j,l}^z\sigma_{j+l}^y),\end{aligned} \tag{4.31}$$

with

$$\begin{aligned} h_0 &= \sum_{m=0}^{\infty} bC_{m,m-1} - gC_{m,m}, \\ h_l^o &= \sum_{m=0}^{\infty}\frac{a}{2}(C_{m,m-\frac{l-1}{2}} + C_{m,m-\frac{l+1}{2}}), \\ h_l^e &= \sum_{m=0}^{\infty}\frac{b}{2}(C_{m,m-\frac{l-2}{2}} + C_{m,m-\frac{l+2}{2}}) - gC_{m,m-\frac{l}{2}}, \end{aligned} \tag{4.32}$$

where $C_{m,r} = \frac{(-1)^{2m-r}}{(m!)^2}(\frac{c_1}{4\omega})^{2m}\begin{pmatrix}2m\\r\end{pmatrix}$. The difference between Eq. (4.29) and Eq. (4.31) is the effective multispin interactions.

4.4 Finite-size Scaling of Geometric Phase

Universality is essential for quantum phase transition. Near critical regime, correlation length becomes diverging and microscopic details are lost. To investigate the universal properties, many approaches are proposed to be able to characterize phase transition by finite-size scaling, e.g., entanglement [139, 140, 141], geometric phase [62], geometric tensor [142], Schmidt gap [143]. Zhu [62] suggested a finite-size scaling analysis of geometric phase to study phase transition in XY spin chain. The scaling behavior obeys universal characteristics of phase boundary in Ising university class. However, previous studies limit the models where phase transition occurs at critical momentum k_c independent of the system parameters. Recent study by Lahtinen and Ardonne discussed criticalities at symmetry protected critical points in generalized cluster model where all $so(N)_1$ critical points can be found [144]. At some symmetry protected points, the system has degeneracies at the critical momentum away from 0 or π. We are interested in the phase transitions and finite-size scaling behavior at these critical points.

4.4.1 Phase Diagram of Cluster-Ising Model

In the first section, we have discussed the generalized Ising model Eq. (4.1). In this section, we consider a model with multispin interactions, i.e., so-called cluster-Ising model

$$H_{CI} = -\sum_{j=1}^{N} \lambda \sigma_j^x M_{j,l}^z \sigma_{j+l}^x + a \sum_{j=1}^{N} \sigma_j^y \sigma_{j+1}^y + g \sum_{j=1}^{N} \sigma_j^z, \tag{4.33}$$

The periodic boundary conditions are assumed. When $l = 2$, $M_{j,l}^z$ is the cluster operator C_j. After Jordan-Wigner transformation and Fourier transformation, we can write the Hamiltonian $H_{CI} = \sum_k \Psi_k^\dagger H_{CI}(k) \Psi_k$, where $H_{CI}(k) = \tilde{\mathbf{d}}(k) \cdot \boldsymbol{\sigma}$. $\tilde{\mathbf{d}}(k) = \tilde{h}_y \hat{\mathbf{e}}_y + \tilde{h}_z \hat{\mathbf{e}}_z$ with $\tilde{h}_y = \lambda \sin kl + a \sin k$, $\tilde{h}_z = a \cos k - \lambda \cos kl - g$. The winding number can be calculated via $\tilde{\theta}_k = \arctan \frac{\lambda \sin kl + a \sin k}{a \cos k - \lambda \cos kl - g}$.

Table 4.1: Phase and winding number for interactions.

Interaction	Phase	Winding number
$\pm \sum_j \sigma_j^z$	P	0
$\pm \sum_j \sigma_j^y \sigma_{j+1}^y$	$\mathrm{AFM}^{(\mathrm{Y})}, \mathrm{FM}^{(\mathrm{Y})}$	+1
$\pm \sum_j \sigma_j^x \sigma_{j+1}^x$	$\mathrm{AFM}^{(\mathrm{X})}, \mathrm{FM}^{(\mathrm{X})}$	−1
$\pm \sum_j \sigma_j^x \mathcal{Z}_{j,l} \sigma_{j+l}^x$	C_l^*, C_l	$-l$

For $l = 1$, $M^z_{j,l} = 1$, and therefore the Hamiltonian defines the transverse Ising model with the well known antiferromagnet-paramagnet quantum phase transition in the Ising universality class. For $l = 2$, Eq. (4.33) defines the so-called cluster-Ising model in an external magnetic field. Assuming periodic boundary conditions: $\sigma^\alpha_{N+1} = \sigma^\alpha_1$, the ground state of Eq. (4.33) for $a = g = 0$ is a unique state known as cluster state [145]. Such state enjoys a non trivial global symmetry of the $\mathbb{Z}_2 \times \mathbb{Z}_2$ type. For open boundary conditions, the cluster state is fourfold degenerate. Such a degeneracy can be lifted only by resorting to operators in the Hamiltonians's symmetry algebra. In such a specific sense, the cluster ground state provides an example of quantum phase of matter with the so-called symmetry protected topological order. Remarkably, such a kind of order is preserved by the Ising interaction and the external field in Eq. (4.33) until quantum phase transitions occur into the system.

The winding numbers for the terms in the Hamiltonian are shown in Table 4.1. The winding number for the first term in Eq. (4.33) is $-l$. When $l = 2$, the ground states of the first part of the Hamiltonian is cluster states or dual cluster states depending on the value of λ. The winding numbers for $\mathrm{AFM}^{(\mathrm{Y})}$ and $\mathrm{FM}^{(\mathrm{Y})}$ are both 1. This means that we can not use the winding number to fully characterize all the phases. However, we know that if two phases can be adiabatically connected without going through degeneracy, they are the same phase. With this property, we can distinguish different phases even they have the same winding number. The high winding number from the first term makes the system nontrivial.

The cluster-Ising models enjoy non-trivial duality properties. In particular, our Hamiltonian Eq. (4.33) can be mapped to the class of models considered in Ref. [63]. The Hamiltonian for $l = 3$ is

$$H_{GC3} = -\sum_{j=1}^{N} \lambda \sigma^x_j \sigma^z_{j+1} \sigma^z_{j+2} \sigma^x_{j+3} + a \sum_{j=1}^{N} \sigma^y_j \sigma^y_{j+1} + g \sum_{j=1}^{N} \sigma^z_j. \tag{4.34}$$

One can make a dual transformation

$$\begin{aligned} \sigma^z_j &= \tau^y_j \tau^y_{j+1}, \\ \sigma^x_j \sigma^x_{j+1} &= \tau^z_{j+1}, \\ \sigma^y_j \sigma^y_{j+1} &= -\tau^y_j \tau^z_{j+1} \tau^y_{j+2}, \\ \sigma^x_{j-1} \sigma^z_j \sigma^z_{j+1} \sigma^x_{j+2} &= -\tau^x_j \tau^z_{j+1} \tau^x_{j+2}. \end{aligned} \tag{4.35}$$

We can have

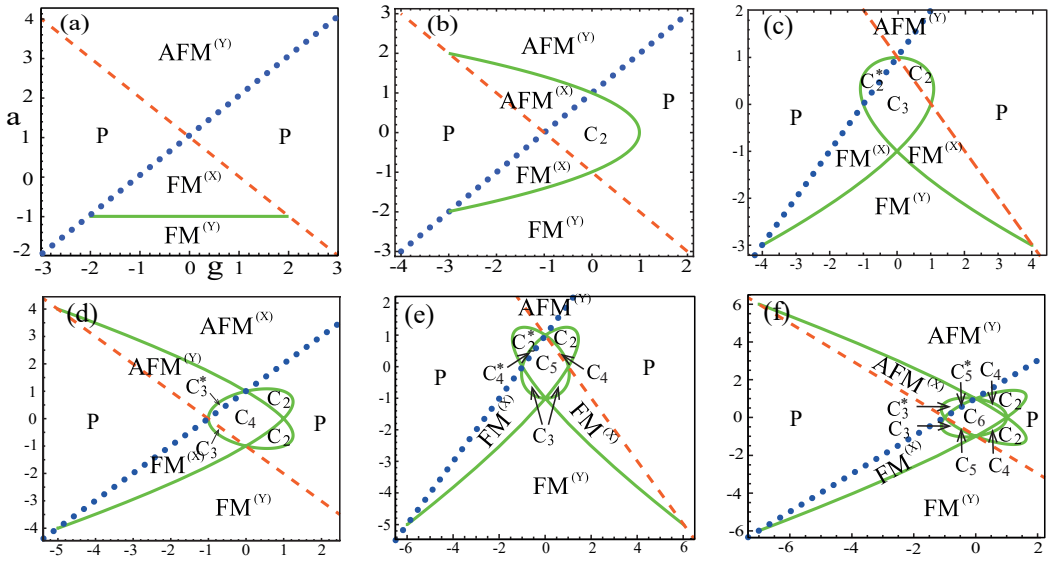

Figure 4.7: Phase diagram of cluster-Ising models. (a)-(f) are phase diagrams of the system for l from 1 to 6. We choose $\lambda = 1$.

$$H_{CI3}^{dual} = \lambda \sum_j \tau_j^x \tau_{j+1}^z \tau_{j+2}^x - a \sum_j \tau_j^y \tau_{j+1}^z \tau_{j+2}^y + g \sum_j \tau_j^y \tau_{j+1}^y. \tag{4.36}$$

Since the construction of the phase diagram of the systems relies on energy properties, the phase diagrams are unaltered by duality.

Phase diagrams with l from 1 to 6 are shown in Fig. 4.7((a)-(f)). Fig. 4.7(a) and (b) show the detailed phase diagram for $l = 1$ and $l = 2$ (see Ref. [63, 47]). The abbreviations mean different phases: paramagnetic (P), ferromagnetic (FM), antiferromagnetic (AFM), cluster (C). The superscript specifies the direction of the order. The cases $l > 2$ were recently studied by Lahtinen and Ardonne [144]. For even l ((b),(d),(f)), the Zeeman field is the control parameter. When $g > 0$, phases with even integer winding numbers are generated. The Ising interaction a tunes the ferromagnetic or antiferromagnetic phases. The roles of g and a are exchanged for odd l ((a),(c),(e)). Elaborating on the findings for $l = 2$ [132], Lahtinen and Ardonne demonstrated that the criticality of the system is indeed characterized by the $so(l+1)_1$ conformal field theory. The structure of the phase diagrams is related to the symmetry of $(h_y(k), h_z(k))$. Such symmetry implies that for l even, the phase diagram is symmetric $a \to -a$; for odd l, the symmetry is $g \to -g$. FM^α or AFM^α denotes ferromagnetic or antiferromagnetic order along the spin direction α, respectively. The C_2 and C_2^* cluster and dual cluster phases respectively, display a string order of the cluster state type with two Majorana modes at the edges of the system; such

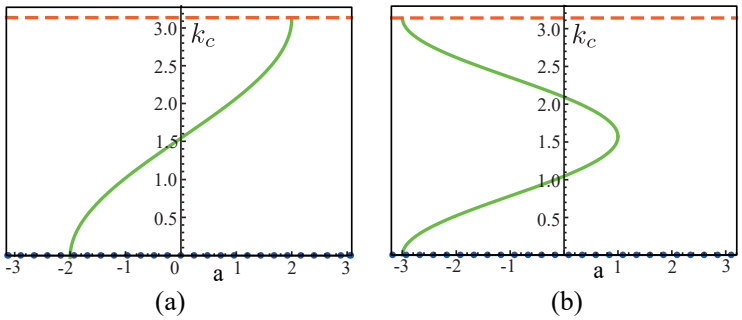

Figure 4.8: Critical momentums for (a) $l = 2$ and (b) $l = 3$.

two phases are characterized by string order parameters with different spin polarizations at the edges [63]. Similarly, C_3 phases are cluster state phases with three Majorana modes at the edges of the system. C_3 and C_3^* phases in (c) are distinguished from each other by the negative and positive Ising interaction a. The C_m and C_m^* phases with $m > 2$ in Fig. 4.7 ((c)-(f)) are defined in with a similar logic. For even l, C_m^* and C_m cluster phases can be swapped by inversion of the Zeeman field g; for odd l, they can be transformed one another by swapping ferromagnetic and antiferromagnetic Ising exchange. The different phases C_m with fixed l in the different panels of Fig. 4.7 can be connected adiabatically. Namely a fixed phase C_m of a given Hamiltonian H_l evolves in to C_m of H_{l+1} under $H_{l,l+1} = (t-1)\,H_l + tH_{l+1}$, $t \in [0,1]$.

The winding numbers for the phases P, C_2, $FM^{(Y)}$, $AFM^{(Y)}$, $FM^{(X)}$, $AFM^{(X)}$ are $0, -2, 1, 1, -1, -1$, respectively. The generalized cluster states with winding number $-l$ are "broken" into phases characterized by lower winding numbers $(-(l-1), \ldots), -1$. There is a parity property for l in the phase diagrams. Odd and even ls have different structures of phase diagrams. This would suggest that the generalized cluster states for odd and even ls have quite different properties.

The green-solid lines in Fig. 4.7 are in the XY universality class. For the blue-dotted (red-dashed) straight lines indicate Ising phase transitions. The XY and Ising transitions have a topological difference. The two phases separated by the XY line have winding number difference equals to 2. However, for ground states separated by the Ising type transition, the winding number difference is 1. Different from blue-dotted (red-dashed) lines, the green-solid lines have critical momentum depending on the parameters a and g. In Figs. 4.8(a) and (b), the critical momentums are presented for $l = 2$ and $l = 3$, respectively.

In Fig. 4.9(a) the critical points are labeled and the energy bands are shown in (b). For

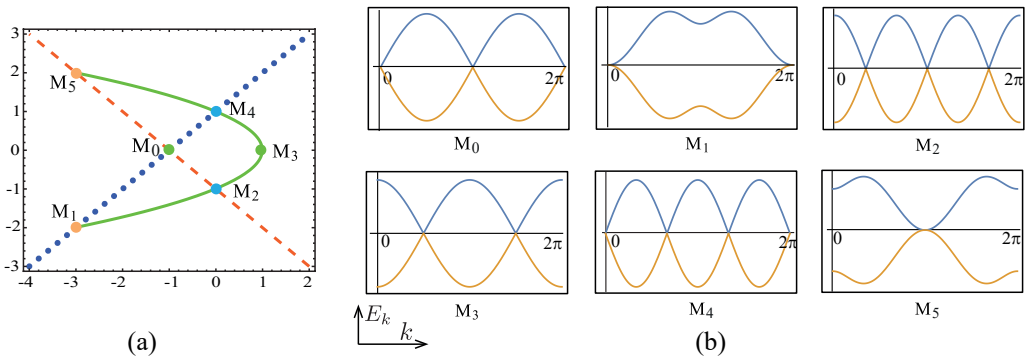

Figure 4.9: Phase diagram (a) for $l = 2$ and (b) energy band structures of some critical points.

the critical points at $a = 0$ or $g = 0$, low-energy dispersions are linear (M_0, M_2, M_3, M_4). However, for M_1 and M_5, the low-energy dispersions are quadratic. Actually the difference between the dispersions can lead to novel effects. Recent studies reveal a new kind of Weyl semimetal with quadratic double Weyl fermions arising from the spin-orbit coupling [146]. They show that the linear and quadratic dispersions have different chiral topological charges. Recent developments of topological materials in condensed matter physics show that energy band is a resource to analyse physical properties of the periodic system. Therefore, we want to study the difference between the linear and quadratic dispersions with finite-size scaling.

4.4.2 Scaling Behavior of Linear Dispersions

Now we discuss the scaling behavior of phase boundaries close to quantum phase transitions with $z = 1$ (green-solid lines in Fig. 4.7). We present the scaling behavior in Fig. 4.10. The scaling ansatz for the (derivative of the) geometric phase is

$$\frac{d\varphi}{dg}|_{g_m} \simeq \kappa_1 \ln N + \text{const}, \tag{4.37}$$

$$\frac{d\varphi}{dg} \simeq \kappa_2 \ln |g - g_c| + \text{const}, \tag{4.38}$$

where g_c is the critical value for infinite long spin chain, and g_m marks the anomaly for the finite size system. According to the scaling ansatz, in the case of logarithmic singularities, the ratio $|\kappa_2/\kappa_1|$ is the exponent ν that governs the divergence of correlation length. We

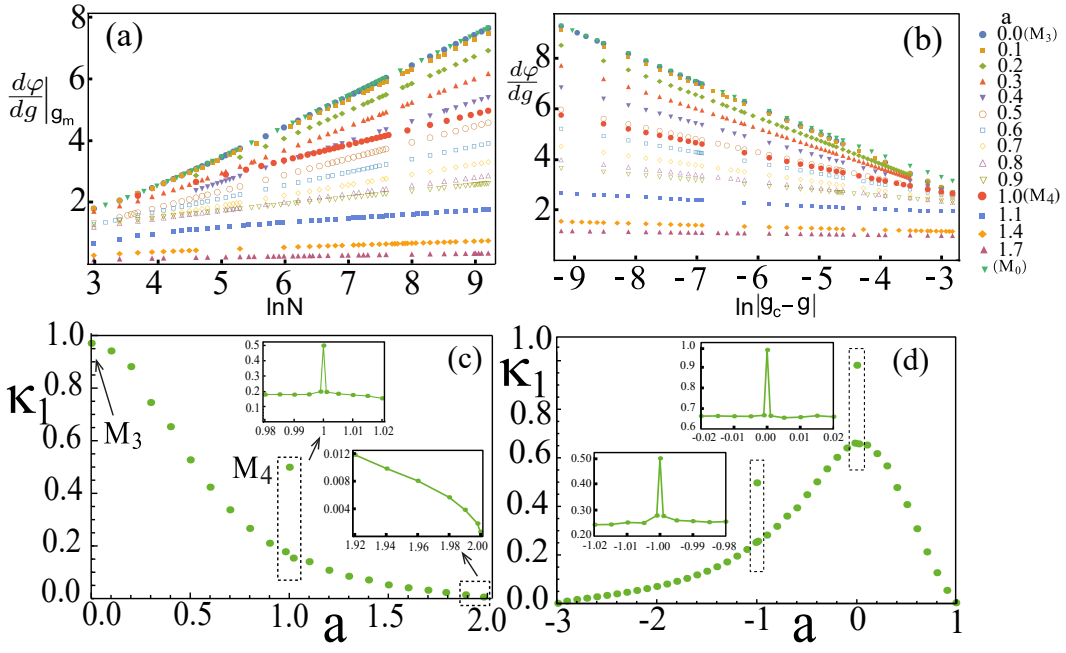

Figure 4.10: Scaling behaviors for the transition line from M_3 to M_5 according to (a) Eq. (4.37) and (b) Eq. (4.38). (c) Scaling coefficient κ_1 for the green phase boundary in Fig. 4.7(b) with critical momentum k_c changing from $\pi/2$ to π. (d) represents κ_1 with k_c changing from 0 to $\pi/2$ for $l = 3$.

note that the scaling behavior is related to the band structure at low energy. Now we look at the case with $l = 2$. For the reason that the critical properties are found symmetric about $a = 0$, we discuss the phase boundaries with $0 < a < 2$. In Fig. 4.10(c) we present the scaling coefficient κ_1 when the Ising interaction a changes. We note that the scaling coefficient κ_1 changes smoothly along the XY critical lines (green-solid lines). This behavior arises because the band structure in the phase boundaries are characterized by the same topology. Specifically, in M_3 there are two degenerate points (or Dirac points) – see Fig. 4.9(c). As for M_4, there are three degenerate points in the band structure. Therefore, M_4 enjoys a $so(3)_1$ criticality rather than the XY one. Therefore, the scaling coefficients exhibit different discontinuity between M_4 and the XY type critical points as shown in Fig. 4.10.

As for topological quantum phase transitions, we first consider $l = 2$. At M_0, the quantum phase transition between a paramagnet and a cluster phase occurs. Similarly, M_4, M_2 at $a = \pm 1$ are quantum multicritical points involving the cluster phase. We found that the same scaling behaviour is displayed in M_2 and M_4. The ratio $|\kappa_2/\kappa_1| \sim 1$ (see

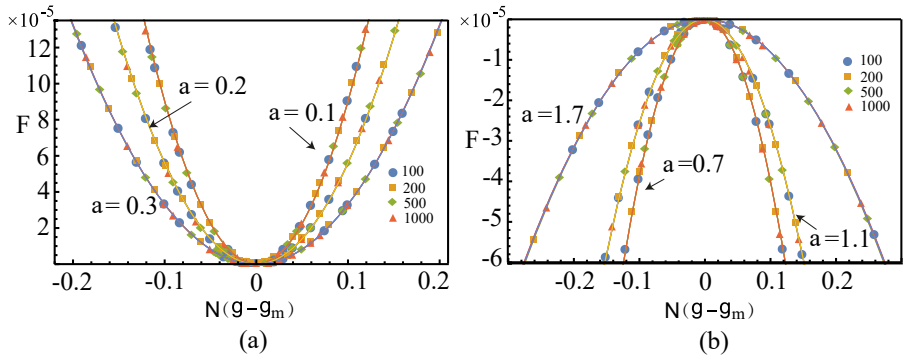

Figure 4.11: The value of $F = [1 - \exp(d\varphi/dg - d\varphi/dg|_{g_m})]$ as a function $N(g - g_m)$ for various lattice sizes, $N = 100, 200, 500, 1000$.

Eq. (4.37) and Eq. (4.38)). For $a = 0$, phase transitions occur at $|g| = 1$. As $|g| > 1$, the ground state is a trivial insulator(P phase). However, if $|g| < 1$, the ground state is a symmetry protected cluster phase. As expected by looking at the dispersion curves M_0 and M_3 share the same criticality. A similar finding holds for M_2 and M_4. The scaling coefficient κ_1 for $l = 3$ is represented in Fig. 4.10(d). For multicritical points with multiple degeneracies in energy bands, the scaling coefficients are discontinuously connected to the neighboring critical points which share the same topologies of band structures.

Furthermore, by proper scaling and taking into account the distance of the extremum of geometric phase from the critical points, it is possible to make all the data for the value of $F = [1 - \exp(d\varphi/dg - d\varphi/dg|_{g_m})]$ as a function of $N^{1/\nu}(g - g_m)$ for different N collapse onto a single curve [139, 62]. In (a), the curves for $a = 0.1, 0.2, 0.3$ are shown. In (b), the curves for $a = 0.7, 1.1, 1.7$ are presented.

4.4.3 Scaling Behavior of Quadratic Dispersions

In Fig. 4.7 there are a kind of critical points which are joint points between XY and Ising classes, i.e., M_1 and M_5 in (b). M_1 and M_5 are non-Lorentz-invariant critical points. These point have special energy band structure. In Fig. 4.9(b), we can see that the low energy dispersion is quadratic in k. The phase transition is characterized by the dynamical critical component $z = 2$. And the phase transitions can not described by Lorentz-invariant conformal field theory. From numerical calculations, we find the scaling behaviors as shown in Fig. 4.12. At M_1 and M_5 the scaling ansatz in Eq. (4.37) and

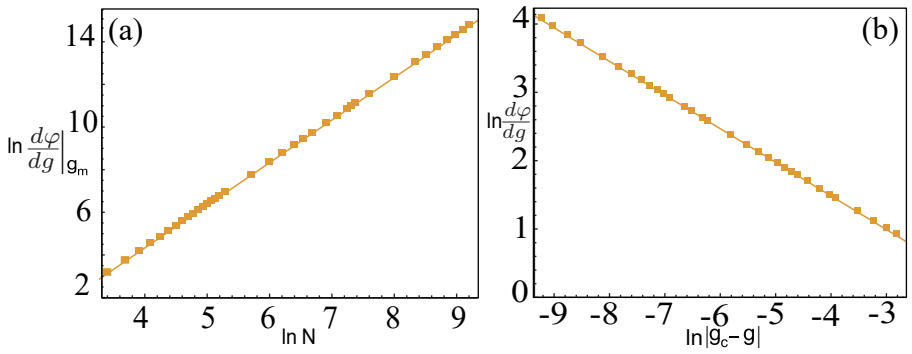

Figure 4.12: Scaling behavior for the point M_5.

Eq. (4.38) changes to

$$\ln \frac{d\varphi}{dg}|_{g_m} \simeq \tilde{\kappa}_1 \ln N + \text{const}, \tag{4.39}$$

and

$$\ln \frac{d\varphi}{dg} \simeq \tilde{\kappa}_2 \ln |g - g_c| + \text{const}. \tag{4.40}$$

Because of the quadratic dispersion, the scaling behaviors are found to be logarithmic. Fig. 4.12(a) and (b) show $\tilde{\kappa}_1$, and $\tilde{\kappa}_2$ being 1.999 and -0.492, respectively. Close to critical points with quadratic dispersions for $l \geq 2$, we find a similar log scaling behavior. In Fig. 4.13 the low energy dispersions at $k_c = \pi$ are plotted around $a = 2$. When the system is close to $a = 2$, the dispersion has smaller slope, but still linear. When it reaches $a = 2$, it becomes k^2 dispersion.

We have studied the phase diagrams and quantum criticalities of generalized cluster-Ising models through the winding number and scaling properties of the geometric phase, respectively. The critical points with linear and quadratic low-energy dispersions obey

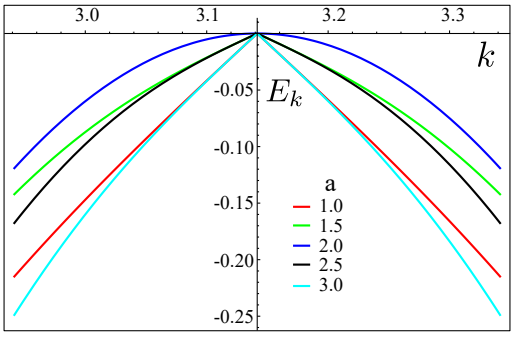

Figure 4.13: Dispersion curves around $k_c = \pi$ for various values of a.

different scaling ansatz. Specifically, the critical point with critical exponent $z = 2$ shows anomalous logarithmic scaling behavior which is markedly different from that one with $z = 1$, with linear dispersions. There is a close connection between topological phase transition, quantum criticality, energy band structure and geometric phase.

Chapter 5

Statistical Properties of Quenched Edge States

Recently, nonequilibrium physics has attracted a lot of interest in eigenstate thermalization hypothesis (ETH) which states that an isolated quantum many-body system would relax to a state well described by the standard statistical-mechanical prescription [147, 148]. Experiments, especially ultracold atoms [149, 150, 151, 152, 153], provide a flexible platform to perform nonequilibrium controlling. Quantum quench is one typical approach to drive systems from equilibrium state to non-equilibrium. Many systems have been considered: cold atoms [154], circuit-QED [50], quantum dots [155] and so forth. Even in topological systems, quantum quenches are shown to exhibit many interesting effects and applications, for instance, band tomography [156], dynamical phase transition (DPT) [157, 158], preservation of Chern number [159], by discussing the band properties. Response of edge states to quantum quench are also explored in open-boundary topological systems [159, 160]. In addition, edge modes with nonequilibrium dynamics has also been investigated, e.g., by discussing the scaling of topological defects [161, 162] and survival probability [163, 164].

In general, physical properties for nonequilibrium systems are manifested through some dynamical observables. Measures, like Loschmidt echo (LE) which is also known as the "return" probability, captures the fidelity of the system after a quantum quench. Moreover, LE is a useful technique that can characterize many phenomena, phase transition or DPT [52, 165], non-Markovianity [166], and the statistical work done in quench process [167]. In topological systems, LE is shown to indicate DPT via Fisher zeros [157]. However, many of these works explore the physics via dynamical observables. As noted in [168, 169], probability distributions in quantum quench are the essence of nonequilibrium

systems. Indeed, those dynamical observables extract information of systems, which can fully captured by probability distribution. In particular, the long-time behavior of the quenched system is described by the probability distribution.

5.1 Loschmidt Echo, Work, and Probability Distribution

Usually, LE is utilized to explore the dynamical behavior of a system. LE is a versatile technique and can be related to a lot of interesting effects, such as decoherence, phase transition and non-Markovianity. Loschmidt amplitude (LA) is defined as the overlap between the initial state and the final state,

$$\begin{aligned} G(t) &= \langle\psi_0|e^{-iH_1 t}|\psi_0\rangle \\ &= \sum_{n=1}^{2N} P_n e^{-iE_n t}, \end{aligned} \tag{5.1}$$

where $P_n = |\langle\psi_0|\Phi_n\rangle|^2$ and $|\psi_0\rangle$ is the initial state before quench, and $|\Phi_n\rangle$ are the nth instantaneous eigenstate of quenched Hamiltonian H_1. To physically quantify the dynamics, LE, i.e. $L(t) = |G(t)|^2$ is usually used. It is clear that LE can be understood as a "return" probability, and it is really an interference effect. The statistics of work done during the process of a quench is analyzed in Ref. [167]. This has motivated people to investigate the relation between probability distribution and physical properties in nonequilibrium systems [170, 171, 168, 172, 173].

Specifically, it has been found in Ref. [171] that the choice of the initial state is important. When the quenched term $H_1 - H_0$, where H_0, H_1 are initial and quenched Hamiltonian in spin$-1/2$ systems, commutes with H_0, magnetic susceptibilities can be interpreted as cumulant of magnetization distribution of initial state. The choice of initial states can make the quench problem very different [174]. Usually, in equilibrium many-body systems, phase transitions are characterized by properties of low energy states. For topological systems, topological invariants change when bandgap closes, and correspondingly the number of edge modes changes. However, topological invariants are not merely reflected by the low energy characteristics of a system [117]. For the systems under quench with topological features, one of the edge states could be chosen as an initial state. As shown in [159, 160], responses of edge states to sudden quench are highly interesting. Depending on the quenches, the LE exhibits quite different dynamical behaviors. Here,

we study the problem in a different way. We consider the long-time properties of the quenched edge state.

5.2 Mixed State Description of Long-time Average of Quenched System

For a system H_0 with eigenstate $|\psi_0\rangle$, the quantum state when the system is suddenly quenched to a new Hamiltonian H_1 is

$$\begin{aligned} |\Psi(t)\rangle &= e^{-iH_1 t}|\psi_0\rangle \\ &= \sum_n e^{-iE_n t} C_n |\Phi_n\rangle, \end{aligned} \tag{5.2}$$

where $|\Phi_n\rangle$ and E_n are eigenstates and eigenenergies of H_1 and $C_n = \langle\Phi_n|\psi_0\rangle$. An observable for the system after sudden quench can be written as

$$\begin{aligned} O(t) &= \langle\Psi(t)|O|\Psi(t)\rangle \\ &= \sum_n P_n \langle\Phi_n|O|\Phi_n\rangle + \sum_{n\neq m} C_n C_m^* e^{-iE_{nm}t} \langle\Phi_m|O|\Phi_n\rangle \end{aligned} \tag{5.3}$$

with $E_{nm} = E_n - E_m$ and $P_n = |C_n|^2$. P_n is called probability distribution and is the nth diagonal element of density matrix $\rho(t) = |\Psi(t)\rangle\langle\Psi(t)|$. To characterize the steady state after relaxation, one can define long-time average of $O(t)$ as

$$\begin{aligned} \overline{O} &= \lim_{T\to\infty} \frac{1}{T} \int_0^T dt O(t) \\ &= \sum_n P_n \langle\Phi_n|O|\Phi_n\rangle + \lim_{T\to\infty} \frac{1}{T} \int_0^T dt \sum_{n\neq m} C_n C_m^* e^{-i(E_{nm})t} \langle\Phi_m|O|\Phi_n\rangle. \end{aligned} \tag{5.4}$$

The average is taken over an integral multiple of the period. If no degeneracy appears, the second term is zero according to Riemann-Lebesgue lemma. We can write fidelity into two parts $O(t) = \overline{O} + \delta O(t)$ where $\delta O(t)$ denotes the fluctuation about the average. In some non-topological many-body systems [154, 54], the fluctuation part characterizes the nonequilibrium phenomenon. Even in topological systems, the dynamical properties show differences for various quenches [164].

Ergodic theorem guarantees the thermalization in isolated many-body systems in which it applies. In such systems, no matter what initial states are, the final states always

evolve to thermalized steady states. However, in integrable systems with its eigenstate being initial state, thermalization is not possible. However, the steady state can still be described by an ensemble, i.e., generalized Gibbs ensemble (GGE) [148]

$$\rho_G = \frac{e^{-\sum_\alpha \lambda_\alpha \mathcal{I}_\alpha}}{\mathrm{Tr}[e^{-\sum_\alpha \lambda_\alpha \mathcal{I}_\alpha}]}, \tag{5.5}$$

where λ_α are Lagrange multipliers constraining the value of each conserved quantity $\mathcal{I}_\alpha$ in the postquench system, i.e., $\langle\psi_0|\mathcal{I}_\alpha|\psi_0\rangle = \mathrm{Tr}[\rho_G \mathcal{I}_\alpha]$. In our case, $\mathcal{I}_\alpha$ are number operators on the energy eigenstates of postquench system. ρ_G is GGE ensemble established in studying the issue of thermalization of isolated systems and is actually the long-time steady state after sudden quench [148]. From Eq. (5.4) and Eq. (5.5), one can easily find that

$$\overline{O} = \mathrm{Tr}[\rho_G O]. \tag{5.6}$$

The mixed state of the topological models continues to exhibit topological properties until the critical temperature [36]. One interesting question is: can the effective ensemble of the quenched system convey topological information? In the following, we explore the relation between the long-time steady state and the topology.

5.3 Aubry-André-Harper model

The AAH model is a 1D tight binding model [175, 176]. This 1D model can be used to realize topological particle pumping [177], and the relation to zero modes is also analyzed [128]. Moreover, the physics that happens in AAH model is related to other topological models in 1D, such as Kitaev chain, SSH model [128]. The AAH model can be described as

$$\begin{aligned} H = & \sum_{i=1}^{N-1} t[1 + \lambda \cos(2\pi\beta i + \varphi_\lambda)]\hat{a}_{i+1}^\dagger \hat{a}_i + h.c. \\ & + \sum_{i=1}^{N} v \cos(2\pi\beta i + \varphi_v)\hat{a}_i^\dagger \hat{a}_i. \end{aligned} \tag{5.7}$$

When $\lambda = 0$, it is called diagonal-AAH model and it is topologically trivial. This diagonal model has been used to analyze disorder and localization of Bose-Einstein condensate in quasiperiodic optical lattice [178]. However, if λ is nonzero, the system is topologically nontrivial. AAH model can be mapped to its 2D ancestor model with φ_v being the crystal

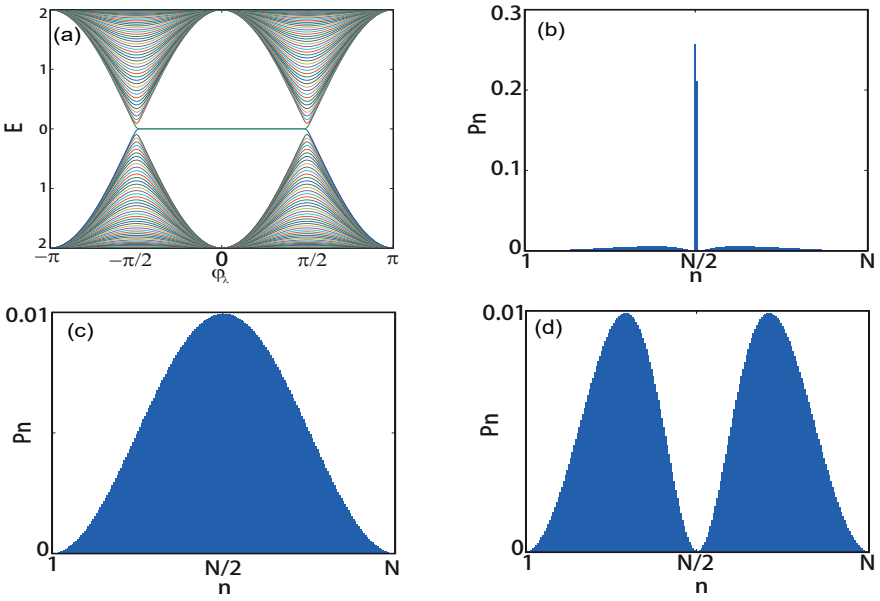

Figure 5.1: Energy spectrum with $\lambda = 1, v = 0, t = 1$ (a). (b)-(d) probability distributions for three quenches from $\varphi_\lambda = 0$ to 0.45π, 0.5π, and 0.7π, respectively. Other parameters are .

momentum in the second dimension [179]. We consider a simple situation with $v = 0$. The inhomogeneous hopping is tuned by the cosine modulation. $\beta = 1/m$ means m sublattices in the unit cell. When $\beta = 1/2$, it resembles SSH model as we have studied. Incommensurate lattice has also been studied in terms of Anderson localization in 1D system with BEC [178]. The recent studies find that quasicrystal with incommensurate ratio β has the same topological origin as AAH model [23, 177].

For open boundary one-dimensional lattice, there are two edge modes appearing at the two ends, separated from each other. We first consider initial edge mode at zero energy, which means edge state degeneracy for infinite length of lattice. For simplicity, we let $t = 1, \lambda = 1, \beta = 1/2$. The spectrum is plotted in Fig. 5.1(a). When $-\frac{\pi}{2} < \varphi_\lambda < \frac{\pi}{2}$ there are two edge modes appearing at two ends of the lattice. Assuming that the initial state is an edge state with $\varphi_\lambda = 0$, then one can quench the system by changing φ_λ to $0.45\pi, 0.5\pi, 0.7\pi$ corresponding to (b)-(d), respectively. The probability distributions in (b)-(d) reveal that the ground band and excited band are symmetrically populated. This is imposed by the initial condition $\langle\Psi_0|H_0|\Psi_0\rangle = 0$. For this reason, periodic revival occurs [164].

We next consider the general model with both diagonal and off-diagonal, with the off-

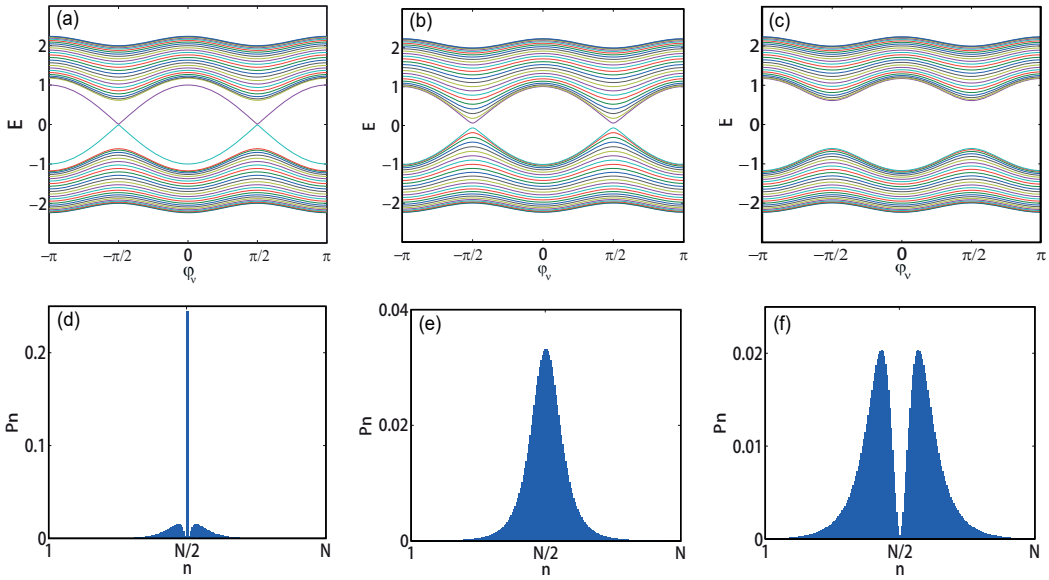

Figure 5.2: (a-c): spectrums for $\lambda = 0.3, 0, -0.3$. (d-f) probability distributions for quenches from $\lambda = 0.3$ to $\lambda = 0.05, 0, -0.3$, respectively, with $\varphi_v = \pi/2$. $v = 1, \varphi_\lambda = 0, t = 1, N = 50$.

diagonal parameter λ as the quenched variable. In Fig. 5.2(a)-(c), energy spectrums are shown with $\lambda = 0.3, 0, -0.3$, respectively. The system is initialized at $\lambda = 0.3, \varphi_v = \pi/2$ where the edge states at two ends are degenerate. Probability distributions in (d)-(f) represent quantum quench to $\lambda = 0.05, 0, -0.3$. As we see, distributions are symmetric along the energy axis for all cases. In Fig. 5.3, the system is chosen with lower edge mode at $\lambda = 0.3, \varphi_v = 0.2\pi$, which is far from the degeneracy point. Fig. 5.3(a)-(c) show the quench from $\lambda = 0.3$ to $\lambda = -0.3, 0, 0.05$, respectively. The unbalanced behavior shows the overlap between initial state and eigenstates of post-quenched system.

5.4 Fidelity and Entropy

An observable for the system after quench can be written as $O(t) = \langle\Psi(t)|O|\Psi(t)\rangle$, with $|\Psi(t)\rangle = \sum_n e^{-iE_n t}\langle\Phi_n|\psi_0\rangle|\Phi_n\rangle$. To capture the main dynamical behaviors of the system,

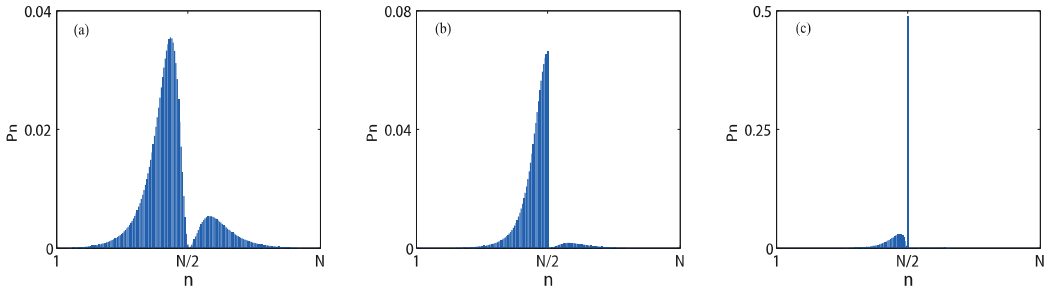

Figure 5.3: Probability distributions for different quenches. The initial edge state is chosen as one with lower energy at $\lambda = 0.3, \varphi_v = 0.2\pi$. (a)-(c) correspond to the quenches $\lambda = -0.3, 0, 0.05$, respectively.

we choose fidelity [180] as an measurement, i.e.,

$$\begin{aligned} F(t) &= \langle\psi_0|\Psi(t)\rangle\langle\Psi(t)|\psi_0\rangle \\ &= \langle\psi_0|\Big(\sum_{n,m} e^{-iE_{nm}t}\langle\Phi_n|\psi_0\rangle\langle\psi_0|\Phi_m\rangle|\Phi_n\rangle\langle\Phi_m|\Big)|\psi_0\rangle \\ &= \sum_{n,m} e^{-iE_{nm}t}\langle\psi_0|\Phi_m\rangle\langle\Phi_m|\psi_0\rangle\langle\psi_0|\Phi_n\rangle\langle\Phi_n|\psi_0\rangle \\ &= \sum_{n,m} e^{-iE_{nm}t}P_m P_n, \end{aligned} \tag{5.8}$$

The dynamical survival probability of initial state shows differences for various quenches [164]. To explore deeper relation between topological quench and the response of system, the long-time steady state should be analyzed. The initial state is the edge mode which is labeled as N/2 from the lowest energy state. Long-time average of $F(t)$ is

$$\overline{F} = \lim_{T\to\infty}\frac{1}{T}\int_0^T dt F(t). \tag{5.9}$$

From Eq. (5.6), we have

$$\overline{F} = \mathrm{Tr}[\rho_G|\psi_0\rangle\langle\psi_0|]. \tag{5.10}$$

As shown in Fig. 5.4(a), when quantum quench is done in the same phase, $\overline{F}$ has finite value. But, if the post-quenched system belongs to a different phase, it exhibits quite different behaviors: namely, $\overline{F}$ approaches zero if the system is quenched over the critical point. In Fig. 5.4(b) von Neumann entropy (VNE) $S(\rho) = -\mathrm{Tr}[\rho\ln\rho]$ is shown for ρ_G. Even though the probability distribution P_n is quite different for $\varphi_v = 0.5\pi$ (Fig. 5.2(d))

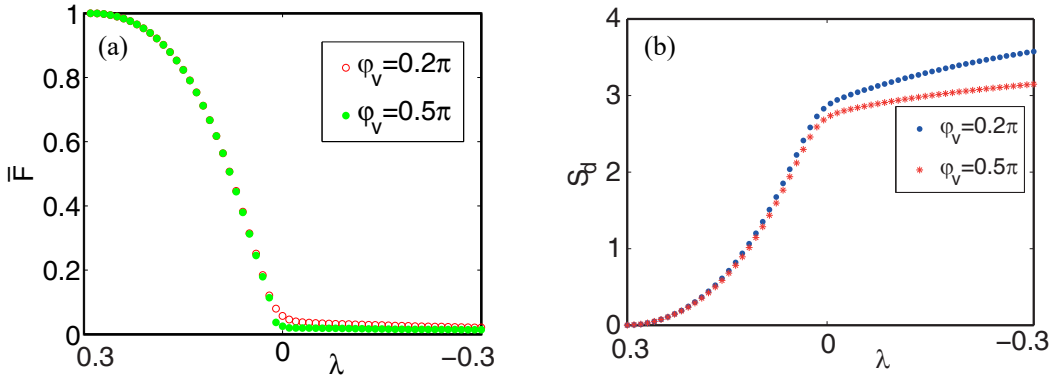

Figure 5.4: Long-time average of fidelity (a) and von Neumann entropy (b), with $T = 1200, t = 1, v = 1, b = 1/2, \varphi_\lambda = 0, N = 200$.

and $\varphi_v = 0.2\pi$ (Fig. 5.3(c)), VNE does not make so much difference.

Chapter 6

Detection of Topological Quantum Number in Circuit-QED System

In previous chapters, we have discussed the Aharonov-Bohm effects and topological phenomena with neutral atoms. In this chapter, we study the topological effects in periodic photonic systems. The photonic edge states and quantum Hall effect in photonic crystals have been studied by Haldane and Raghu [181] and also probed experimentally [182]. Recently, artificial gauge fields for photons are also investigated in many photonic systems [183, 184, 185, 186, 187]. Moreover, the photons in microwave frequency are proposed for simulating condensed matter effects [188, 189]. In particular, Koch *et al.* propose a special passive coupling element between microwave resonators [189]. As a result, the time-reversal symmetry can be broken and artificial gauge field is generated [189]. The use of passive coupling elements can avoid some of the challenges posed by dissipation. The experiments have realized artificial gauge field in circuit-QED systems recently [190].

At first, for electromagnetic waves, one can mimick topological features by fabricating periodic structures in photonic crystal [191, 182, 129] or coupled cavity array [192]. In particular, topological Floquet insulator can be realized in an array of evanescently coupled helical waveguides where the propagation coordinate z acts as 'time' in experiment [193]. The graphene-like lattice is fabricated to simulate the topological effects in honeycomb lattice. In the photonic crystal, the properties of photons in the lattice can be tuned in various ways, e.g., external driving, interaction with atoms, cavity decay. The cavity decay is also exploited to observe the topological phase transitions [24]. Here, we focus on the circuit-QED lattice where microwave photons can hop between neighboring resonators/cavities with the mediation of atoms [194, 195]. The advantage for the atom-mediated hopping is that one can tune the atoms in such a way that topological

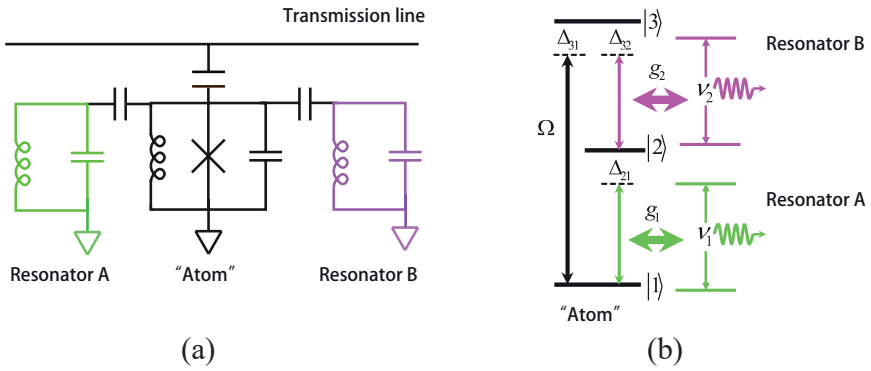

Figure 6.1: (a) The circuit diagram of two resonators and a flux qubit. (b) The energy levels and interactions with resonators.

properties of photons can be changed.

Before the discussion of photonic lattice, we first consider the quantum system with simple atom-photon interaction. In quantum optics, the interaction between atom and photon is a fundamental tool to engineer quantum state [196], cool resonator [197], etc. If several modes of photons are coupled to atoms, the effective interactions (linear and nonlinear) can be obtained, which are useful to study many-body physics for photons [198, 199]. In the following, we consider the atom-mediated two resonators which will be used to generate topological states in later sections. This simple quantum system has significant applications in quantum optics and quantum information processing, e.g., generating entanglement between resonators [200, 201], producing noninear photon hopping [202].

6.1 Atom-Mediated Two Resonators: Entangled States

The circuit-QED system is a nice setup to perform quantum optical effects and realize quantum information processing [203, 204]. The entanglement between resonators can be realized by coupling them to a three level superconducting artificial atom [205, 206]. The circuit of the system is shown in Fig. 6.1. The qubit we consider is the flux-type [207]. The energy levels of flux qubit can be tuned by the magnetic flux in the superconducting loop interrupted by Josephson junctions, which are marked by red and blue crosses in Fig. 6.1(a). The loop can be treated as a multilevel "atom". The transition elements between different levels can also be adjusted by magnetic flux. When the flux is properly tuned, cyclic transitions between three levels can be realized [208]. A control microwave field is applied to couple the levels $|1\rangle$ and $|3\rangle$ via the transmission line. In (b), the energy

levels of the "atom" are shown. Two resonators couple to the transitions $|1\rangle \leftrightarrow |2\rangle$ and $|2\rangle \leftrightarrow |3\rangle$, respectively. The Hamiltonians for the driven atom and the interaction between resonators and atoms are H_0 and H_1

$$H_0 = \sum_{j=1}^{2} \nu_j \hat{a}_j^\dagger \hat{a}_j + \sum_{k=2}^{3} \omega_{k1}\sigma_{kk} + \Omega(\sigma_{13}e^{i\nu_3 t} + \sigma_{31}e^{-i\nu_3 t}). \tag{6.1}$$

$$H_1 = g_1(\hat{a}_1^\dagger \sigma_{12} + \hat{a}_1\sigma_{21}) + g_2(\hat{a}_2^\dagger\sigma_{23} + \hat{a}_2\sigma_{32}). \tag{6.2}$$

Here $\nu_{1,2}$ are the frequencies of the two harmonic oscillators. ν_3 is the frequency of the microwave field. $\hat{a}_j^\dagger$ and $\hat{a}_j$ are creation and annihilation operators of the two oscillators, respectively. σ_{jj} and $\sigma_{jk}(j \neq k, j, k = 1, 2, 3)$ are projection operators and transition operators of the atom, respectively. g_1 and g_2 represent the atom-resonator interactions, and Ω is the Rabi frequency of the driven transition $|3\rangle \leftrightarrow |1\rangle$. In the rotating frame, the Hamiltonians change to

$$\tilde{H}_0 = \Delta_{31}\sigma_{33} + \Omega(\sigma_{13} + \sigma_{31}). \tag{6.3}$$

$$\tilde{H}_1 = g_1(\hat{a}_1^\dagger\sigma_{12}e^{-i\Delta_{21}t} + \hat{a}_1\sigma_{21}e^{i\Delta_{21}t}) + g_2[\hat{a}_2^\dagger\sigma_{23}e^{-i(\Delta_{32}-\Delta_{31})t} + \hat{a}_2\sigma_{32}e^{i(\Delta_{32}-\Delta_{31})t}], \tag{6.4}$$

where $\Delta_{31} = \omega_{31} - \nu_3$, $\Delta_{32} = \omega_{32} - \nu_2$, $\Delta_{21} = \omega_{21} - \nu_1$ $\omega_{jk} = \omega_j - \omega_k$ are frequency differences between three energy levels. After diagonalization of $\tilde{H}_0$ we obtain the dressed states which are superpositions of bare states

$$|+\rangle = \cos\theta|3\rangle + \sin\theta|1\rangle, \qquad |-\rangle = -\sin\theta|3\rangle + \cos\theta|1\rangle, \tag{6.5}$$

where we define $\cos\theta = \sqrt{\frac{1}{2} + \frac{\Delta}{2d}}$, $\sin\theta = \sqrt{\frac{1}{2} - \frac{\Delta}{2d}}$, $d = \sqrt{\Delta^2 + 4\Omega^2}$ and $\Delta_{31} = \Delta$. The dressed states $|+\rangle$ and $|-\rangle$ have the eigenvalues $\lambda_\pm = \frac{1}{2}(\Delta \pm d)$, respectively. In the eigenstates representation, $\tilde{H}_0 = \lambda_+\sigma_{++} + \lambda_-\sigma_{--}$. Considering a unitary transformation $U' = \exp(-i\tilde{H}_0 t)$, the system is described by

$$\begin{aligned} H_{int} \;=\; & g_1\hat{a}_1^\dagger[\sin\theta\sigma_{+2}e^{i(\lambda_+ - \Delta_{21})t} + \cos\theta\sigma_{-2}e^{i(\lambda_- - \Delta_{21})t}] + g_2\hat{a}_2^\dagger[\cos\theta\sigma_{2+}e^{-i[\lambda_+ + (\Delta_{32}-\Delta_{31})]t} \\ & - \sin\theta\sigma_{2-}e^{-i[\lambda_- + (\Delta_{32}-\Delta_{31})]t}] + h.c. \end{aligned} \tag{6.6}$$

Here we consider the three-photon resonance conditions, i.e., $\Delta_{21} = \Delta_{31} - \Delta_{32}$. By tuning Rabi sideband resonance $\lambda_+ = \Delta_{21}$ and neglecting these fast oscillating terms, we can

obtain the reduced Hamiltonian as

$$H_I = (g_1\hat{a}_1^\dagger \sin\theta + g_2\hat{a}_2 \cos\theta)\sigma_{+2} + h.c. \tag{6.7}$$

Then we introduce a Bogoliubov transformation,

$$\begin{aligned} \hat{b}_1 &= \hat{a}_1 \cosh r + \hat{a}_2^\dagger \sinh r, \\ \hat{b}_2 &= \hat{a}_2 \cosh r + \hat{a}_1^\dagger \sinh r, \end{aligned} \tag{6.8}$$

where the squeezing parameter is defined as

$$r = \arctan\sqrt{\frac{d-\Delta}{d+\Delta}} \quad (\Delta > 0), \tag{6.9}$$

$$r = \arctan\sqrt{\frac{d+\Delta}{d-\Delta}} \quad (\Delta < 0). \tag{6.10}$$

The Hamiltonian H_I is written with the new operators b_1 and b_2 as

$$\tilde{H}_{I_2} = G(\hat{b}_2\sigma_{+2} + \hat{b}_2^\dagger\sigma_{2+}) \quad (\Delta > 0), \tag{6.11}$$

$$\tilde{H}_{I_1} = G(\hat{b}_1\sigma_{2+} + \hat{b}_1^\dagger\sigma_{+2}) \quad (\Delta < 0), \tag{6.12}$$

where the effective coupling constant $G = \sqrt{|g_2^2\cos\theta^2 - g_1^2\sin\theta^2|}$. In the dressed states representation Eq. 6.5, the mater equation of the system is written as

$$\dot{\tilde{\rho}} = -i[\tilde{H}_I, \tilde{\rho}] + \mathcal{L}_a\tilde{\rho} + \mathcal{L}_c\tilde{\rho}, \tag{6.13}$$

with

$$\begin{aligned} \mathcal{L}_a\tilde{\rho} = & \sum_{m,n=+,-,2}^{m\neq n} \frac{\Gamma_{mn}}{2}(2\sigma_{nm}\tilde{\rho}\sigma_{mn} - \sigma_{mm}\tilde{\rho} - \tilde{\rho}\sigma_{mm}) - \sum_{k,j=+,-}^{k\neq j}[\frac{\Gamma^{kj}_{1_{in}}}{2}(2\sigma_{2k}\tilde{\rho}\sigma_{j2} - \sigma_{jk}\tilde{\rho} - \tilde{\rho}\sigma_{jk}) \\ & -\Gamma^{kj}_{2_{in}}\sigma_{k2}\tilde{\rho}\sigma_{2j}] + \Gamma_{ph_1}(\sigma_{++}\tilde{\rho}\sigma_{--} + \sigma_{--}\tilde{\rho}\sigma_{++}) + \frac{\Gamma_{ph_2}}{2}(2\sigma_p\tilde{\rho}\sigma_p - \sigma_p\sigma_p\tilde{\rho} - \tilde{\rho}\sigma_p\sigma_p) \\ & + \sum_{l=+,-,2}\frac{\Gamma_{ll}}{2}(2\sigma_{ll}\tilde{\rho}\sigma_{ll} - \sigma_{ll}\tilde{\rho} - \tilde{\rho}\sigma_{ll}), \end{aligned} \tag{6.14}$$

and

$$\begin{aligned}\mathcal{L}_c\tilde{\rho} &= \frac{\kappa}{2}[\sum_{j=1}^{2}(N_j+1)(\hat{b}_j\tilde{\rho}\hat{b}_j^\dagger-\hat{b}_j^\dagger\hat{b}_j\tilde{\rho})+N_j(\hat{b}_j^\dagger\tilde{\rho}\hat{b}_j-\tilde{\rho}\hat{b}_j\hat{b}_j^\dagger)]\\ &\quad+\kappa M(\tilde{\rho}\hat{b}_1\hat{b}_2+\hat{b}_1\hat{b}_2\tilde{\rho}-\hat{b}_1\tilde{\rho}\hat{b}_2-\hat{b}_2\tilde{\rho}\hat{b}_1)+h.c.,\end{aligned} \tag{6.15}$$

where $\sigma_p=\sigma_{++}-\sigma_{--}$. We assume that the decay rates of resonators are the same, i.e., $\kappa_1=\kappa_2=\kappa$. The parameters in the above expressions are

$$\begin{aligned}\Gamma_{+-} &= \gamma_{31}\cos^4\theta+\frac{\gamma_{33}}{4}\sin^2 2\theta,\\ \Gamma_{-+} &= \gamma_{31}\sin^4\theta+\frac{\gamma_{33}}{4}\sin^2 2\theta,\\ \Gamma_{+2} &= \gamma_{32}\cos^2\theta,\quad \Gamma_{-2}=\gamma_{32}\sin^2\theta,\\ \Gamma_{2+} &= \gamma_{21}\sin^2\theta,\quad \Gamma_{2-}=\gamma_{21}\cos^2\theta,\\ \Gamma_{1_{in}}^{+-} &= \Gamma_{1_{in}}^{-+}=\frac{\gamma_{32}}{2}\sin 2\theta,\\ \Gamma_{2_{in}}^{+-} &= \Gamma_{2_{in}}^{-+}=\frac{\gamma_{21}}{2}\sin 2\theta,\\ \Gamma_{ph_1} &= \frac{\gamma_{33}}{4}\sin^2 2\theta,\quad \Gamma_{ph_2}=\frac{\gamma_{31}}{4}\sin^2 2\theta,\\ \Gamma_{++} &= \gamma_{33}\cos^4\theta,\Gamma_{--}=\gamma_{33}\sin^4\theta,\Gamma_{22}=\gamma_{22},\\ N_1 &= N_2=\sinh^2 r,\quad M=\sinh r\cosh r,\end{aligned} \tag{6.16}$$

in which the terms $\Gamma_{mn}(m,n=+,-,2,m\neq n)$ describe the incoherent population transfer between different dressed states, $\Gamma_{1_{in}}^{kj}$ and $\Gamma_{2_{in}}^{kj}(k,j=+,-,k\neq j)$ represent the cross correlations between the incoherent process $|\pm\rangle\rightarrow|2\rangle$ and $|2\rangle\rightarrow|\pm\rangle$, $\Gamma_{ph_j}(j=1,2)$ and $\Gamma_{kk}(k=+,-,2)$ are the phase damping terms, $N_j(j=1,2)$ and M denote the atomic reservoir effects. $\gamma_{jk}(j\neq k)$ denote decays from states $|j\rangle$ to $|k\rangle$. γ_{jj} are the dephasing rates for the states $|j\rangle$.

As an illustration, we consider the case $\Delta>0$ with the Hamiltonian Eq. 6.11. The reduced master equation $\tilde{\rho}_c'$ of the modes a_1 and a_2 is

$$\begin{aligned}\dot{\tilde{\rho}}_c' &= A_{11}(\hat{a}_1\tilde{\rho}_c'\hat{a}_1^\dagger-\hat{a}_1^\dagger\hat{a}_1\tilde{\rho}_c')+A_{22}(\hat{a}_1^\dagger\tilde{\rho}_c'\hat{a}_1-\hat{a}_1\hat{a}_1^\dagger\tilde{\rho}_c')\\ &+ B_{11}(\hat{a}_2\tilde{\rho}_c'\hat{a}_2^\dagger-\hat{a}_2^\dagger\hat{a}_2\tilde{\rho}_c')+B_{22}(\hat{a}_2^\dagger\tilde{\rho}_c'\hat{a}_2-\hat{a}_2\hat{a}_2^\dagger\tilde{\rho}_c')\\ &+ A_{12}(\hat{a}_1\tilde{\rho}_c'\hat{a}_2-\hat{a}_2\hat{a}_1\tilde{\rho}_c')+A_{21}(\hat{a}_2^\dagger\tilde{\rho}_c'\hat{a}_1^\dagger-\hat{a}_1^\dagger\hat{a}_2^\dagger\tilde{\rho}_c')\\ &+ B_{12}(\hat{a}_1^\dagger\tilde{\rho}_c'\hat{a}_2^\dagger-\hat{a}_2^\dagger\hat{a}_1^\dagger\tilde{\rho}_c')+B_{21}(\hat{a}_2\tilde{\rho}_c'\hat{a}_1-\hat{a}_1\hat{a}_2\tilde{\rho}_c')\\ &+ \frac{\kappa}{2}(\hat{a}_1\tilde{\rho}_c'\hat{a}_1^\dagger-\hat{a}_1^\dagger\hat{a}_1\tilde{\rho}_c')+\frac{\kappa}{2}(\hat{a}_2\tilde{\rho}_c'\hat{a}_2^\dagger-\hat{a}_2^\dagger\hat{a}_2\tilde{\rho}_c')+h.c.,\end{aligned} \tag{6.17}$$

where the coefficients A_{mn} and $B_{mn}(m,n=1,2)$ are given as

$$\begin{aligned}
A_{11} &= \frac{\kappa}{2}\alpha_{22}\sinh^2 r, \quad A_{22} = \frac{\kappa}{2}\alpha_{11}\sinh^2 r, \\
B_{11} &= \frac{\kappa}{2}\alpha_{11}\cosh^2 r, \quad B_{22} = \frac{\kappa}{2}\alpha_{22}\cosh^2 r, \\
A_{12} &= A_{21} = \frac{\kappa}{2}\alpha_{22}\sinh r\cosh r, \\
B_{12} &= B_{21} = \frac{\kappa}{2}\alpha_{11}\sinh r\cosh r.
\end{aligned} \tag{6.18}$$

From the master equation Eq. 6.17, the c-number quantum Langevin equations of the modes a_1 and a_2 are derived as

$$\begin{aligned}
\frac{d\alpha_1}{dt} &= -(\frac{\kappa}{2}-\zeta_{11})\alpha_1 + \zeta_{12}\alpha_2^* + f_{\alpha_1}, \\
\frac{d\alpha_2}{dt} &= -(\frac{\kappa}{2}-\zeta_{22})\alpha_2 + \zeta_{21}\alpha_1^* + f_{\alpha_2},
\end{aligned} \tag{6.19}$$

where

$$\begin{aligned}
\zeta_{11} &= \frac{\kappa}{2}(\alpha_{11}^*-\alpha_{22})\sinh^2 r, \quad \zeta_{12} = \frac{\kappa}{2}(\alpha_{11}^*-\alpha_{22})\sinh r\cosh r, \\
\zeta_{21} &= \frac{\kappa}{2}(\alpha_{22}^*-\alpha_{11})\sinh r\cosh r, \quad \zeta_{22} = \frac{\kappa}{2}(\alpha_{22}^*-\alpha_{11})\cosh^2 r.
\end{aligned} \tag{6.20}$$

f_{α_1} and f_{α_2} are fluctuation forces of the modes with zero averages $\langle f_{\alpha_j}\rangle = 0$ and correlation functions $\langle f_x(t)f_y(t')\rangle = 2D'_{xy}\delta(t-t')$. The diffusion coefficients $2D'_{xy}$ can be calculated via the generalized Einstein relation and the nonzero diffusion coefficients are

$$\begin{aligned}
2D'_{\delta\alpha_1^*\delta\alpha_1} &= \frac{\kappa}{2}(\alpha_{11}^*+\alpha_{11})\sinh^2 r, \\
2D'_{\delta\alpha_2^*\delta\alpha_2} &= \frac{\kappa}{2}(\alpha_{22}^*+\alpha_{22})\cosh^2 r, \\
2D'_{\delta\alpha_1\delta\alpha_2} &= -\frac{\kappa}{2}(\alpha_{11}+\alpha_{22})\sinh r\cosh r, \\
2D'_{\delta\alpha_1^*\delta\alpha_2^*} &= -\frac{\kappa}{2}(\alpha_{22}^*+\alpha_{22}^*)\sinh r\cosh r,
\end{aligned} \tag{6.21}$$

wherein $2D'_{xy} = 2D'_{yx}$ and $2D'_{x^*y^*} = 2D'^*_{xy}$. Using the Duan's criterion [209], the variance sum Q of the original modes $\hat{a}_{1,2}$ is expressed as

$$Q = 2[1 + \langle\delta\alpha_1^*\delta\alpha_1\rangle + \langle\delta\alpha_2^*\delta\alpha_2\rangle + \langle\delta\alpha_1\delta\alpha_2\rangle + \langle\delta\alpha_1^*\delta\alpha_2^*\rangle]. \tag{6.22}$$

As shown in Fig. 6.2, the entanglement between two resonators is created when the

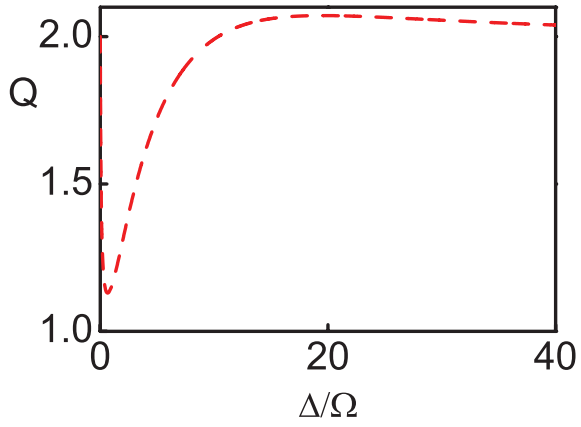

Figure 6.2: The variance sum Q of the original modes for $\Delta > 0$ as a function of the normalized detuning Δ/Ω. We choose $\kappa = 0.1\gamma; g_1 = g_2 = \gamma; \gamma_{31} = 2\gamma; \gamma_{21} = 0.2\gamma; \gamma_{33} = \gamma_{22} = \gamma$.

detuning is chosen properly.

6.2 Topological Photonic State in Atom-Mediated Resonator Array

In this section, we come to the topic of topological states based on the atom-mediated resonators. There are various models that support topological states. One possibility is the optical ring microresonators where the spins are encoded by the clockwise and counter-clockwise modes [191, 210]. In superconducting circuits several models have been suggested [211, 212, 213, 214]. The model we consider here is composed of periodic cells of the atom-mediated transmission line resonator. The photon hopping between nearest neighbour resonators is tuned through the coupling capacitors and the connected flux qubits, as shown in Fig. 6.3. a_n and b_n represent two different resonators a and b at the nth unit cell. The minimal setup of this circuit has been used to create entanglement between two end resonators [201]. Here, we consider the periodic lattice of this circuit. The capacitively coupled resonator lattice is described by the SSH Hamiltonian

$$H_0 = \sum_n J_1 \hat{a}_n^\dagger \hat{b}_n + J_2 \hat{a}_n^\dagger \hat{b}_{n-1} + h.c., \tag{6.23}$$

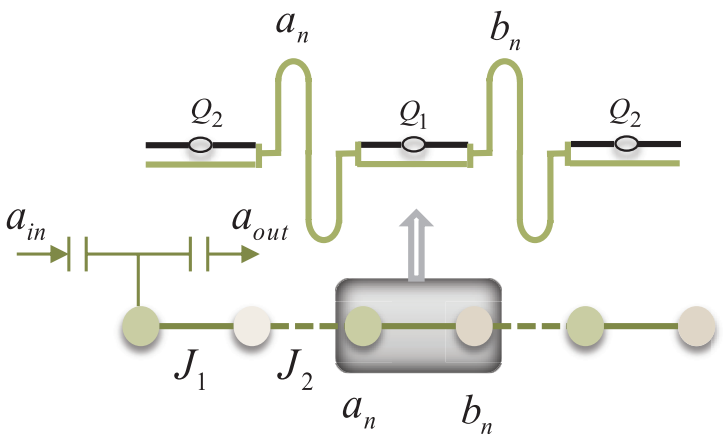

Figure 6.3: Setup for the one-dimensional circuit-QED lattice. The cavity input-output process is employed to probe the edge state.

where J_1 and J_2 are the intra- and inter-cell hopping amplitudes. For the qubit-assisted hopping, we assume that the two resonators within the same unit cell are both coupled to the flux qubit Q_1, while the two resonators belonging to the two nearest-neighbour unit cells are both coupled with the flux qubit Q_2. The atom-mediated coupling provides an alternating parametric modulation on the hopping amplitudes and the chemical potentials. In the dispersive regime, when all the qubits are in the ground state, the coupling between the resonator and the qubit can be removed, leading to an effective transmission resonator lattice with photon hopping assisted by the connected qubits. Combined with the previous capacitively coupled resonator lattice, the total Hamiltonian of this cicuit-QED lattice (in a rotating frame with respect to the external driving frequency ω_d and also in the interaction picture with respect to the qubit energy $\omega_{1,2}$) takes the form

$$\begin{aligned} H = \sum_n (J_1 - \frac{g_1 g_2}{\Delta})\hat{a}_n^\dagger \hat{b}_n + (J_2 + \frac{g_1 g_2}{\Delta})\hat{a}_n^\dagger \hat{b}_{n-1} + h.c \\ + \frac{g_2^2 - g_1^2}{\Delta}(\hat{a}_n^\dagger \hat{a}_n - \hat{b}_n^\dagger \hat{b}_n) + \Delta_c(\hat{a}_n^\dagger \hat{a}_n + \hat{b}_n^\dagger \hat{b}_n), \end{aligned} \tag{6.24}$$

where g_1 and g_2 describe the coupling strengths between the qubit $Q_1(Q_2)$ and the resonators a_n and b_n, (b_n and a_{n+1}), $\Delta = \omega_1 - \omega_d = \omega_d - \omega_2$ is the detuning of the qubit energies, and $\Delta_c = \omega_c - \omega_d$ is the detuning of the resonator frequency. The qubit-assisted hopping and on-site modulation terms are introduced in order to map into the effective second dimension. To simulate the two-dimensional Chern insulator Hamiltonian [69, 70], we write the qubit-resonator coupling strengths in the above lattice Hamiltonian

in a parameter space as

$$g_1 = g_0 \sin(\theta/2), g_2 = g_0 \cos(\theta/2), \tag{6.25}$$

where the mixing angle $\theta = 2\arctan(g_1/g_2)$ and $g_0 = \sqrt{g_1^2 + g_2^2}$. The parameter θ is determined by the ratio between the coupling strength g_1 and g_2. Note that the coupling strengths between the flux qubit and the resonators can be individually controlled through using superconducting quantum interferences (SQUIDs) devices and changing the external magnetic fluxes applied on the SQUIDs loops. Then θ can be engineered from 0 to 2π for subsequent two dimensional mapping. Moreover, the topological feature demonstrated below in this model endows this system with topological protection, which allows our methods to be robust to practical deformations in the parameters engineering. By substituting the above equation into the total lattice Hamiltonian and further writing it in momentum space, one can get $H = \sum_k C_k^\dagger h(k) C_k$, where $C_k = (\hat{a}_k, \hat{b}_k)^T$. The momentum density has the following form

$$h(k) = h_0 + h_x\sigma_x + h_y\sigma_y + h_z\sigma_z, \tag{6.26}$$

where $h_0 = \Delta_c$ and $\mathbf{h} = (h_x, h_y, h_z) = (2J\cos k_x, 2\delta \sin k_x - J_e \sin\theta \sin k_x, J_e \cos\theta)$ with $J = (J_1 + J_2)/2$, $\delta = (J_1 - J_2)/2$ and $J_e = g_0^2/\Delta$. $\sigma_{x,y,z}$ are the Pauli matrices spanned by $\hat{a}_k$ and $\hat{b}_k$. Now θ plays the role of the second dimension. This Hamiltonian can simulate two dimensional Chern insulator. The topological properties of present model are captured by the Chern number of the Bloch band and the edge state spectrum. By mapping the two-dimensional torus to a spherical surface, the Chern number of the occupied ground band can be expressed as

$$C = \frac{1}{4\pi} \int\int dk_x d\theta (\partial_{k_x} \hat{\mathbf{h}} \times \partial_\theta \hat{\mathbf{h}}) \cdot \hat{\mathbf{h}}, \tag{6.27}$$

where the unit vector $\hat{\mathbf{h}} = (h_x, h_y, h_z)/|h|$ with $|h| = \sqrt{h_x^2 + h_y^2 + h_z^2}$. Through substituting $h_{x,y,z}$ into above formula and one can get the Chern number of the ground band as

$$C = \begin{cases} 1 & \text{if } -J_e < 2\delta < J_e \\ 0 & \text{otherwise} \end{cases} \tag{6.28}$$

One can change the hopping difference δ to engineer the photonic topological phase transition. It is also worth pointing out that, when the coupling strength $g_2 = -g_0 \cos(\theta/2)$,

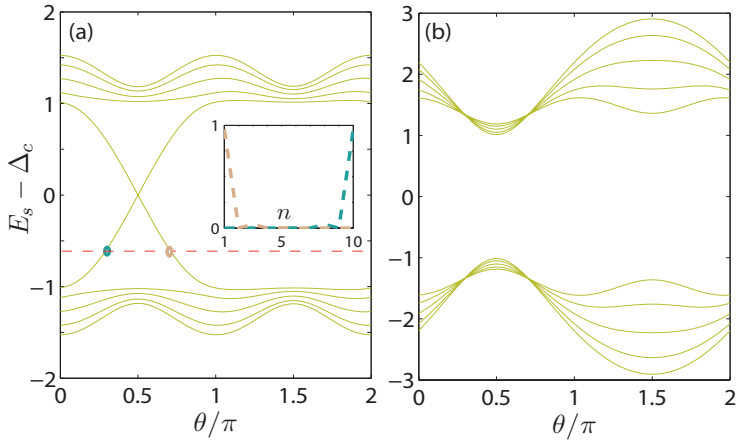

Figure 6.4: Energy spectrum of the lattice with (a) Chern number $C = 1$ for $\delta = 0$ and (b) Chern number $C = 0$ for $\delta = 0.6J_e$. For the Chern insulator, there are two edge states at the in-gap energy denoted by the red dashed line. The inset shows the density distribution of the two edge states. The other parameter are chosen as $J = J_e$ and the lattice size $L = 10$.

the ground state can be prepared as a Chern insulator with $C = -1$. According to the bulk-edge correspondence, the appearance of edge state is a hallmark of topological phase. In Fig. 6.4(a), we have plotted the edge state spectrum with various values of θ. There exist one pair of in-gap states which correspond to edge states localized at left and right boundaries of the lattice. The density distributions for the edge states are plotted in the inset figure of Fig. 6.4(a). We also show the spectrum for the topological trivial situation in Fig. 6.4(b) with no edge state in the gap.

6.3 Chern Number of Photonic Lattice

Based on Laughlin's pumping argument [215], recent scattering theory of topological insulators shows that topological invariant can be described by the reflection matrices at the Fermi level [216]. The basic experimental setup is achieved by rolling a two-dimensional topological system into a cylinder and threading it with a magnetic flux. For our one-dimensional photonic simulator, if we regard the left and right edges of the photonic lattice as the two ends of the cylinder, the periodic parameter θ as the external magnetic flux and the in-gap energy as the fermi level, our system can be naturally used to simulate the experimental setup in Laughlin's pumping argument and to test scattering theory of topological insulators. When the frequency of the incident photon towards one

edge is tuned into the in-gap energy and the external periodic parameter θ is tuned over one period, the pumping particle number per cycle can be expressed as

$$Q = \frac{1}{2\pi i}\int_0^{2\pi} d\theta \frac{d}{d\theta}\log r(\theta), \tag{6.29}$$

where $r(\theta)$ is the reflection coefficient of the incident photon from one edge. In this way, based on scattering theory of topological insulators [216], the topological invariant can be characterized by the winding number of the reflection coefficient phase [217]. To further demonstrate this point, we model the total system in the scattering process into three parts: left lead, device and right lead. We use Green function to analytically derive the reflection coefficient from the left edge of the above one-dimensional lattice. In particular, the reflection coefficient from the left lead is calculated below. The total lattice Hamiltonian of the system is $H = H_{\rm L} + H_{\rm LD} + H_{\rm D} + H_{\rm RD} + H_{\rm R}$, where

$$\begin{aligned}
H_{\rm D} &= \sum_{n=1}^{L/2}[(J_1 - \frac{J_e}{2}\sin\theta)\hat{a}_n^\dagger \hat{b}_n + (J_2 + \frac{J_e}{2}\sin\theta)\hat{b}_n^\dagger \hat{a}_{n+1} + \text{h.c.}] \\
&\quad + \sum_{n=1}^{L/2}[J_e\cos\theta(\hat{a}_n^\dagger\hat{a}_n - \hat{b}_n^\dagger\hat{b}_n) + \Delta_c(\hat{a}_n^\dagger\hat{a}_n + \hat{b}_n^\dagger\hat{b}_n)], \\
H_{\rm L} &= -\frac{J}{2}\sum_{i=-1}^{-\infty}(\hat{c}_{i+1}^\dagger\hat{c}_i + \text{h.c.}), \\
H_{\rm R} &= -\frac{J}{2}\sum_{i=L+1}^{\infty}(\hat{c}_{i+1}^\dagger\hat{c}_i + \text{h.c.}).
\end{aligned} \tag{6.30}$$

We assume the lattice sites of device L is even. The tunnelings between leads and device are given by

$$H_{\rm LD} = -\frac{J}{2}(\hat{a}_1^\dagger\hat{c}_0 + \text{h.c.}), H_{\rm RD} = -\frac{J}{2}(\hat{c}_{L+1}^\dagger\hat{b}_L + \text{h.c.}). \tag{6.31}$$

In the basis $\{\cdots, \hat{c}_{-1}^\dagger, \hat{c}_0^\dagger, \hat{a}_1^\dagger, \hat{b}_1^\dagger, \cdots, \hat{a}_{L/2}^\dagger, \hat{b}_{L/2}^\dagger, \hat{c}_{L+1}^\dagger, \hat{c}_{L+2}^\dagger, \cdots\}$, we can formulate the Hamiltonian of the whole system as

$$H = \begin{bmatrix} H_{\rm L} & \tau_{\rm L} & 0 \\ \tau_{\rm L}^\dagger & H_{\rm D} & \tau_{\rm R} \\ 0 & \tau_{\rm R}^\dagger & H_{\rm R} \end{bmatrix}, \tag{6.32}$$

where

$$H_{\mathrm{L}}=\begin{bmatrix}\cdots & \cdots & \cdots & \cdots\\ \cdots & 0 & -J/2 & 0\\ \cdots & -J/2 & 0 & -J/2\\ \cdots & 0 & -J/2 & 0\end{bmatrix}_{\infty\times\infty}, H_{\mathrm{R}}=\begin{bmatrix}0 & -J/2 & 0 & \cdots\\ -J/2 & 0 & -J/2 & \cdots\\ 0 & -J/2 & 0 & \cdots\\ \cdots & \cdots & \cdots & \cdots\end{bmatrix}_{\infty\times\infty},$$

$$\tau_{\mathrm{L}}=\begin{bmatrix}\cdots & \cdots & \cdots & \cdots\\ 0 & 0 & \cdots & 0\\ 0 & 0 & \cdots & 0\\ -J/2 & 0 & \cdots & 0\end{bmatrix}_{\infty\times L}, \tau_{\mathrm{R}}=\begin{bmatrix}0 & 0 & 0 & \cdots\\ \cdots & \cdots & \cdots & \cdots\\ 0 & 0 & 0 & \cdots\\ -J/2 & 0 & 0 & \cdots\end{bmatrix}_{L\times\infty},$$

$$H_{\mathrm{D}}=\begin{bmatrix}\Delta_c+J_e\cos\theta & J_1-\frac{J_e}{2}\sin\theta & 0 & 0 & \cdots\\ J_1-\frac{J_e}{2}\sin\theta & \Delta_c-J_e\cos\theta & J_2+\frac{J_e}{2}\sin\theta & 0 & \cdots\\ 0 & J_2+\frac{J_e}{2}\sin\theta & \Delta_c+J_e\cos\theta & J_1-\frac{J_e}{2}\sin\theta & \cdots\\ 0 & 0 & J_1-\frac{J_e}{2}\sin\theta & \Delta_c-J_e\cos\theta & \cdots\\ \cdots & \cdots & \cdots & \cdots & \cdots\end{bmatrix}_{L\times L}.$$

Then the Green function for the device is given by [218],

$$G_{\mathrm{D}}=[E\hat{\boldsymbol{I}}-H_{\mathrm{D}}-\Sigma_{\mathrm{L}}^{r}-\Sigma_{\mathrm{R}}^{r}]^{-1}, \tag{6.33}$$

where the self-energies of the leads are $\Sigma_{\mathrm{L}}^{r}=\tau_{\mathrm{L}}^{\dagger}g_{\mathrm{L}}^{r}\tau_{\mathrm{L}}$ and $\Sigma_{\mathrm{R}}^{r}=\tau_{\mathrm{R}}g_{\mathrm{R}}^{r}\tau_{\mathrm{R}}^{\dagger}$. The lead Green functions are

$$g_{\mathrm{L}}^{r}=[(E+i\eta)\hat{\boldsymbol{I}}-H_{\mathrm{L}}]^{-1}, g_{\mathrm{R}}^{r}=[(E+i\eta)\hat{\boldsymbol{I}}-H_{\mathrm{R}}]^{-1}. \tag{6.34}$$

After some straightforward calculations, we find that the non-zero elements in the self-energies are $[\Sigma_{\mathrm{L}}^{r}]_{11}=\frac{J^2}{4}[g_{\mathrm{L}}^{r}]_{\infty,\infty}$ and $[\Sigma_{\mathrm{R}}^{r}]_{LL}=\frac{J^2}{4}[g_{\mathrm{R}}^{r}]_{11}$, otherwise is zero. Due to the symmetrical configuration of the whole system, we note that $[\Sigma_{\mathrm{L}}^{r}]_{11}=[\Sigma_{\mathrm{R}}^{r}]_{LL}$. Furthermore, the dispersion relation of the semi-infinite lead is $E=-J\cos k$, the group velocity in the lead is $\nu_{\mathrm{L}}=\nu_{\mathrm{R}}=\frac{\partial E}{\partial k}=J\sin k$ and the self-energy of the lead is $[\Sigma_{\mathrm{L}}^{r}]_{11}=[\Sigma_{\mathrm{R}}^{r}]_{LL}=-\frac{J}{2}e^{ika}$ [218]. Keeping $\nu_L>0$ and $\nu_R<0$ for the photon injecting from leads to device, we have

(assume $J > 0$ from now on)

$$\nu_{\rm L} = \sqrt{J^2 - E^2}, \Sigma_{\rm L} = [\Sigma_{\rm L}^r]_{11} = \frac{1}{2}(E - i\sqrt{J^2 - E^2}),$$
$$\nu_{\rm R} = -\sqrt{J^2 - E^2}, \Sigma_{\rm R} = [\Sigma_{\rm R}^r]_{LL} = \frac{1}{2}(E + i\sqrt{J^2 - E^2}). \tag{6.35}$$

Therefore, the device Green function is

$$G_{\rm D} = \begin{bmatrix} E_L & J_\alpha & 0 & 0 & 0 \\ J_\alpha & E - \Delta_c + J_e\cos\theta & J_\beta & 0 & 0 \\ 0 & J_\beta & \cdots & \cdots & 0 \\ 0 & 0 & \cdots & E - \Delta_c - J_e\cos\theta & J_\alpha \\ 0 & 0 & 0 & J_\alpha & E_R \end{bmatrix}^{-1}_{L\times L}, \tag{6.36}$$

with $E_L = E - \Delta_c - J_e\cos\theta - \Sigma_L$, $E_R = E - \Delta_c + J_e\cos\theta - \Sigma_R$, $J_\alpha = -J_1 + \frac{J_e}{2}\sin\theta$,$J_\beta = -J_2 - \frac{J_e}{2}\sin\theta$. Via the continued fraction method and taking into account the periodic pattern of the matrix elements in $G_{\rm D}$, the closed form of $[G_{\rm D}]_{11}$ can be obtained,

$$[G_{\rm D}]_{11}^{-1} + \Sigma_L = E - \Delta_c - J_e\cos\theta - \frac{(J_1 - \frac{J_e}{2}\sin\theta)^2}{E - \Delta_c + J_e\cos\theta - \frac{(J_2 + \frac{J_e}{2}\sin\theta)^2}{[G_{\rm D}]_{11}^{-1} + \Sigma_L}}. \tag{6.37}$$

Solving this algebra equation we have

$$[G_{\rm D}]_{11} = -\frac{2(E_p + P_1)}{m_1 - im_2}, \tag{6.38}$$

where

$$\begin{aligned} m_1 &= J_1^2 - J_2^2 + (E_p + P_1)(\Delta_c + P_1) - (J_1 + J_2)P_2 \\ &\quad -\sqrt{[E_p^2 - (J_1 + J_2)^2 - P_1^2][E_p^2 - (P_2 - J_1 + J_2)^2 - P_1^2]}, \qquad (6.39) \\ m_2 &= (E_p + P_1)\sqrt{J^2 - (E_p + \Delta_c)^2}, \qquad (6.40) \\ P_1 &= J_e\cos\theta, P_2 = J_e\sin\theta, \qquad (6.41) \end{aligned}$$

and $E_p = E - \Delta_c$ is the in-gap energy of our photonic system. Based on the Fisher-Lee relation [219], $S_{nm}(E) = -\delta_{nm} + i\sqrt{\nu_n\nu_m}[G_{\rm D}]_{nm}$, where the scattering matrix is

$S = \begin{bmatrix} r_{\mathrm{L}} & t_{\mathrm{R}} \\ t_{\mathrm{L}} & r_{\mathrm{R}} \end{bmatrix}$. The reflection coefficient from the left lead is thus

$$r_L(\theta) = -1 + i\sqrt{J^2 - E^2}[G_{\mathrm{D}}]_{11}. \tag{6.42}$$

Therefore, through substituting Eq. (6.38) into Eq. (6.42), we find that

$$r_L(\theta) = -\frac{m_1 + im_2}{m_1 - im_2}. \tag{6.43}$$

By substituting the above equation into Eq. (6.29), we get

$$\begin{aligned} Q &= \frac{1}{2\pi}\int_0^{2\pi} d(\arctan\frac{m_2^2 - m_1^2}{2m_1m_2}) \\ &= \frac{1}{2}\left[\mathrm{sgn}(2\delta + J_e) - \mathrm{sgn}(2\delta - J_e)\right] \\ &= C. \end{aligned} \tag{6.44}$$

One finds that the winding number of the phase of the reflection coefficients is exactly equal to the topological invariant of this system.

6.4 Scattering Formulation of Topological Invariant

In this section, we show that the information regarding the photonic reflection coefficient can be probed spectroscopically using cavity input-output process. The photonic Chern insulator is then detected by counting the winding number of reflection coefficient phase. In contrast to fermi system, one can directly probe the edge state and its scattering feature in our photonic simulator. The reason is that bosonic photons can occupy one particular eigenstate at the same time. This could be done by externally driving the resonators with the driven frequency tuned as the eigenenergy of the lattice, then the corresponding eigenmode would be occupied with some weights. In the rotating frame with respect to the driving frequency, the driven Hamiltonian is $H_d = \sum_n(\Omega_{na}\hat{a}_n^\dagger + \Omega_{nb}\hat{b}_n^\dagger) + h.c$, where $\Omega_{na,nb}$ are the driven amplitudes in the nth unit cell. In the presence of dissipation, the expectation value of the cavity field $\hat{a}_j$ in steady state can be derived from the solution of the Lindblad master equation

$$\langle\dot{\hat{a}}_j\rangle = -i\langle[\hat{a}_j, H + H_d]\rangle + \kappa\sum_n\langle L[\hat{a}_n]\hat{a}_j\rangle, \tag{6.45}$$

where the Lindblad term $L[\hat{a}_n]\hat{a}_j = \hat{a}_n\hat{a}_j\hat{a}_n^\dagger - \{\hat{a}_n^\dagger\hat{a}_n, \hat{a}_j\}/2$, κ is the cavity decay rate. In the new bases $\mathbf{a} = (\langle\hat{a}_1\rangle, \langle\hat{b}_1\rangle, ..., \langle\hat{a}_n\rangle, \langle\hat{b}_n\rangle)^{\mathrm{T}}$ and $\mathbf{\Omega} = (\Omega_{1a}, \Omega_{1b}, ..., \Omega_{na}, \Omega_{nb})^{\mathrm{T}}$ with Tr representing the transposition of matrix, based on the condition of the steady state solution $\langle\dot{\hat{a}}_j\rangle = 0$, we can write the expectation value of the cavity fields in the steady state as

$$\mathbf{a} = -(\Delta_c + T - i\frac{\kappa}{2})^{-1}\mathbf{\Omega}, \tag{6.46}$$

where the elements of matrix T are defined by $T_{na,nb} = T_{nb,na} = J_1 - J_e\sin(\theta/2)$, $T_{na,(n-1)b} = T_{(n-1)b,na} = J_2 + J_e\sin(\theta/2)$, $T_{na(b),na(b)} = \pm J_e\cos\theta$.

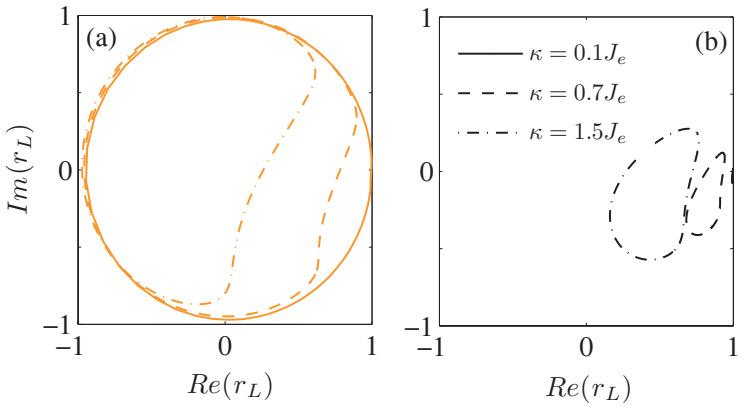

Figure 6.5: The reflection coefficients from the left edge for topological (a) nontrivial and (b) trivial insulators.

To probe the edge states, we need to occupy this edge states firstly. We choose to excite the left edge state by external driving the leftmost resonator (see Fig. 6.3), with the driving microwave pulses chosen as $\mathbf{\Omega} = (\Omega_{1a}, 0, ..., 0, 0)^{\mathrm{T}}$ and driven frequency ω_d tuned to the in-gap energy. The reason is that the left edge state has maximal probability occupying the leftmost resonator. In contrast, if the middle and rightmost resonators are driven with same laser, the occupied probability of the left edge mode is very small, then there will almost be no resonant eigenmode and all the photons will finally decay into vacuum in the steady state. When the driven frequency is tuned as the bulk energy, the photons are extensively populated in the lattice, which satisfies the feature of Bloch bulk state. Therefore, the photonic edge state can be directly observed by measuring the corresponding average photon number in the steady state.

The detection of photonic reflection coefficient is naturally related to cavity input-output process [220]. Using input-output formalism, the reflected output photons a_1^{out} from the left edge resonator is related to the input photon through $a_1^{out} = a_1^{in} + \sqrt{\kappa}a_1$,

where the input field a_1^{in} is related to the external driving by $\sqrt{\kappa}a_1^{in} = i\Omega_{1a}$ [221]. Using Eq. (6.46), the photonic reflection coefficient from the left edge is obtained as

$$r_L(\theta) = \frac{\langle a_1^{out}\rangle}{\langle a_1^{in}\rangle} = 1 + i\kappa[(\Delta_c + T - i\frac{\kappa}{2})^{-1}]_{11}. \tag{6.47}$$

In Fig. 6.5(a) and (b), we plot the numerical results of reflection coefficients for photonic topological nontrivial (Chern number $C = 1$) and trivial insulator (Chern number $C = 0$). The lattice size is $L = 10$, the driving amplitude $\Omega_{1a} = 0.1J_e$ and the cavity decay rates $\kappa = 0.1J_e$ (solid), $0.7J_e$ (dashed) and $1.5J_e$ (dash-dotted). The results show that the winding number of the reflection coefficient phase of r_L is 1 and 0 respectively, which yield the photonic topological invariants. This method also applies for the right edge case and the conclusion is same. We take into account the influence of the cavity decay. The results in Fig. 6.5(a) and (b) show that, if the cavity decay rate is not larger than the energy gap $2J_e$, the in-gap energy will remain in the energy gap and the winding number will remain the same. Then our measurement is very robust to fluctuations of the frequency of the input photon. For circuit-QED experiment, with a typical choice of $\omega_d = 5\Delta$, $g_0 = 0.1\Delta$, the qubit-assisted hopping amplitude J_e can approach the order of 10 MHz. For the current coupled transmission line resonator experiment [222], the hopping amplitudes $J_{1,2}$ can be tuned within the range $1 - 100$ MHz. The experimental parameters required in our work are within the experimentally accessible regimes.

Therefore, the simulation and detection of photonic Chern insulator is possible in the circuit-QED lattice by using the atom-mediated resonator array. Similar idea has been realized in recent experiment [190]. In this chapter, we show that one can use the scattering of incident photons to detect the topological properties of the system. This method is highly promising for the photonic lattice. Indeed, the studies of topological effects in photonic systems pave the way for topological photonics [223, 224]. Depending the tunable parameters of different systems, there are various ways to fabricate topological photonic materials. For example, the photonic Floquet topological insulator is realized in a three dimensional waveguides lattice [193]. The propagation coordinate (z) acts as 'time' and can be used to observe topological states.

In circuit-QED system, the nonlinear effects are quite important and can be employed for topological effects, such as topological pumping [225]. Recently, Lee and Thomale consider the linear circuits and find that topolectrical boundary resonances appear in the impedance read-out of a circuit [226]. The topolectrical circuits can establish a bridge between electronics and topological states of matter. As the nonlinear effects which

can be generated from the Josephson junction are included, more interesting and novel phenomena can be explored in the near future [227].

Chapter 7

Summary and Outlook

In this thesis, we have focussed on gauge fields and geometric phases for several periodic systems. We now make a summary of this thesis and discuss some potential directions for future work.

7.1 Summary

In Chapter 2, we introduce the approaches to produce artificial gauge fields. The adiabatic evolution approach is discussed in both Abelian and non-Abelian cases. The realization of Aharonov-Bohm effect in optical lattice with the help of artificial gauge field is discussed. By employing the angular momentum of Laguerre-Gauss lasers, we present a scheme to observe the interference patterns with the influence of Abelian and non-Abelian artificial gauge fields.

In Chapter 3, we study the Berry's phase in optical lattice. For the lattice with inversion symmetry, Berry's phase is quantized. Such phase in one dimensional periodic system with inversion symmetry is also known for Zak phase, which is defined in the Brillouin zone. Motivated by recent developments in experimental realization of SSH model in optical lattice, we consider the system with more subsites. The topological phase transitions are analysed in the four-band model with Zak phase. For the three-band model, the Aharonov-Bohm cage arising from the destructive interference is considered if the long-range hopping is generated.

In Chapter 4, we discuss the geometric phase and winding number in 1/2-spin chain with multispin interactions. First, we use the winding number to label all the phases in phase diagrams. Then, the finite-size scaling of geometric phase close to critical points with different low-energy dispersions is considered. The linear and quadratic low-energy

dispersions obey different scaling behaviors. We observed that there is a close connection between topological phase transition, quantum criticality, energy band structure and geometric phase.

In Chapter 5, we consider the nonequilibrium dynamics of edge states. In the topological systems with open boundary, the edge modes can be quenched to nonequilibrium by sudden changing some parameters in the system. In this chapter, we consider a long-time average of the system and find an equivalent ensemble description of it. By means of the long-time limit, the fluctuation is averaged out and statistical features are revealed.

At last, we introduce a proposal to realize a photonic Chern insulator in a one-dimensional circuit-QED lattice in Chapter 6. Based on Laughlins pumping argument and input-output formalism, the photonic edge states and topological invariant can be unambiguously measured even in a dissipative resonator network, which may take a significant step towards observing a topological invariant with circuit-QED.

7.2 Outlook

We next discuss briefly possible future research directions. The topological pumping has been investigated in the translational invariant lattices, like in waveguide [177], optical lattices [12, 14, 11]. It is interesting to consider open systems. Because the relation between pumping charges and topological invariants in the bulk states, the topological invariants can be studied for mixed states [38, 37, 36]. These works provide motivations for the topological pumping with thermal states. Another interesting possibility is to explore the relation between topological invariant and statistical distributions. Some works have paved the way to this direction [31, 211, 28, 24].

How can the intrinsic topological properties affect the nonequilibrium dynamics? The role played by topology in quenching edge modes [161, 162] and Bloch states [157, 158] has been noted. Moreover, the geometric phase has an effect in generating excitations in the driven spin chain [53]. These works are important attempts to deepen our understanding of geometric phase or topological invariant in nonequilibrium physics.

The topological orders and geometric effects has been discussed for several decades. They have brought us some surprising twists. And a question that we may ask is: what's next? Is there other possibilities to change our perspective in physics? One possibility in this direction is an insight into the concept of time. Recently, the idea of time crystal is proposed [228, 229]. Similar to the translational invariant in spacial crystal, the time crystal is characterized by the discrete time translational symmetry. Recent works in

nonequilibrium physics with floquet driving propose a way to realize time-spatial order [230, 231, 232].

Bibliography

[1] HP Büchler, M Hermele, SD Huber, Matthew PA Fisher, and P Zoller. Atomic quantum simulator for lattice gauge theories and ring exchange models. *Phys. Rev. Lett.*, 95(4):040402, 2005. 1

[2] J Ignacio Cirac, Paolo Maraner, and Jiannis K Pachos. Cold atom simulation of interacting relativistic quantum field theories. *Phys. Rev. Lett.*, 105(19):190403, 2010. 1

[3] Leonardo Mazza, Alejandro Bermudez, Nathan Goldman, Matteo Rizzi, Miguel Angel Martin-Delgado, and Maciej Lewenstein. An optical-lattice-based quantum simulator for relativistic field theories and topological insulators. *New J. Phys.*, 14(1):015007, 2012. 1, 17

[4] Julian Struck, Christoph Ölschläger, R Le Targat, Parvis Soltan-Panahi, André Eckardt, Maciej Lewenstein, Patrick Windpassinger, and Klaus Sengstock. Quantum simulation of frustrated classical magnetism in triangular optical lattices. *Science*, 333(6045):996–999, 2011. 1

[5] Dieter Jaksch, Ch Bruder, Juan Ignacio Cirac, Crispin W Gardiner, and Peter Zoller. Cold bosonic atoms in optical lattices. *Phys. Rev. Lett.*, 81(15):3108, 1998. 2, 16, 17, 18

[6] Dieter Jaksch and Peter Zoller. Creation of effective magnetic fields in optical lattices: the Hofstadter butterfly for cold neutral atoms. *New J. Phys.*, 5(1):56, 2003. 2, 4, 10, 17, 18

[7] Dieter Jaksch and Peter Zoller. The cold atom Hubbard toolbox. *Ann. Phys.*, 315(1):52–79, 2005. 2, 4, 10

[8] X.J. Liu, M.F. Borunda, X. Liu, and J. Sinova. Effect of induced spin-orbit coupling for atoms via laser fields. *Phys. Rev. Lett.*, 102(4):046402, 2009. 2

[9] Chunji Wang, Chao Gao, Chao-Ming Jian, and Hui Zhai. Spin-orbit coupled spinor bose-einstein condensates. *Phys. Rev. Lett.*, 105(16):160403, 2010. 2

[10] Y-J Lin, K Jiménez-García, and IB Spielman. Spin-orbit-coupled bose-einstein condensates. *Nature*, 471(7336):83–86, 2011. 2

[11] Lei Wang, Matthias Troyer, and Xi Dai. Topological charge pumping in a one-dimensional optical lattice. *Phys. Rev. Lett.*, 111(2):026802, 2013. 2, 96

[12] Michael Lohse, Christian Schweizer, Oded Zilberberg, Monika Aidelsburger, and Immanuel Bloch. A Thouless quantum pump with ultracold bosonic atoms in an optical superlattice. *Nat. Phys.*, 2015. 2, 3, 40, 96

[13] H-I Lu, Max Schemmer, Lauren M Aycock, Dina Genkina, Seiji Sugawa, and Ian B Spielman. Geometrical pumping with a Bose-Einstein condensate. *Phys. Rev. Lett.*, 116, 2016. 2, 37

[14] Shuta Nakajima, Takafumi Tomita, Shintaro Taie, Tomohiro Ichinose, Hideki Ozawa, Lei Wang, Matthias Troyer, and Yoshiro Takahashi. Topological Thouless pumping of ultracold fermions. *Nat. Phys.*, 2016. 2, 3, 40, 96

[15] Charles L Kane and Eugene J Mele. Quantum spin Hall effect in graphene. *Phys. Rev. Lett.*, 95(22):226801, 2005. 2

[16] B Andrei Bernevig, Taylor L Hughes, and Shou-Cheng Zhang. Quantum spin Hall effect and topological phase transition in HgTe quantum wells. *Science*, 314(5806):1757–1761, 2006. 2

[17] Markus König, Steffen Wiedmann, Christoph Brüne, Andreas Roth, Hartmut Buhmann, Laurens W Molenkamp, Xiao-Liang Qi, and Shou-Cheng Zhang. Quantum spin Hall insulator state in HgTe quantum wells. *Science*, 318(5851):766–770, 2007. 2

[18] N Goldman, JC Budich, and P Zoller. Topological quantum matter with ultracold gases in optical lattices. *Nat. Phys.*, 12(7):639–645, 2016. 2

[19] J Zak. Berry's phase for energy bands in solids. *Phys. Rev. Lett.*, 62(23):2747, 1989. 3, 5, 34

[20] Raffaele Resta. Theory of the electric polarization in crystals. *Ferroelectrics*, 136(1):51–55, 1992. 3

[21] RD King-Smith and David Vanderbilt. Theory of polarization of crystalline solids. *Phys. Rev. B*, 47(3):1651, 1993. 3, 37, 39

[22] Shigeki Onoda, Shuichi Murakami, and Naoto Nagaosa. Topological nature of polarization and charge pumping in ferroelectrics. *Phys. Rev. Lett.*, 93(16):167602, 2004. 3

[23] Yaacov E Kraus and Oded Zilberberg. Topological equivalence between the Fibonacci quasicrystal and the Harper model. *Phys. Rev. Lett.*, 109(11):116404, 2012. 3, 74

[24] Julia M Zeuner, Mikael C Rechtsman, Yonatan Plotnik, Yaakov Lumer, Stefan Nolte, Mark S Rudner, Mordechai Segev, and Alexander Szameit. Observation of a topological transition in the bulk of a non-Hermitian system. *Phys. Rev. Lett.*, 115(4):040402, 2015. 3, 35, 49, 78, 96

[25] Meng Xiao, ZQ Zhang, and Che Ting Chan. Surface impedance and bulk band geometric phases in one-dimensional systems. *Phys. Rev. X*, 4(2):021017, 2014. 3, 37

[26] Qiang Wang, Meng Xiao, Hui Liu, Shining Zhu, and CT Chan. Measurement of the zak phase of photonic bands through the interface states of a metasurface/photonic crystal. *Phys. Rev. B*, 93(4):041415, 2016. 3

[27] Meng Xiao, Guancong Ma, Zhiyu Yang, Ping Sheng, ZQ Zhang, and Che Ting Chan. Geometric phase and band inversion in periodic acoustic systems. *Nat. Phys.*, 11(3):240–244, 2015. 3, 37

[28] MS Rudner and LS Levitov. Topological transition in a non-hermitian quantum walk. *Phys. Rev. Lett.*, 102(6):065703, 2009. 3, 49, 96

[29] T. Kitagawa, M.S. Rudner, E. Berg, and E. Demler. Exploring topological phases with quantum walks. *Phys. Rev. A*, 82(3):033429, 2010. 3

[30] H. Obuse and N. Kawakami. Topological phases and delocalization of quantum walks in random environments. *Phys. Rev. B*, 84(19):195139, 2011. 3

[31] F. Cardano, M. Maffei, F. Massa, B. Piccirillo, C. de Lisio, G. De Filippis, V. Cataudella, E. Santamato, and L. Marrucci. Dynamical moments reveal a topological quantum transition in a photonic quantum walk. *Nat. Commun.*, 7(11439), 2016. 3, 96

[32] V.V. Ramasesh, E. Flurin, M. Rudner, I. Siddiqi, and N.Y. Yao. Direct probe of topological invariants using Bloch oscillating quantum walks. *Physical Review Letters*, 118(13):130501, 2017. 3

[33] E. Flurin, V.V. Ramasesh, S. Hacohen-Gourgy, L.S. Martin, N.Y. Yao, and I. Siddiqi. Observing topological invariants using quantum walk in superconducting circuits. *arXiv preprint arXiv:1610.03069*, 2016. 3

[34] Armin Uhlmann. Parallel transport and quantum holonomy along density operators. *Rep. Math. Phys.*, 24(2):229–240, 1986. 3

[35] A Uhlmann. On Berry phases along mixtures of states. *Annalen der Physik*, 501(1):63–69, 1989. 3

[36] O Viyuela, A Rivas, and MA Martin-Delgado. Uhlmann phase as a topological measure for one-dimensional fermion systems. *Phys. Rev. Lett.*, 112(13):130401, 2014. 3, 73, 96

[37] O Viyuela, A Rivas, and MA Martin-Delgado. Two-dimensional density-matrix topological fermionic phases: topological uhlmann numbers. *Phys. Rev. Lett.*, 113(7):076408, 2014. 3, 96

[38] Zhoushen Huang and Daniel P Arovas. Topological indices for open and thermal systems via uhlmanns phase. *Phys. Rev. Lett.*, 113(7):076407, 2014. 3, 96

[39] Jan Carl Budich and Sebastian Diehl. Topology of density matrices. *Phys. Rev. B*, 91(16):165140, 2015. 3

[40] S. Diehl, E. Rico, M.A. Baranov, and P. Zoller. Topology by dissipation in atomic quantum wires. *Nat. Phys.*, 7(12):971–977, 2011. 3

[41] Erik Sjöqvist, Arun K Pati, Artur Ekert, Jeeva S Anandan, Marie Ericsson, Daniel KL Oi, and Vlatko Vedral. Geometric phases for mixed states in interferometry. *Phys. Rev. Lett.*, 85(14):2845, 2000. 3

[42] ANGELO Carollo, I Fuentes-Guridi, M Franca Santos, and Vlatko Vedral. Geometric phase in open systems. *Phys. Rev. Lett.*, 90(16):160402, 2003. 3

[43] DM Tong, Erik Sjöqvist, Leong Chuan Kwek, and Choo Hiap Oh. Kinematic approach to the mixed state geometric phase in nonunitary evolution. *Phys. Rev. Lett.*, 93(8):080405, 2004. 3

[44] J.F. Du, P. Zou, M.J. Shi, L.C. Kwek, J.W. Pan, C.H. Oh, A. Ekert, D.K.L Oi, and M. Ericsson. Observation of geometric phases for mixed states using nmr interferometry. *Phys. Rev. Lett.*, 91(10):100403, 2003. 3

[45] F.M. Cucchietti, J.F. Zhang, F.C. Lombardo, P.I. Villar, and R. Laflamme. Geometric phase with nonunitary evolution in the presence of a quantum critical bath. *Phys. Rev. Lett.*, 105(24):240406, 2010. 3

[46] O. Viyuela, A. Rivas, S. Gasparinetti, A. Wallraff, S. Filipp, and M.A. Martin-Delgado. A measurement protocol for the topological uhlmann phase. *arXiv preprint arXiv:1607.08778*, 2016. 3

[47] G Zhang and Z Song. Topological characterization of extended quantum Ising models. *Phys. Rev. Lett.*, 115(17):177204, 2015. 4, 5, 50, 52, 63

[48] L-M Duan, E Demler, and MD Lukin. Controlling spin exchange interactions of ultracold atoms in optical lattices. *Phys. Rev. Lett.*, 91(9):090402, 2003. 4

[49] Jonathan Simon, Waseem S Bakr, Ruichao Ma, M Eric Tai, Philipp M Preiss, and Markus Greiner. Quantum simulation of antiferromagnetic spin chains in an optical lattice. *Nature*, 472(7343):307–312, 2011. 4

[50] Oliver Viehmann, Jan von Delft, and Florian Marquardt. Observing the nonequilibrium dynamics of the quantum transverse-field Ising chain in circuit QED. *Phys. Rev. Lett.*, 110(3):030601, 2013. 4, 70

[51] Pierre Pfeuty. The one-dimensional Ising model with a transverse field. *Ann. Phys.*, 57(1):79–90, 1970. 4

[52] Markus Heyl, Anatoli Polkovnikov, and Stefan Kehrein. Dynamical quantum phase transitions in the transverse-field Ising model. *Phys. Rev. Lett.*, 110(13):135704, 2013. 4, 70

[53] Michael Tomka, Anatoli Polkovnikov, and Vladimir Gritsev. Geometric phase contribution to quantum nonequilibrium many-body dynamics. *Phys. Rev. Lett.*, 108(8):080404, 2012. 4, 51, 53, 96

[54] Simone Ziraldo, Alessandro Silva, and Giuseppe E Santoro. Relaxation dynamics of disordered spin chains: Localization and the existence of a stationary state. *Phys. Rev. Lett.*, 109(24):247205, 2012. 4, 5, 51, 72

[55] Angelo CM Carollo and Jiannis K Pachos. Geometric phases and criticality in spin-chain systems. *Phys. Rev. Lett.*, 95(15):157203, 2005. 4, 5, 51, 53

[56] Michael V Berry. Quantal phase factors accompanying adiabatic changes. In *Proc. R. Soc. A: Mathematical, Physical and Engineering Sciences*, volume 392, pages 45–57. The Royal Society, 1984. 4, 10

[57] Frank Wilczek and A Zee. Appearance of gauge structure in simple dynamical systems. *Phys. Rev. Lett.*, 52(24):2111, 1984. 4, 10, 15

[58] R Dum and M Olshanii. Gauge structures in atom-laser interaction: Bloch oscillations in a dark lattice. *Phys. Rev. Lett.*, 76(11):1788, 1996. 4, 10, 11

[59] Yakir Aharonov and David Bohm. Significance of electromagnetic potentials in the quantum theory. *Phys. Rev.*, 115(3):485, 1959. 4, 8

[60] Jean Dalibard, Fabrice Gerbier, Gediminas Juzeliūnas, and Patrik Öhberg. Colloquium: Artificial gauge potentials for neutral atoms. *Rev. Mod. Phys.*, 83(4):1523, 2011. 4, 10

[61] Luigi Amico, Andreas Osterloh, and Francesco Cataliotti. Quantum many particle systems in ring-shaped optical lattices. *Phys. Rev. Lett.*, 95(6):063201, 2005. 5, 20, 21

[62] Shi-Liang Zhu. Scaling of geometric phases close to the quantum phase transition in the xy spin chain. *Phys. Rev. Lett.*, 96(7):077206, 2006. 5, 50, 51, 53, 55, 56, 61, 67

[63] Takumi Ohta, Shu Tanaka, Ippei Danshita, and Keisuke Totsuka. Topological and dynamical properties of a generalized cluster model in one dimension. *Phys. Rev. B*, 93(16):165423, 2016. 5, 50, 62, 63, 64

[64] A Yu Kitaev. Unpaired Majorana fermions in quantum wires. *Physics-Uspekhi*, 44(10S):131, 2001. 5

[65] Anatoli Polkovnikov, Krishnendu Sengupta, Alessandro Silva, and Mukund Vengalattore. *Colloquium* : Nonequilibrium dynamics of closed interacting quantum systems. *Rev. Mod. Phys.*, 83:863–883, Aug 2011. 5

[66] ACT Wu and Chen Ning Yang. Evolution of the concept of the vector potential in the description of fundamental interactions. *Int. J. Mod. Phys. A*, 21(16):3235–3277, 2006. 6

[67] Chen Ning Yang. *Selected Papers (1945-1980), with Commentary*, volume 36. World Scientific, 2005. 7

[68] Chen Ning Yang. Hermann Weyl's contribution to physics. *Selected Papers of Chen Ning Yang II: With Commentaries. Edited by Yang Chen Ning. Published by World Scientific Publishing Co. Pte. Ltd., 2013. ISBN# 9789814449021, pp. 78-92*, 1:78–92, 2013. 7

[69] M Zahid Hasan and Charles L Kane. Colloquium: topological insulators. *Rev. Mod. Phys.*, 82(4):3045, 2010. 10, 85

[70] Xiao-Liang Qi and Shou-Cheng Zhang. Topological insulators and superconductors. *Rev. Mod. Phys.*, 83(4):1057, 2011. 10, 85

[71] K Osterloh, M Baig, L Santos, P Zoller, and M Lewenstein. Cold atoms in non-Abelian gauge potentials: from the Hofstadter "moth" to lattice gauge theory. *Phys. Rev. Lett.*, 95(1):010403, 2005. 10, 17, 40

[72] Hui Zhai. Spin-orbit coupled quantum gases. *Int. J. Mod. Phys. B*, 26(01):1230001, 2012. 10

[73] N Goldman, IB Spielman, et al. Light-induced gauge fields for ultracold atoms. *Rep. Prog. Phys.*, 77(12):126401, 2014. 10

[74] L-M Duan, JI Cirac, and P Zoller. Geometric manipulation of trapped ions for quantum computation. *Science*, 292(5522):1695–1697, 2001. 10

[75] Giuseppe Falci, Rosario Fazio, G Massimo Palma, Jens Siewert, and Vlatko Vedral. Detection of geometric phases in superconducting nanocircuits. *Nature*, 407(6802):355–358, 2000. 10

[76] Shi-Liang Zhu and ZD Wang. Implementation of universal quantum gates based on nonadiabatic geometric phases. *Phys. Rev. Lett.*, 89(9):097902, 2002. 10

[77] David Jeffery Griffiths. *Introduction to quantum mechanics*. Pearson Education India, 2005. 11

[78] Marc Cheneau, Steffen Patrick Rath, Tarik Yefsah, Kenneth John Günter, G Juzeliūnas, and Jean Dalibard. Geometric potentials in quantum optics: A semi-classical interpretation. *Europhys. Lett.*, 83(6):60001, 2008. 13

[79] Y-J Lin, RL Compton, AR Perry, WD Phillips, JV Porto, and IB Spielman. Bose-einstein condensate in a uniform light-induced vector potential. *Phys. Rev. Lett.*, 102(13):130401, 2009. 14

[80] Y-J Lin, Rob L Compton, K Jiménez-García, James V Porto, and Ian B Spielman. Synthetic magnetic fields for ultracold neutral atoms. *Nature*, 462(7273):628–632, 2009. 14

[81] Shi-Liang Zhu, Hao Fu, C-J Wu, S-C Zhang, and L-M Duan. Spin Hall effects for cold atoms in a light-induced gauge potential. *Phys. Rev. Lett.*, 97(24):240401, 2006. 15

[82] Yong Li, C Bruder, and CP Sun. Generalized Stern-Gerlach effect for chiral molecules. *Phys. Rev. Lett.*, 99(13):130403, 2007. 15

[83] J Ruseckas, G Juzeliūnas, P Öhberg, and M Fleischhauer. Non-abelian gauge potentials for ultracold atoms with degenerate dark states. *Phys. Rev. Lett.*, 95(1):010404, 2005. 15

[84] Julian Struck, Christoph Ölschläger, Malte Weinberg, Philipp Hauke, Juliette Simonet, André Eckardt, Maciej Lewenstein, Klaus Sengstock, and Patrick Windpassinger. Tunable gauge potential for neutral and spinless particles in driven optical lattices. *Phys. Rev. Lett.*, 108(22):225304, 2012. 17

[85] Gyu-Boong Jo, Jennie Guzman, Claire K Thomas, Pavan Hosur, Ashvin Vishwanath, and Dan M Stamper-Kurn. Ultracold atoms in a tunable optical kagome lattice. *Phys. Rev. Lett.*, 108(4):045305, 2012. 17

[86] Monika Aidelsburger, Marcos Atala, Sylvain Nascimbène, Stefan Trotzky, Y-A Chen, and Immanuel Bloch. Experimental realization of strong effective magnetic fields in an optical lattice. *Physical review letters*, 107(25):255301, 2011. 17

[87] Monika Aidelsburger, Marcos Atala, Michael Lohse, Julio T Barreiro, B Paredes, and Immanuel Bloch. Realization of the Hofstadter hamiltonian with ultracold atoms in optical lattices. *Phys. Rev. Lett.*, 111(18):185301, 2013. 17

[88] Fabrice Gerbier and Jean Dalibard. Gauge fields for ultracold atoms in optical superlattices. *New J. Phys.*, 12(3):033007, 2010. 17, 40

[89] Janne Ruostekoski, Gerald V Dunne, and Juha Javanainen. Particle number fractionalization of an atomic fermi-dirac gas in an optical lattice. *Phys. Rev. Lett.*, 88(18):180401, 2002. 18

[90] Konstantin Yu Bliokh. Geometrical optics of beams with vortices: Berry phase and orbital angular momentum Hall effect. *Phys. Rev. Lett.*, 97(4):043901, 2006. 19

[91] Xiong-Jun Liu, Xin Liu, Leong Chuan Kwek, and Choo Hiap Oh. Optically induced spin-Hall effect in atoms. *Phys. Rev. Lett.*, 98(2):026602, 2007. 19, 20

[92] M Bhattacharya and Pierre Meystre. Using a Laguerre-Gaussian beam to trap and cool the rotational motion of a mirror. *Phys. Rev. Lett.*, 99(15):153603, 2007. 19

[93] Nigel R Cooper and Zoran Hadzibabic. Measuring the superfluid fraction of an ultracold atomic gas. *Phys. Rev. Lett.*, 104(3):030401, 2010. 19, 20

[94] G Juzeliūnas and P Öhberg. Slow light in degenerate fermi gases. *Rev. Mod. Phys.*, 93(3):033602, 2004. 20

[95] G Juzeliūnas, P Öhberg, J Ruseckas, and A Klein. Effective magnetic fields in degenerate atomic gases induced by light beams with orbital angular momenta. *Phys. Rev. A*, 71(5):053614, 2005. 20

[96] G Juzeliūnas, J Ruseckas, and P Öhberg. Effective magnetic fields induced by EIT in ultra-cold atomic gases. *J. Phys. B: At. Mol. Opt. Phys.*, 38(23):4171, 2005. 20

[97] P Zhang, Y Li, and CP Sun. Induced magnetic monopole from trapped λ-type atom. *Eur. Phys. J. D*, 36(2):229–233, 2005. 20

[98] J Arlt, K Dholakia, L Allen, and MJ Padgett. The production of multiringed Laguerre-Gaussian modes by computer-generated holograms. *J. Mod. Opt.*, 45(6):1231–1237, 1998. 20

[99] Naoya Matsumoto, Taro Ando, Takashi Inoue, Yoshiyuki Ohtake, Norihiro Fukuchi, and Tsutomu Hara. Generation of high-quality higher-order Laguerre-Gaussian beams using liquid-crystal-on-silicon spatial light modulators. *J. Opt. Soc. Am. A.*, 25(7):1642–1651, 2008. 20

[100] Takahiro Kuga, Yoshio Torii, Noritsugu Shiokawa, Takuya Hirano, Yukiko Shimizu, and Hiroyuki Sasada. Novel optical trap of atoms with a doughnut beam. *Phys. Rev. Lett.*, 78:4713–4716, Jun 1997. 20

[101] A Ramanathan, KC Wright, SR Muniz, M Zelan, WT Hill III, CJ Lobb, Kristian Helmerson, WD Phillips, and GK Campbell. Superflow in a toroidal Bose-Einstein condensate: an atom circuit with a tunable weak link. *Phys. Rev. Lett.*, 106(13):130401, 2011. 20

[102] Stephen Eckel, Jeffrey G Lee, Fred Jendrzejewski, Noel Murray, Charles W Clark, Christopher J Lobb, William D Phillips, Mark Edwards, and Gretchen K Campbell. Hysteresis in a quantized superfluid 'atomtronic' circuit. *Nature*, 506(7487):200–203, 2014. 20

[103] Sonja Franke-Arnold, Jonathan Leach, Miles J Padgett, Vassilis E Lembessis, Demos Ellinas, Amanda J Wright, John M Girkin, P Ohberg, and Aidan S Arnold. Optical ferris wheel for ultracold atoms. *Opt. Exp.*, 15(14):8619–8625, 2007. 20

[104] AV Ponomarev, S Denisov, and P Hänggi. ac-driven atomic quantum motor. *Phys. Rev. Lett.*, 102(23):230601, 2009. 20

[105] D Aghamalyan, N T Nguyen, F Auksztol, K S Gan, M Martinez Valado, P C Condylis, L-C Kwek, R Dumke, and L Amico. An atomtronic flux qubit: a ring lattice of Bose-Einstein condensates interrupted by three weak links. *New J. Phys.*, 18(7):075013, 2016. 20

[106] Luigi Amico, Davit Aghamalyan, Filip Auksztol, Herbert Crepaz, Rainer Dumke, and Leong Chuan Kwek. Superfluid qubit systems with ring shaped optical lattices. *Sci. Rep.*, 4, 2014. 20

[107] Rainer Dumke, Zehuang Lu, John Close, Nick Robins, Antoine Weis, Manas Mukherjee, Gerhard Birkl, Christoph Hufnagel, Luigi Amico, Malcolm G Boshier, et al. Roadmap on quantum optical systems. *J. Opt.*, 18(9):093001, 2016. 20

[108] W-P Su, J. R. Schrieffer, and A. J. Heeger. Solitons in polyacetylene. *Phys. Rev. Lett.*, 42(25):1698, 1979. 27

[109] Alan J Heeger, S Kivelson, JR Schrieffer, and W-P Su. Solitons in conducting polymers. *Rev. Mod. Phys.*, 60(3):781, 1988. 31

[110] Rudolf Ernst Peierls. *Quantum theory of solids*. Number 23. Oxford University Press, 1955. 31

[111] DJ Thouless, Mahito Kohmoto, MP Nightingale, and M Den Nijs. Quantized Hall conductance in a two-dimensional periodic potential. *Phys. Rev. Lett.*, 49(6):405, 1982. 34, 37

[112] J. E. Avron, R. Seiler, and B. Simon. Homotopy and quantization in condensed matter physics. *Phys. Rev. Lett.*, 51:51–53, Jul 1983. 34

[113] Barry Simon. Holonomy, the quantum adiabatic theorem, and Berry's phase. *Phys. Rev. Lett.*, 51:2167–2170, Dec 1983. 34

[114] Raffaele Resta. Manifestations of Berry's phase in molecules and condensed matter. *J. Phys.: Condens. Matter*, 12(9):R107, 2000. 35

[115] Andrea Blanco-Redondo, Imanol Andonegui, Matthew J Collins, Gal Harari, Yaakov Lumer, Mikael C Rechtsman, Benjamin J Eggleton, and Mordechai Segev. Topological optical waveguiding in silicon and the transition between topological and trivial defect states. *Phys. Rev. Lett.*, 116(16):163901, 2016. 35

[116] Stefano Longhi. Zak phase of photons in optical waveguide lattices. *Opt. Lett.*, 38(19):3716–3719, 2013. 35

[117] Marcos Atala, Monika Aidelsburger, Julio T Barreiro, Dmitry Abanin, Takuya Kitagawa, Eugene Demler, and Immanuel Bloch. Direct measurement of the Zak phase in topological Bloch bands. *Nat. Phys.*, 9(12):795–800, 2013. 35, 37, 49, 71

[118] P. Delplace, D. Ullmo, and G. Montambaux. Zak phase and the existence of edge states in graphene. *Phys. Rev. B*, 84:195452, Nov 2011. 37

[119] GP Mikitik and Yu V Sharlai. Manifestation of Berry's phase in metal physics. *Phys. Rev. Lett.*, 82(10):2147, 1999. 37

[120] KS Novoselov, Edward McCann, SV Morozov, Vladimir I Falko, MI Katsnelson, U Zeitler, D Jiang, F Schedin, and AK Geim. Unconventional quantum Hall effect and Berry's phase of 2π in bilayer graphene. *Nat. Phys.*, 2(3):177–180, 2006. 37

[121] Yuanbo Zhang, Yan-Wen Tan, Horst L Stormer, and Philip Kim. Experimental observation of the quantum Hall effect and Berry's phase in graphene. *Nature*, 438(7065):201–204, 2005. 37

[122] Pasquale Marra, Roberta Citro, and Carmine Ortix. Fractional quantization of the topological charge pumping in a one-dimensional superlattice. *Phys. Rev. B*, 91(12):125411, 2015. 40

[123] WP Su and JR Schrieffer. Fractionally charged excitations in charge-density-wave systems with commensurability 3. *Phys. Rev. Lett.*, 46(11):738, 1981. 40

[124] Stefano Longhi. Aharonov-Bohm photonic cages in waveguide and coupled resonator lattices by synthetic magnetic fields. *Opt. Lett.*, 39(20):5892–5895, 2014. 40

[125] S. Mukherjee and R.R. Thomson. Observation of localized flat-band modes in a quasi-one-dimensional photonic rhombic lattice. *Opt. Lett.*, 40(23):5443–5446, 2015. 40

[126] Ramaz Khomeriki and Sergej Flach. Landau-Zener Bloch oscillations with perturbed flat bands. *Phys. Rev. Lett.*, 116:245301, Jun 2016. 43

[127] Alejandro Bermudez, Tobias Schaetz, and Diego Porras. Synthetic gauge fields for vibrational excitations of trapped ions. *Phys. Rev. Lett.*, 107:150501, Oct 2011. 43

[128] Sriram Ganeshan, Kai Sun, and S Das Sarma. Topological zero-energy modes in gapless commensurate Aubry-André-Harper models. *Phys. Rev. Lett.*, 110(18):180403, 2013. 47, 49, 73

[129] Meng Xiao, Z. Q. Zhang, and C. T. Chan. Surface impedance and bulk band geometric phases in one-dimensional systems. *Phys. Rev. X*, 4:021017, Apr 2014. 49, 78

[130] Mark S Rudner, Michael Levin, and Leonid S Levitov. Survival, decay, and topological protection in non-Hermitian quantum transport. *arXiv preprint arXiv:1605.07652*, 2016. 49

[131] Huaiming Guo and Shu Chen. Kaleidoscope of symmetry-protected topological phases in one-dimensional periodically modulated lattices. *Physical Review B*, 91(4):041402, 2015. 49

[132] Pietro Smacchia, Luigi Amico, Paolo Facchi, Rosario Fazio, Giuseppe Florio, Saverio Pascazio, and Vlatko Vedral. Statistical mechanics of the cluster Ising model. *Phys. Rev. A*, 84(2):022304, 2011. 50, 63

[133] Wonmin Son, Luigi Amico, Rosario Fazio, Alioscia Hamma, Saverio Pascazio, and Vlatko Vedral. Quantum phase transition between cluster and antiferromagnetic states. *Europhys. Lett.*, 95(5):50001, 2011. 50

[134] Sebastián Montes and Alioscia Hamma. Phase diagram and quench dynamics of the cluster-xy spin chain. *Phys. Rev. E*, 86(2):021101, 2012. 50, 55

[135] Stein Olav Skrøvseth and Stephen D Bartlett. Phase transitions and localizable entanglement in cluster-state spin chains with Ising couplings and local fields. *Phys. Rev. A*, 80(2):022316, 2009. 50

[136] Irakli Titvinidze and GI Japaridze. Phase diagram of the spin extended model. *Eur. Phys. J. B*, 32(3):383–393, 2003. 51

[137] A. A. Zvyagin and G. A. Skorobagat'ko. Exactly solvable quantum spin model with alternating and multiple spin exchange interactions. *Phys. Rev. B*, 73:024427, Jan 2006. 51

[138] M. Benito, A. Gómez-León, V. M. Bastidas, T. Brandes, and G. Platero. Floquet engineering of long-range p-wave superconductivity. *Phys. Rev. B*, 90:205127, Nov 2014. 59

[139] Andreas Osterloh, Luigi Amico, Giuseppe Falci, and Rosario Fazio. Scaling of entanglement close to a quantum phase transition. *Nature*, 416(6881):608–610, 2002. 61, 67

[140] Frank Pollmann, Subroto Mukerjee, Ari M Turner, and Joel E Moore. Theory of finite-entanglement scaling at one-dimensional quantum critical points. *Phys. Rev. Lett.*, 102(25):255701, 2009. 61

[141] L-A Wu, Marcelo S Sarandy, and Daniel A Lidar. Quantum phase transitions and bipartite entanglement. *Phys. Rev. Lett.*, 93(25):250404, 2004. 61

[142] Lorenzo Campos Venuti and Paolo Zanardi. Quantum critical scaling of the geometric tensors. *Phys. Rev. Lett.*, 99(9):095701, 2007. 61

[143] G De Chiara, L Lepori, M Lewenstein, and A Sanpera. Entanglement spectrum, critical exponents, and order parameters in quantum spin chains. *Phys. Rev. Lett.*, 109(23):237208, 2012. 61

[144] Ville Lahtinen and Eddy Ardonne. Realizing all so(N)$_1$ quantum criticalities in symmetry protected cluster models. *Phys. Rev. Lett.*, 115(23):237203, 2015. 61, 63

[145] Robert Raussendorf, Daniel E Browne, and Hans J Briegel. Measurement-based quantum computation on cluster states. *Phys. Rev. A*, 68(2):022312, 2003. 62

[146] Shin-Ming Huang, Su-Yang Xu, Ilya Belopolski, Chi-Cheng Lee, Guoqing Chang, Tay-Rong Chang, BaoKai Wang, Nasser Alidoust, Guang Bian, Madhab Neupane, et al. New type of Weyl semimetal with quadratic double Weyl fermions. *Proceedings of the National Academy of Sciences*, 113(5):1180–1185, 2016. 65

[147] J Eisert, M Friesdorf, and Christian Gogolin. Quantum many-body systems out of equilibrium. *Nat. Phys.*, 11(2):124–130, 2015. 70

[148] Marcos Rigol, Vanja Dunjko, and Maxim Olshanii. Thermalization and its mechanism for generic isolated quantum systems. *Nature*, 452(7189):854–858, 2008. 70, 73

[149] David Chen, Matthew White, Cecilia Borries, and Brian DeMarco. Quantum quench of an atomic Mott insulator. *Phys. Rev. Lett.*, 106(23):235304, 2011. 70

[150] Yu-Ao Chen, Sebastian D Huber, Stefan Trotzky, Immanuel Bloch, and Ehud Altman. Many-body Landau-Zener dynamics in coupled one-dimensional Bose liquids. *Nat. Phys.*, 7(1):61–67, 2011. 70

[151] Florian Meinert, Manfred J Mark, Emil Kirilov, Katharina Lauber, Philipp Weinmann, Andrew J Daley, and H-C Nägerl. Quantum quench in an atomic one-dimensional Ising chain. *Phys. Rev. Lett.*, 111(5):053003, 2013. 70

[152] Florian Meinert, Manfred J Mark, Emil Kirilov, Katharina Lauber, Philipp Weinmann, Michael Gröbner, Andrew J Daley, and Hanns-Christoph Nägerl. Observation of many-body dynamics in long-range tunneling after a quantum quench. *Science*, 344(6189):1259–1262, 2014. 70

[153] Ulrich Schneider, Lucia Hackermüller, Jens Philipp Ronzheimer, Sebastian Will, Simon Braun, Thorsten Best, Immanuel Bloch, Eugene Demler, Stephan Mandt, David Rasch, et al. Fermionic transport and out-of-equilibrium dynamics in a homogeneous Hubbard model with ultracold atoms. *Nat. Phys.*, 8(3):213–218, 2012. 70

[154] Corinna Kollath, Andreas M Läuchli, and Ehud Altman. Quench dynamics and nonequilibrium phase diagram of the Bose-Hubbard model. *Phys. Rev. Lett.*, 98(18):180601, 2007. 70, 72

[155] Hakan E Türeci, M Hanl, M Claassen, A Weichselbaum, T Hecht, B Braunecker, A Govorov, L Glazman, A Imamoglu, and J von Delft. Many-body dynamics of exciton creation in a quantum dot by optical absorption: A quantum quench towards kondo correlations. *Phys. Rev. Lett.*, 106(10):107402, 2011. 70

[156] Philipp Hauke, Maciej Lewenstein, and André Eckardt. Tomography of band insulators from quench dynamics. *Phys. Rev. Lett.*, 113(4):045303, 2014. 70

[157] Jan Carl Budich and Markus Heyl. Dynamical topological order parameters far from equilibrium. *Phys. Rev. B*, 93(8):085416, 2016. 70, 96

[158] Szabolcs Vajna and Balázs Dóra. Topological classification of dynamical phase transitions. *Phys. Rev. B*, 91(15):155127, 2015. 70, 96

[159] MD Caio, Nigel R Cooper, and MJ Bhaseen. Quantum quenches in Chern insulators. *Phys. Rev. Lett.*, 115(23):236403, 2015. 70, 71

[160] Adolfo G Grushin, Sthitadhi Roy, and Masudul Haque. Response of fermions in Chern bands to spatially local quenches. *arXiv preprint arXiv:1508.04778*, 2015. 70, 71

[161] A Bermudez, D Patane, L Amico, and MA Martin-Delgado. Topology-induced anomalous defect production by crossing a quantum critical point. *Phys. Rev. Lett.*, 102(13):135702, 2009. 70, 96

[162] A Bermudez, L Amico, and MA Martin-Delgado. Dynamical delocalization of Majorana edge states by sweeping across a quantum critical point. *New J. Phys.*, 12(5):055014, 2010. 70, 96

[163] Aavishkar A Patel, Shraddha Sharma, and Amit Dutta. Quench dynamics of edge states in 2D topological insulator ribbons. *Eur. Phys. J. B*, 86(9):1–6, 2013. 70

[164] Atanu Rajak and Amit Dutta. Survival probability of an edge Majorana in a one-dimensional p-wave superconducting chain under sudden quenching of parameters. *Phys. Rev. E*, 89(4):042125, 2014. 70, 72, 74, 76

[165] HT Quan, Z Song, XF Liu, P Zanardi, and CP Sun. Decay of loschmidt echo enhanced by quantum criticality. *Phys. Rev. Lett.*, 96(14):140604, 2006. 70

[166] Pinja Haikka, John Goold, Suzanne McEndoo, Francesco Plastina, and Sabrina Maniscalco. Non-Markovianity, Loschmidt echo, and criticality: A unified picture. *Phys. Rev. A*, 85(6):060101, 2012. 70

[167] Alessandro Silva. Statistics of the work done on a quantum critical system by quenching a control parameter. *Phys. Rev. Lett.*, 101(12):120603, 2008. 70, 71

[168] Francis NC Paraan and Alessandro Silva. Quantum quenches in the Dicke model: Statistics of the work done and of other observables. *Phys. Rev. E*, 80(6):061130, 2009. 70, 71

[169] Lorenzo Campos Venuti and Paolo Zanardi. Universality in the equilibration of quantum systems after a small quench. *Phys. Rev. A*, 81(3):032113, 2010. 70

[170] Ross Dorner, John Goold, Cecilia Cormick, Mauro Paternostro, and Vlatko Vedral. Emergent thermodynamics in a quenched quantum many-body system. *Phys. Rev. Lett.*, 109(16):160601, 2012. 71

[171] L Fusco, S Pigeon, TJG Apollaro, A Xuereb, L Mazzola, M Campisi, A Ferraro, M Paternostro, and G De Chiara. Assessing the nonequilibrium thermodynamics in a quenched quantum many-body system via single projective measurements. *Phys. Rev. X*, 4(3):031029, 2014. 71

[172] Yulia E Shchadilova, Pedro Ribeiro, and Masudul Haque. Quantum quenches and work distributions in ultralow-density systems. *Phys. Rev. Lett.*, 112(7):070601, 2014. 71

[173] Lorenzo Campos Venuti and Paolo Zanardi. Unitary equilibrations: Probability distribution of the Loschmidt echo. *Phys. Rev. A*, 81(2):022113, 2010. 71

[174] Marcos Rigol and Mattias Fitzpatrick. Initial-state dependence of the quench dynamics in integrable quantum systems. *Phys. Rev. A*, 84(3):033640, 2011. 71

[175] Serge Aubry and Gilles André. Analyticity breaking and anderson localization in incommensurate lattices. *Ann. Israel Phys. Soc*, 3(133):18, 1980. 73

[176] Philip George Harper. Single band motion of conduction electrons in a uniform magnetic field. *Proc. Phys. Soc. London, Sec. A*, 68(10):874, 1955. 73

[177] Yaacov E Kraus, Yoav Lahini, Zohar Ringel, Mor Verbin, and Oded Zilberberg. Topological states and adiabatic pumping in quasicrystals. *Phys. Rev. Lett.*, 109(10):106402, 2012. 73, 74, 96

[178] Giacomo Roati, Chiara DErrico, Leonardo Fallani, Marco Fattori, Chiara Fort, Matteo Zaccanti, Giovanni Modugno, Michele Modugno, and Massimo Inguscio. Anderson localization of a non-interacting Bose-Einstein condensate. *Nature*, 453(7197):895–898, 2008. 73, 74

[179] Douglas R Hofstadter. Energy levels and wave functions of Bloch electrons in rational and irrational magnetic fields. *Phys. Rev. B*, 14(6):2239, 1976. 74

[180] Armin Uhlmann. The transition probability in the state space of a*-algebra. *Rep. Math. Phys.*, 9(2):273–279, 1976. 76

[181] F.D.M. Haldane and S. Raghu. Possible realization of directional optical waveguides in photonic crystals with broken time-reversal symmetry. *Phys. Rev. Lett.*, 100(1):013904, 2008. 78

[182] Z. Wang, Y.D. Chong, J.D. Joannopoulos, and M. Soljačić. Observation of unidirectional backscattering-immune topological electromagnetic states. *Nature*, 461(7265):772–775, 2009. 78

[183] Kejie Fang and Shanhui Fan. Controlling the flow of light using the inhomogeneous effective gauge field that emerges from dynamic modulation. *Phys. Rev. Lett.*, 111(20):203901, 2013. 78

[184] Kejie Fang, Zongfu Yu, and Shanhui Fan. Photonic Aharonov-Bohm effect based on dynamic modulation. *Phys. Rev. Lett.*, 108(15):153901, 2012. 78

[185] M Hafezi. Synthetic gauge fields with photons. *Int. J. Mod. Phys. B*, 28(02):1441002, 2014. 78

[186] Qian Lin and Shanhui Fan. Light guiding by effective gauge field for photons. *Phys. Rev. X*, 4(3):031031, 2014. 78

[187] S Mittal, J Fan, S Faez, A Migdall, JM Taylor, and M Hafezi. Topologically robust transport of photons in a synthetic gauge field. *Phys. Rev. Lett.*, 113(8):087403, 2014. 78

[188] Andrew A Houck, Hakan E Türeci, and Jens Koch. On-chip quantum simulation with superconducting circuits. *Nat. Phys.*, 8(4):292–299, 2012. 78

[189] Jens Koch, Andrew A Houck, Karyn Le Hur, and SM Girvin. Time-reversal-symmetry breaking in circuit-QED-based photon lattices. *Phys. Rev. A*, 82(4):043811, 2010. 78

[190] P. Roushan, C. Neill, A. Megrant, Y. Chen, R. Babbush, R. Barends, B. Campbell, Z. Chen, B. Chiaro, A. Dunsworth, A. Fowler, E. Jeffrey, J. Kelly, E. Lucero, J. Mutus, O'Malley P.J.J., M. Neeley, C. Quintana, D. Sank, A. Vainsencher, J. Wenner, T. White, E. Kapit, H. Neven, and J.M. Martinis. Chiral groundstate currents of interacting photons in a synthetic magnetic field. *Nat. Phys.*, 13(2):146–151, 2017. 78, 93

[191] Mohammad Hafezi, Eugene A Demler, Mikhail D Lukin, and Jacob M Taylor. Robust optical delay lines with topological protection. *Nat. Phys.*, 7(11):907–912, 2011. 78, 84

[192] Jiasen Jin, Davide Rossini, Rosario Fazio, Martin Leib, and Michael J Hartmann. Photon solid phases in driven arrays of nonlinearly coupled cavities. *Phys. Rev. Lett.*, 110(16):163605, 2013. 78

[193] Mikael C Rechtsman, Julia M Zeuner, Yonatan Plotnik, Yaakov Lumer, Daniel Podolsky, Felix Dreisow, Stefan Nolte, Mordechai Segev, and Alexander Szameit. Photonic floquet topological insulators. *Nature*, 496(7444):196–200, 2013. 78, 93

[194] M. Mariantoni, F. Deppe, A. Marx, R. Gross, F.K. Wilhelm, and E. Solano. Two-resonator circuit quantum electrodynamics: A superconducting quantum switch. *Physical Review B*, 78(10):104508, 2008. 78

[195] G.M. Reuther, D. Zueco, F. Deppe, E. Hoffmann, E.P. Menzel, T. Weißl, M. Mariantoni, S. Kohler, A. Marx, E. Solano, R. Gross, and P. Hänggi. Two-resonator circuit quantum electrodynamics: Dissipative theory. *Physical Review B*, 81(14):144510, 2010. 78

[196] M. Hofheinz, H. Wang, M. Ansmann, R.C. Bialczak, E. Lucero, M. Neeley, A.D. O'connell, D. Sank, J. Wenner, J.M. Martinis, and A.N. Cleland. Synthesizing arbitrary quantum states in a superconducting resonator. *Nature*, 459(7246):546–549, 2009. 79

[197] A. D. O'Connell, M. Hofheinz, M. Ansmann, R. C. Bialczak, M. Lenander, E. Lucero, M. Neeley, D. Sank, H. Wang, M. Weides, J. Wenner, J.M. Martinis, and A.N. Cleland. Quantum ground state and single-phonon control of a mechanical resonator. *Nature*, 464(7289):697–703, 2010. 79

[198] Dimitris G Angelakis, Marcelo Franca Santos, and Sougato Bose. Photon-blockade-induced Mott transitions and XY spin models in coupled cavity arrays. *Phys. Rev. A*, 76(3):031805, 2007. 79

[199] Michael J Hartmann, Fernando GSL Brandao, and Martin B Plenio. Strongly interacting polaritons in coupled arrays of cavities. *Nat. Phys.*, 2(12):849–855, 2006. 79

[200] Frederick W Strauch, Kurt Jacobs, and Raymond W Simmonds. Arbitrary control of entanglement between two superconducting resonators. *Physical review letters*, 105(5):050501, 2010. 79

[201] H Wang, Matteo Mariantoni, Radoslaw C Bialczak, M Lenander, Erik Lucero, M Neeley, AD OConnell, D Sank, M Weides, J Wenner, et al. Deterministic entanglement of photons in two superconducting microwave resonators. *Physical review letters*, 106(6):060401, 2011. 79, 84

[202] Borja Peropadre, David Zueco, Friedrich Wulschner, Frank Deppe, Achim Marx, Rudolf Gross, and Juan José García-Ripoll. Tunable coupling engineering between superconducting resonators: From sidebands to effective gauge fields. *Physical Review B*, 87(13):134504, 2013. 79

[203] A. Blais, R.S. Huang, A. Wallraff, S. M Girvin, and R.J. Schoelkopf. Cavity quantum electrodynamics for superconducting electrical circuits: An architecture for quantum computation. *Physical Review A*, 69(6):062320, 2004. 79

[204] A. Wallraff, D.I. Schuster, A. Blais, L. Frunzio, R.S. Huang, J. Majer, S. Kumar, S.M. Girvin, and R.J. Schoelkopf. Strong coupling of a single photon to a superconducting qubit using circuit quantum electrodynamics. *Nature*, 431(7005):162–167, 2004. 79

[205] Z.H. Peng, Yu-xi Liu, J.T. Peltonen, T. Yamamoto, J.S. Tsai, and O. Astafiev. Correlated emission lasing in harmonic oscillators coupled via a single three-level artificial atom. *Physical review letters*, 115(22):223603, 2015. 79

[206] Fei Wang, Wei Nie, Xunli Feng, and CH Oh. Steady-state entanglement of harmonic oscillators via dissipation in a single superconducting artificial atom. *Physical Review A*, 94(1):012330, 2016. 79

[207] JE Mooij, TP Orlando, L Levitov, Lin Tian, Caspar H Van der Wal, and Seth Lloyd. Josephson persistent-current qubit. *Science*, 285(5430):1036–1039, 1999. 79

[208] Yu-xi Liu, JQ You, LF Wei, CP Sun, and Franco Nori. Optical selection rules and phase-dependent adiabatic state control in a superconducting quantum circuit. *Physical review letters*, 95(8):087001, 2005. 79

[209] Lu-Ming Duan, Géza Giedke, Juan Ignacio Cirac, and Peter Zoller. Inseparability criterion for continuous variable systems. *Physical Review Letters*, 84(12):2722, 2000. 83

[210] GQ Liang and YD Chong. Optical resonator analog of a two-dimensional topological insulator. *Phys. Rev. Lett.*, 110(20):203904, 2013. 84

[211] Yizhou Huang, Zhang-qi Yin, and W. L. Yang. Realizing a topological transition in a non-Hermitian quantum walk with circuit QED. *Phys. Rev. A*, 94:022302, Aug 2016. 84, 96

[212] Feng Mei, Jia-Bin You, Wei Nie, Rosario Fazio, Shi-Liang Zhu, and Leong Chuan Kwek. Simulation and detection of photonic Chern insulators in a one-dimensional circuit-QED lattice. *Phys. Rev. A*, 92(4):041805, 2015. 84

[213] Pedram Roushan, C Neill, Yu Chen, M Kolodrubetz, C Quintana, N Leung, M Fang, R Barends, B Campbell, Z Chen, et al. Observation of topological transitions in interacting quantum circuits. *Nature*, 515(7526):241–244, 2014. 84

[214] Yan-Pu Wang, Wan-Li Yang, Yong Hu, Zheng-Yuan Xue, and Ying Wu. Detecting topological phases of microwave photons in a circuit quantum electrodynamics lattice. *npj Quantum Information*, 2:16015, 2016. 84

[215] Robert B Laughlin. Quantized Hall conductivity in two dimensions. *Phys. Rev. B*, 23(10):5632, 1981. 87

[216] IC Fulga, F Hassler, and AR Akhmerov. Scattering theory of topological insulators and superconductors. *Phys. Rev. B*, 85(16):165409, 2012. 87, 88

[217] A.V. Poshakinskiy, A.N. Poddubny, and M. Hafezi. Phase spectroscopy of topological invariants in photonic crystals. *Phys. Rev. A*, 91(4):043830, 2015. 88

[218] S. Datta. *Quantum transport: atom to transistor*. Cambridge University Press, 2005. 89

[219] D.S. Fisher and P.A. Lee. Relation between conductivity and transmission matrix. *Phys. Rev. B*, 23(12):6851, 1981. 90

[220] D.F. Walls and G.J. Milburn. *Quantum optics*. Springer Science & Business Media, 2007. 92

[221] A.A. Clerk, M.H. Devoret, S.M. Girvin, F. Marquardt, and R.J. Schoelkopf. Introduction to quantum noise, measurement, and amplification. *Rev. Mod. Phys.*, 82(2):1155, 2010. 93

[222] S. Schmidt and J. Koch. Circuit QED lattices: towards quantum simulation with superconducting circuits. *Annalen der Physik*, 525(6):395–412, 2013. 93

[223] Karyn Le Hur, Loïc Henriet, Alexandru Petrescu, Kirill Plekhanov, Guillaume Roux, and Marco Schiró. Many-body quantum electrodynamics networks: Non-equilibrium condensed matter physics with light. *Comptes Rendus Physique*, 17(8):808–835, 2016. 93

[224] Ling Lu, John D Joannopoulos, and Marin Soljačić. Topological photonics. *Nature Photonics*, 8(11):821–829, 2014. 93

[225] Jirawat Tangpanitanon, Victor M Bastidas, Sarah Al-Assam, Pedram Roushan, Dieter Jaksch, and Dimitris G Angelakis. Topological pumping of photons in nonlinear resonator arrays. *Physical Review Letters*, 117(21):213603, 2016. 93

[226] Ching Hua Lee and Ronny Thomale. Topolectrical circuits. *arXiv preprint arXiv:1705.01077*, 2017. 93

[227] G Engelhardt, M Benito, G Platero, and T Brandes. Topologically-enforced bifurcations in superconducting circuits. *arXiv preprint arXiv:1611.01467*, 2016. 94

[228] Alfred Shapere and Frank Wilczek. Classical time crystals. *Phys. Rev. Lett.*, 109(16):160402, 2012. 96

[229] Frank Wilczek. Quantum time crystals. *Phys. Rev. Lett.*, 109(16):160401, 2012. 96

[230] Dominic V. Else, Bela Bauer, and Chetan Nayak. Floquet time crystals. *Phys. Rev. Lett.*, 117:090402, Aug 2016. 97

[231] Norman Y Yao, Andrew C Potter, I-D Potirniche, and Ashvin Vishwanath. Discrete time crystals: rigidity, criticality, and realizations. *Phys. Rev. Lett.*, 118(3):030401, 2017. 97

[232] J Zhang, PW Hess, A Kyprianidis, P Becker, A Lee, J Smith, G Pagano, I-D Potirniche, AC Potter, A Vishwanath, et al. Observation of a discrete time crystal. *Nature*, 543(7644):217–220, 2017. 97